An R&D Program for Targetry and Capture at a Muon-Collider Source

A Proposal to the BNL AGS Division

Audrey Bernadon,[d] David Brashears,[i] Kevin Brown,[b] Daniel Carminati,[d]
Michael Cates,[i] John Corlett,[g] F Debray,[f] Adrian Fabich,[d] Richard C. Fernow,[b]
Charles Finfrock,[b] Yasuo Fukui,[c] Tony A. Gabriel,[i] Juan C. Gallardo,[b]
Michael A. Green,[g] George A. Greene,[b] John R. Haines,[i] Jerry Hastings,[b]
Ahmed Hassanein,[a] Michael Iarocci,[b] Colin Johnson,[d] Stephen A. Kahn,[b]
Bruce J. King,[b] Harold G. Kirk,[b,1] Jacques Lettry,[d] Vincent LoDestro,[b]
Changguo Lu,[j] Kirk T. McDonald,[j,2] Nikolai V. Mokhov,[e]
Alfred Moretti,[e] James H. Norem,[a] Robert B. Palmer,[b] Ralf Prigl,[b] Helge Ravn,[d]
Bernard Riemer,[i] James Rose,[b] Thomas Roser,[b] Roman Samulyak,[b]
Joseph Scaduto,[b] Peter Sievers,[d] Nicholas Simos,[b] Philip Spampinato,[i]
Iuliu Stumer,[b] Peter Thieberger,[b] James Tsai,[i] Thomas Tsang,[b] Haipeng Wang,[b]
Robert Weggel,[b] Albert F. Zeller,[h] Yongxiang Zhao[b]

[a] *Argonne National Laboratory, Argonne, IL 60439*
[b] *Brookhaven National Laboratory, Upton, NY 11973*
[c] *University of California, Los Angeles, CA 90095*
[d] *CERN, 1211 Geneva, Switzerland*
[e] *Fermi National Laboratory, Batavia, IL 60510*
[f] *Grenoble High Magnetic Field Laboratory, 38042 Grenoble, France*
[g] *Lawrence Berkeley National Laboratory, Berkeley, CA 94720*
[h] *Michigan State University, East Lansing, MI 48824*
[i] *Oak Ridge National Laboratory, Oak Ridge, TN 37831*
[j] *Princeton University, Princeton, NJ 08544*

(Submitted Sept. 28, 1998; approved as E-951 Oct. 1, 1999)

[1] Project Manager. Email: hkirk@bnl.gov
[2] Spokesperson. Email: kirkmcd@princeton.edu

Executive Summary

Present designs for a muon collider call for a copious source of muons: 5×10^{14} μ/s distributed over 15 pulses/s, each only a few ns long. These muons arise from the decay of low-energy pions that are produced by the interaction of a beam of 1.5×10^{15}, 16-24-GeV protons/s with a high-Z target. The proton beam power is 4 MW, of which 10% is deposited in the target at a density of about 30 J/g per pulse.

The target is surrounded by a 20-T solenoid magnet that captures pions of transverse momentum up to 225 MeV/c into a decay channel. To avoid absorption of the spiraling pions near the target, the latter cannot be cooled by contact with a local thermal bath. Rather, the material of the target must move out of the interaction region to be cooled elsewhere. The baseline design is for a target in the form of a pulsed jet of liquid metal such as Ga, Hg or molten Bi/Pb. A backup design is a nickel target in the form of a band that moves through the interaction region somewhat like the blade of a bandsaw.

The decay channel includes a series of low-frequency rf cavities inside a 1.25-T solenoid. The cavities are phased so as to compress the energy spread of the decay muons, for better injection into the subsequent muon-cooling channel. This process of "phase rotation" is more effective when the first rf cavity is located as close as possible downstream of the target.

The targetry scenario leads to several critical technical questions, which are to be addressed in the proposed R&D program:

- What is the effect of the pressure wave induced in the target by the proton pulse? If the liquid target is dispersed by the beam, do the droplets damage the containment vessel?
- What is the effect of the magnetic field of the capture solenoid on the motion of the liquid-jet target? Is the jet badly distorted by Lorentz forces on the eddy currents induced as the jet enters the field? Does the magnetic field damp the effects of the beam-induced pressure wave?
- Can the first rf cavity of the phase-rotation channel operate viably in close proximity to the target?
- What is the yield of low-energy pions from 16-24-GeV protons incident on the target of the muon-collider source?
- Can numerical simulations of target behavior be developed that permit reliable extrapolation of the data we obtain?

The proposed R&D program into these targetry issues for a muon-collider source consists of eight parts:

1. Initial studies of liquid (and solid) target materials with a proton beam at the AGS.
2. Studies of a liquid-metal jet entering a 20-T magnet at the National High Magnetic Field Laboratory (NHMFL) in Florida.
3. Studies of a full-scale liquid-metal jet in a beam of 10^{14} protons per pulse, but without magnetic field.

4. Studies of a liquid-metal jet + proton beam + 20-T pulsed solenoid magnet.

5. Studies of a 70-MHz rf cavity downstream of the target in the proton beam, but without a magnet around the cavity.

6. Continuation of topic 5, with the addition of a 1.25-T, 1.25-m-radius solenoid surrounding the rf cavity.

7. Characterization of the pion yield downstream of the target + rf cavity.

8. Simulation of the performance of liquid-metal targets: thermal shock, eddy currents. Validation of the simulation by exploding-wire studies.

The first two topics in the program should establish reasonably quickly whether there are any first-order difficulties in the use of a free liquid jet as a proton target in a strong magnetic field. Should this be the case, the solid-band option then would be emphasized. Topics 3-7 explore the next level of technical difficulties in constructing a target that meets the parameters of a muon-collider source. Not covered in this program are the serious issues of operation of a moving target in a high-repetition-rate beam and in the consequent intense radiation environment.

Topics 1 and 3-7 are to be pursued in the FEB U-line of the AGS. In no case do we require more than a few beam pulses per hour. However, there are several other beam requirements that are very aggressive:

- RMS beam-spot size $\sigma_r = 1$ mm for a single extracted bunch of 10^{13}, 24-GeV protons at the target station for topic 1.

- Six-bunch extraction of 10^{14}, 24-GeV protons for topics 3 and 4.

- Pulses of length $\sigma_t = 2$ ns for topics 5 and 6. These pulses could be at 7 GeV, and could involve only single-bunch extraction.

- Slow beam of only 10^6 protons/s at 16-24 GeV for topic 7. For this, the U-line could be operated as a secondary beamline.

Topics 4-7 involve apparatus of substantial size and likely will require development of a new target station along the U-line. The 20-T pulsed magnet of topic 4 also serves as the dump for the proton beam. If the U-line is to continue to be used by others for occasional studies with large integrated proton dose, the new target station must be located downstream of a removable beam dump, to avoid excessive activation of our apparatus.

Considerable magnet power is required:

- The 20-T pulsed magnet of topic 4 requires 4 MW. It is designed to be energized by the MPS power supply, which would be relocated to the U-line.

- The 1.25-T solenoid magnet that surrounds the rf cavity of topic 6 will require 1.2 MW, if its coil is resistive.

- The 2-T bent solenoid magnet of the spectrometer of topic 7 will require 1.4 MW, if its coil is resistive.

A scenario is presented for accomplishing this R&D program over a four-year period, with funding estimated at approximately $1, $2, $3, and $1M for the four years, respectively.

Contents

1 Introduction

1.1 Overview of a Muon Collider

The high-energy frontier of elementary-particle physics presently is pursued with two types of colliding beam facilities:

- **Proton-proton machines**, in which storage rings contain the colliding beams, but for which the constituent (primarily gluon-gluon) center-of-mass (CoM) energy is poorly defined and effectively about 1/10 of the p-p CoM energy.
- **Electron-positron linear colliders**, in which all of the CoM energy is available for fundamental processes, but for which the effects of quantum beamstrahlung limit the precision of the initial state at high energies and luminosities. An e^+e^- storage ring of CoM energy higher than LEP is not foreseen, due to the high power lost to synchrotron radiation.

Future examples of such machines will be rather costly.

In this context a new type of high-energy particle accelerator,

- A **muon collider** [1, 2],

has many attractive features. Muons are leptons, and so, like electrons, couple directly to fundamental processes. But muons are 200 times heavier than electrons, so initial-state radiation (beamstrahlung and synchrotron radiation) are negligible for CoM energies up to $\mathcal{O}$(100 TeV). Hence, recirculating accelerators and storage rings [3] can be used at a muon collider [4, 5, 6], offering cost advantages over both electron-positron and proton-proton colliders.

A physics advantage of muons over electrons and protons (*i.e.*, gluons) is that muons have the largest s-channel coupling (which is proportional to m^2) to Higgs-type bosons, permitting precision studies of such particles [7, 8]. A first muon collider might focus on this unique opportunity.

A 3-4-TeV muon collider would fit on the existing sites of BNL or FNAL, as shown in Fig. 1. The front end (Fig. 2) of such a machine would be suitable for studies of s-channel production of a light Higgs boson.

Muons are unstable, with a lifetime of 2.2 μs in the muon's rest frame. Therefore, copious quantities of muons are required for high luminosity. For this, the muons will be collected over a relatively large volume of phase space, which must quickly be reduced by a cooling process. As muons have little interaction with matter, the cooling can be accomplished by a technique not suitable for other particles, namely ionization cooling [3, 9, 10, 11]. In this process, muons lose their transverse and longitudinal momentum during passage through bulk matter, after which only longitudinal momentum is restored via acceleration in rf cavities, as sketched in Fig. 3.

The muon-decay products are electrons and neutrinos, so a muon collider would be the premier source of future neutrino beams [8, 12]. Indeed, some care as to personnel safety from neutrino-induced radiation will be required in multi-TeV muon colliders [1].

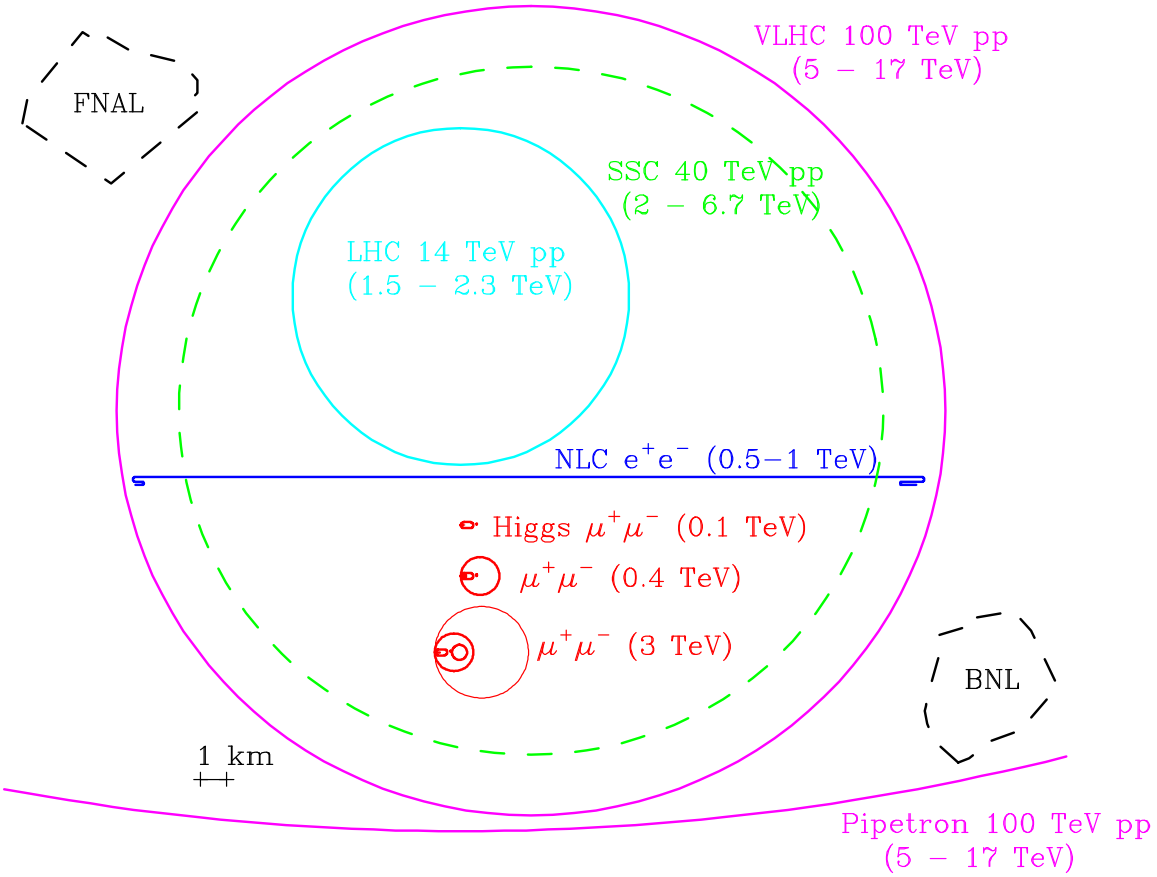

Figure 1: Comparison of footprints of possible future colliders, including muon colliders at CoM energies 0.1, 0.4 and 3 TeV. The energy shown in parentheses for lepton machines is the CoM energy, while for hadron machines it is the effective energy for parton-parton collisions.

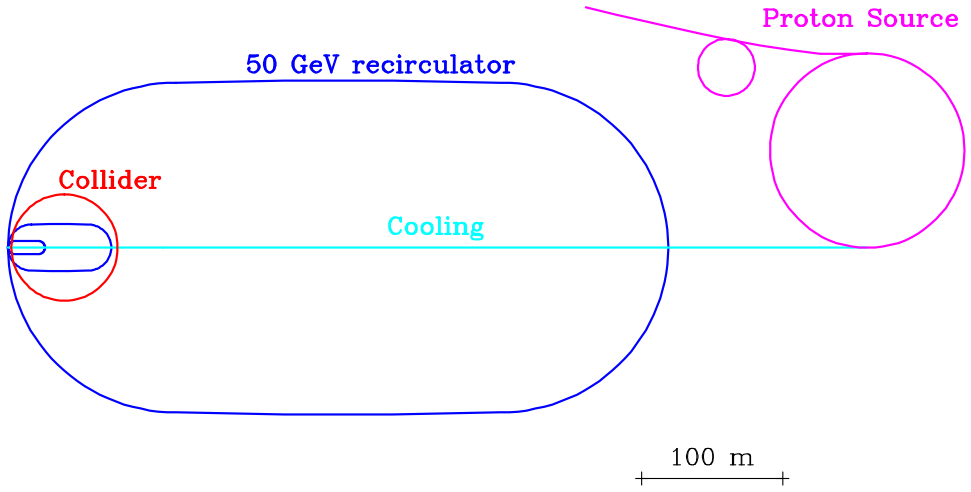

Figure 2: Plan of a 100-GeV CoM Muon Collider, as an example of a first muon collider, to study s-channel light-Higgs production.

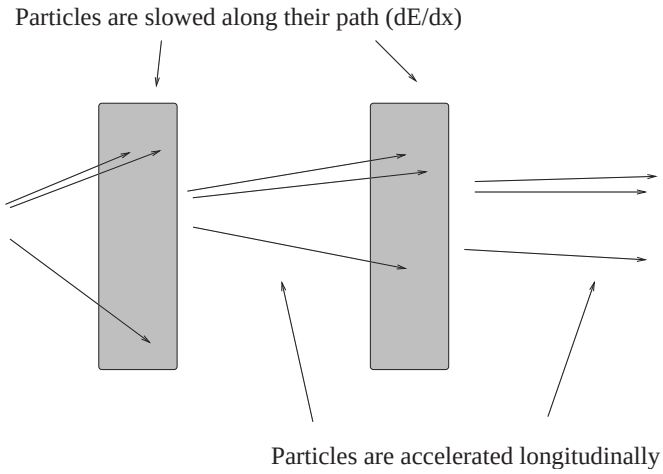

Figure 3: The concept of ionization cooling.

A collaboration [13] of over 100 members[3] has been active for several years in exploring the concept of a muon collider via analytic studies and computer simulation. This effort is summarized in refs. [1, 2] and references therein. A key conclusion is that the concepts of a muon collider should be validated by a program of research and development in two areas:

- Ionization cooling.
- Targetry.

A proposal for an R&D program on ionization cooling [14] has been submitted to Fermilab recently. The present document proposes a companion program for targetry issues: the production of pions by protons hitting a target, and the subsequent capture and decay of the pions to produce the initial muon beam.

1.2 A Targetry Scenario for a Muon Collider

This subsection first discusses the choice of target technology, optimization of the target geometry, and then describes design studies for the pion capture and phase-rotation channel.

Figure 4 gives an overview of the configuration for production of pions by a proton beam impinging on a long, thin target, followed by capture of low-momentum, forward pions in a channel of solenoid magnets with rf cavities to compress the bunch energy while letting the bunch length grow, thus rotating the bunch in phase space.

1.2.1 Pion production

To achieve the present design luminosity of 7×10^{34} cm^{-2}s^{-1} for a 3-TeV CoM muon collider (or 10^{31} cm^{-2}s^{-1} at 100-GeV CoM), 2×10^{12} (or 4×10^{12} at 100-GeV CoM) muons of each sign must be delivered to the collider ring in each pulse at 15 Hz. We estimate that a muon has a probability of only 1/4 of surviving the processes of cooling and acceleration, due to

[3]Spokesperson: R.B. Palmer.

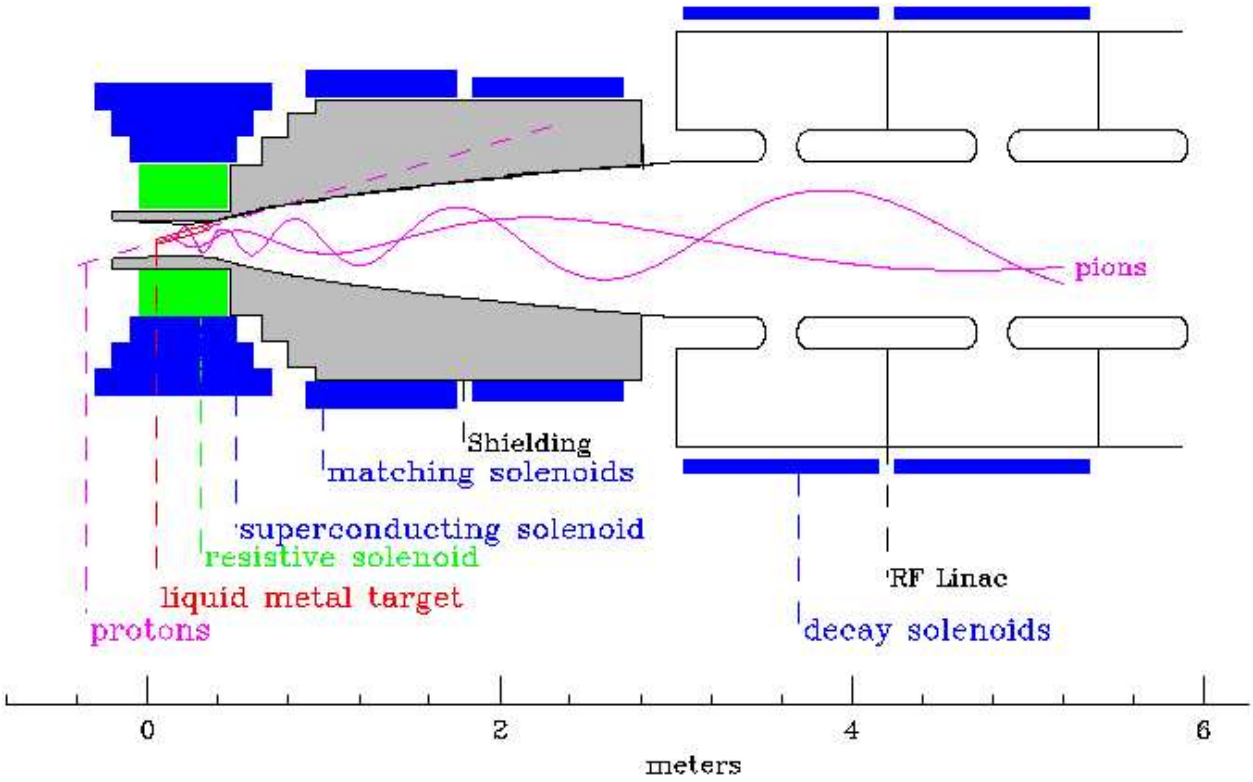

Figure 4: Schematic view of pion production, capture and initial phase rotation. A pulse of 16-30 GeV protons is incident on a skewed target inside a high-field solenoid magnet followed by a decay and phase-rotation channel.

losses in beam apertures or by decay. Thus, 0.8×10^{13} muons (1.6×10^{13} at 100 GeV) must exit the phase-rotation channel each pulse. For pulses of 2.5×10^{13} protons (5×10^{13} for 100 GeV), this requires 0.3 muons per initial proton. And since the efficiency of the phase-rotation channel is about 1/2, this is equivalent to a capture of about 0.6 pions per proton, a very high efficiency.

The pions are produced by the interaction of the proton beam with the primary target. Extensive simulations have been performed for pion production from 8-30-GeV proton beams on different target materials in a high-field solenoid [2, 15, 16, 17, 18]. Three different Monte Carlo codes [19, 20, 21, 22] predict similar pion yields despite significant differences in their physics models. The Collaboration is involved in an AGS experiment (see Appendix A and [23]) to measure the yield of very low momentum pions, which will validate the codes in the critical kinematic region.

The pion yield is greater for relatively high-Z materials, and for these, the pion yield is maximal for longitudinal momenta of the same order as the average transverse momentum ($\approx$ 200 MeV/c). Targets of varying composition ($6 < Z < 82$), radii (0.2-3 cm) and thicknesses (0.5-3 nuclear interaction lengths, λ_I) have been explored. For a fixed number of interaction lengths, the pion yield per proton rises almost linearly with proton energy [18], and hence is almost proportional to the energy deposited in the target. The yield is higher for medium and high-Z target materials, with a noticeable gain at $Z > 26$ for 30-GeV proton beams,

but with only a minor effect for $E \leq 16$ GeV, as shown in Fig. 5a.

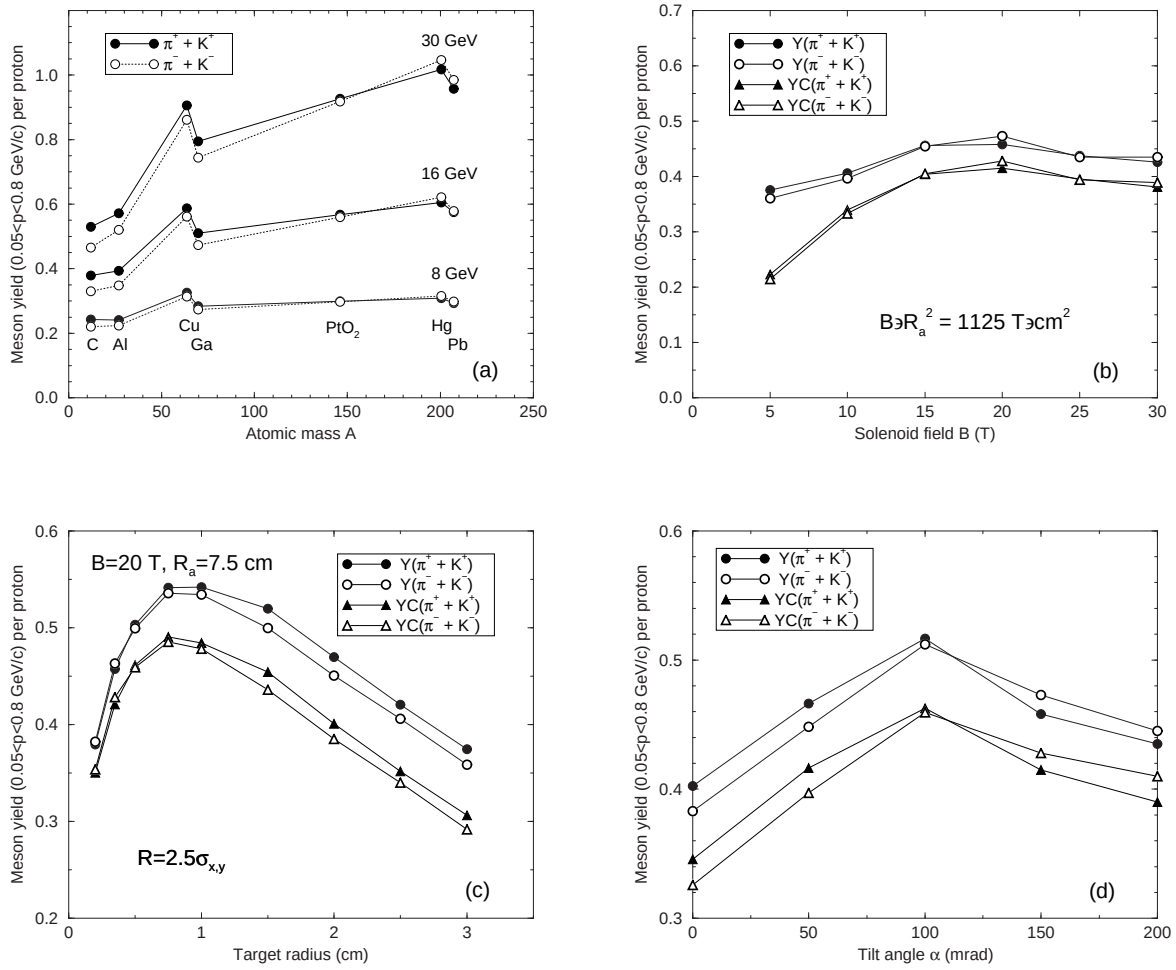

Figure 5: a) Meson yield ($\pi + K$) from a 1.5-λ_I, 1-cm-radius target irradiated with 8, 16 and 30-GeV proton beams as a function of target atomic mass; b) Meson yield from a 3-λ_I, 1-cm-radius gallium target tilted at angle 150 mrad in a 16-GeV proton beam *vs.* solenoid field for a fixed adiabatic invariant BR_a^2; c) Meson yield as a function of target radius; d) Meson yield *vs.* tilt angle between the axis of the capture solenoid and the proton beam. The target is aligned along the beam. The curves labeled YC show mesons that are transported into the decay channel.

1.2.2 Target

The target should be 2-3 interaction lengths long to maximize pion production. A high-density material is favored to reduce the target length, thereby minimizing the size and cost of the capture solenoid magnet. Target radii larger than about 1 cm lead to lower pion rates due to reabsorption, while smaller diameter targets reduce the added production from secondary interactions. Tilting the target by 100-150 mrad minimizes the loss of pions

by absorption in the target after one or more turns on their helical trajectory. Another advantage of the tilted target geometry is that the high-energy and neutral components of the shower can be absorbed in a water-cooled beam dump to the side of the focused beam (see Fig. 4).

About 30 kJ of energy is deposited in the target by each proton pulse (10% of the beam energy). Hence, the target absorbs 400 kW of power at the 15-Hz pulse rate. Cooling of the target via contact with a thermal bath would lead to unacceptable absorption of pions, and radiative cooling is inadequate for such high power in a compact target. Therefore, the target must move so as to carry the energy deposited by the proton beam to a heat exchanger outside the solenoid channel.

Both moving-solid-metal and flowing-liquid targets have been considered, with the latter as the currently preferred solution. A liquid is relatively easy to move, easy to cool, can be readily removed and replaced, and is the preferred target material for most spallation neutron sources under study. A liquid flowing in a pipe was considered, but experience at CERN [24] and Novosibirsk [25] indicates that shock damage to the pipe is a serious problem. Therefore, an open liquid jet is proposed.

A jet of liquid mercury has been demonstrated [26] (see Fig. 6) but not exposed to a beam. For our application, safety and other considerations favor the use of a low-melting-point lead alloy, rather than mercury. Gallium alloys, despite their lower density, are also being considered.

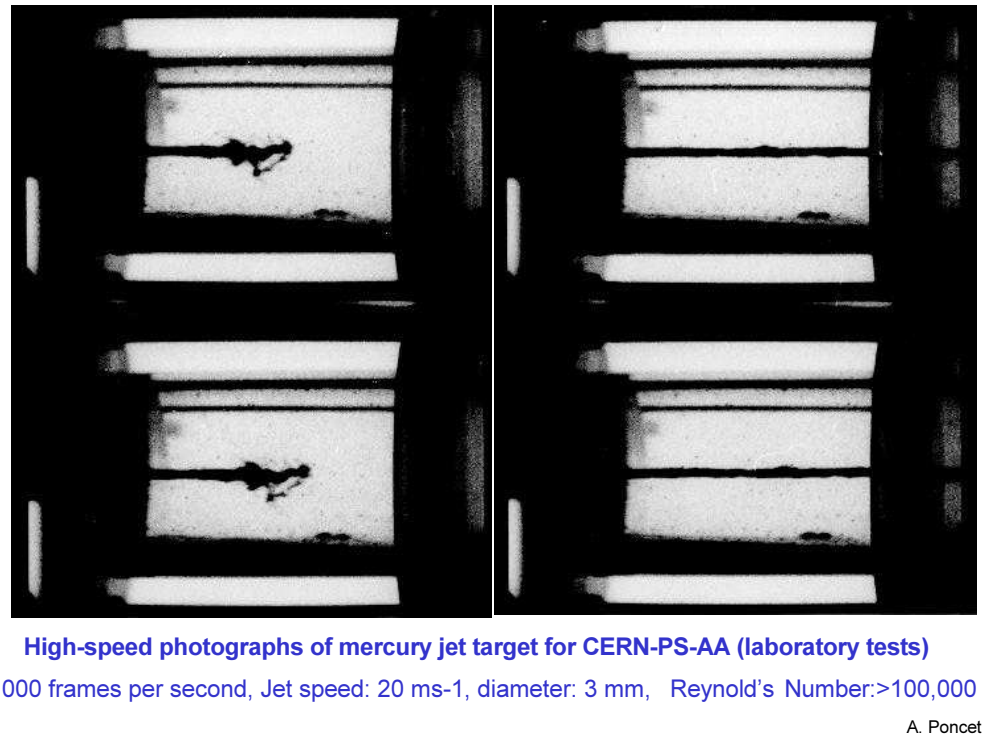

Figure 6: Photographs of a 3-mm-diameter mercury jet.

It is expected that the jet will disperse after being struck by the beam. The target station

must survive damage resulting from the violence in this dispersion. This consideration will determine the minimum beam, and thus jet, radius.

For a conducting liquid jet in a strong magnetic field, as proposed, strong eddy currents will be induced in the jet, causing reaction forces that may disrupt its flow [28, 29]. The forces induced are proportional to the square of the jet radius, and set a maximum for this radius of order 5-10 mm. If this maximum is smaller than the minimum radius set by shock considerations, then multiple smaller beams and jets could be used; *e.g.*, four jets of 5 mm radius with four beams with 2.5 10^{13} protons per bunch. Alternatives include targets made from insulating materials such as liquid PtO_2 or Re_2O_3, slurries (*e.g.*, Pt in water), or powders [31].

A moving-solid-metal target is not the current baseline solution, but is a serious consideration. In this case [32], the target could consist of a long flat band or hoop of copper-nickel that moves along its length (as in a band saw). The band would be many meters in length, would be cooled by gas jets away from the target area, and would be supported and moved by rollers, as shown in Fig. 7.

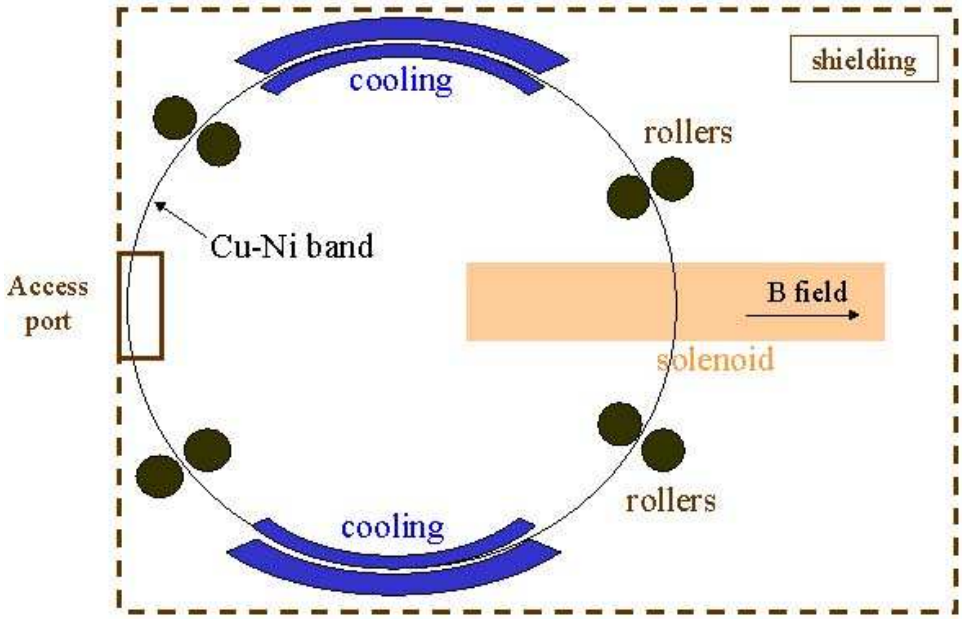

Figure 7: Alternative concept of a solid metal target in the form of a rotating Cu-Ni band.

1.2.3 Capture

In order to capture all pions with transverse momenta $P_\perp$ less than their typical values of 200 MeV/c, the product of the capture solenoid field B and its radius R_a must be greater than 1.33 T-m. The use of a high field and small radius is preferred, to minimize the corresponding transverse emittance, which is proportional to BR^2: for a fixed transverse-momentum capture, this emittance is thus proportional to R. A field of 20 T and 7.5 cm radius was chosen on the basis of simulations described below. This gives $BR = 1.5$ T-m, $BR^2 = 0.1125$ T-m^2 and a maximum transverse-momentum capture of $P_\perp = 225$ MeV/c.

A preliminary design [33] of the capture solenoid has an inner 6-T, 4-MW, water-cooled, hollow-conductor magnet with an inside diameter of 24 cm and an outside diameter of 60 cm. There is space for a 4-cm-thick, water-cooled, heavy-metal shield inside the coil. The outer superconducting magnet has three coils, with inside diameters of 60 to 80 cm. It generates an additional 14 T of field at the target and provides the required tapered field to match into the decay channel. Such a hybrid solenoid will call for state-of-the-art magnet technology [34].

The 20-T capture solenoid is matched via a transfer solenoid [15] into a decay channel consisting of a system of superconducting solenoids with the same adiabatic invariant $BR^2 \propto RP_\perp$. Thus, for a 1.25-T decay channel, B drops by a factor of 1/16 between the target and decay channel; R and $P_\perp$ change by factors of 4 and 1/4, respectively. This permits improved acceptance of transverse momentum within the decay channel, at the cost of an increased spread in longitudinal momentum.

Results of a MARS simulation of pion production and capture [18] are shown in Fig. 5.

The curves labeled YC in Fig. 5b show, as a function of field in the capture solenoid, the yield of pions that are both captured in the high-field solenoid and transported into the decay channel. The radius of the capture solenoid maintains the same BR_a^2 as in the decay channel. The optimum field is 20 T in the capture solenoid.

Figure 5c shows that pion production *vs.* target radius has a maximum near $r = 0.85$ cm. This is the result of the competition between secondary production and absorption.

If the axis of the target is coincident with that of the solenoid field, then there is a relatively high probability that pions re-enter the target after one cycle on their helical trajectory and are lost due to nuclear interactions. When the target and proton beam are at an angle of 100-150 mrad with respect to the field axis, the probability for such pion interactions at the target is reduced, and the overall production rate increased by 60%, as shown in Fig. 5d.

In sum, the simulations indicate that a 20-T solenoid of 16-cm inside diameter surrounding a tilted target will capture about half of all produced pions. With target efficiency included, about 0.45 pions per proton will enter the pion decay channel [18].

1.2.4 Phase-Rotation Linac

The pions, and the muons into which they decay, have an energy spread with an rms value of approximately 100% and a peak value near 200 MeV/c. It would be difficult to handle such a wide spread in any subsequent system. Therefore, a linac is introduced along the decay channel, with frequencies and phases chosen to deaccelerate the fast particles and accelerate the slow ones; *i.e.*, to phase rotate the muon bunch.

Several studies have been made of the design of this system, using differing ranges of rf frequency, delivering different final muon momenta, and differing final bunch lengths. In all cases, efficiencies of close to 0.3 muons per proton are obtained. Until the early stages of the ionization cooling have been designed, it is not yet possible to choose among them.

Independent of the above choices is the question of the location of the focusing solenoid coils and rf cavity design. The closer the first rf cavity is to the target, the less the muon bunch lengthens due to the variation in velocity of the pions.

We discuss here only the case where muons are captured at a mean kinetic energy of

130 MeV. See ref. [1] for an example of capture at a higher energy. Table 1 gives parameters of the linacs used. The frequencies vary between 30 and 60 MHz, and the overall length is 42 m.

Monte Carlo simulations [2], with the program MUONMC [35], were done using pion production calculated by ARC [19] for a copper target of 1 cm radius at an angle of 150 mrad. A uniform solenoidal field was assumed in the phase-rotation channel, and the rf was approximated by a series of kicks.

Table 1: Parameters of Phase-Rotation Linacs

Linac	Length (m)	Frequency (MHz)	Gradient (MeV/m)
1	3	60	5
2	29	30	4
3	5	60	4
4	5	37	4

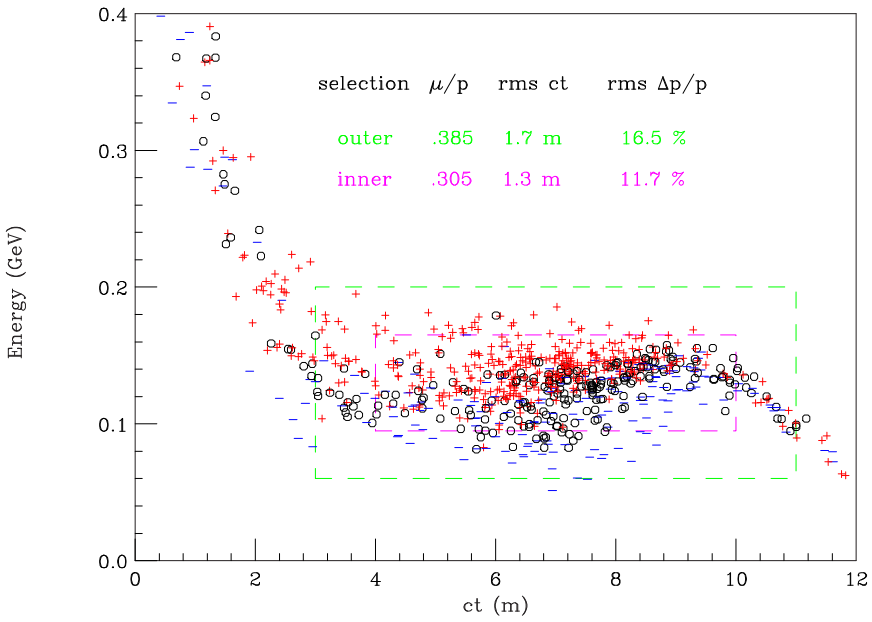

Figure 8: Energy *vs. ct* of μ's at end of the phase-rotation channel. The symbols +, o and − denote muons with polarization $P > \frac{1}{3}$, $-\frac{1}{3} < P < \frac{1}{3}$ and $P < -\frac{1}{3}$, respectively. Without energy selection, the average polarization of the muons is 20%.

Fig. 8 shows the energy *vs. ct* at the end of the decay and phase-rotation channel. A loose final-bunch selection was defined with an energy 130 ± 70 MeV and bunch *ct* between 3 and

11 m. With this selection, the rms energy spread is 16.5%, the rms ct is 1.7 m, and there are 0.385 muons per incident proton. A tighter selection, with an energy 130 ± 35 MeV and bunch ct from 4 to 10 m, gave an rms energy spread of 11.7%, rms ct of 1.3 m, and contained 0.305 muons per incident proton.

1.2.5 Use of Both Signs

Protons on the target produce pions of both signs, and a solenoid will capture both, but the subsequent phase-rotation rf systems will have opposite effects on opposite charges within the same bunch. The baseline solution is to use two proton bunches, separated in time by an odd number of rf half cycles.

A second possibility would be to separate the charges into two channels, and phase rotate them separately. However, the separation, probably using a bent solenoid, is not simple and would not be fully efficient. Whether a gain in overall efficiency could be achieved is not yet known.

1.2.6 Solenoids and RF

Pion capture using higher frequencies appears to be less efficient, and most studies now use frequencies down to 30 MHz. Such cavities, when conventionally designed, are very large (about 6.6 m diameter). In the Snowmass study [37], a reentrant design reduced this diameter to 2.5 m, but this is still large, and it was first assumed that 5-T focusing solenoids would, for economic reasons, be placed within the irises of the cavities (see Fig. 9).

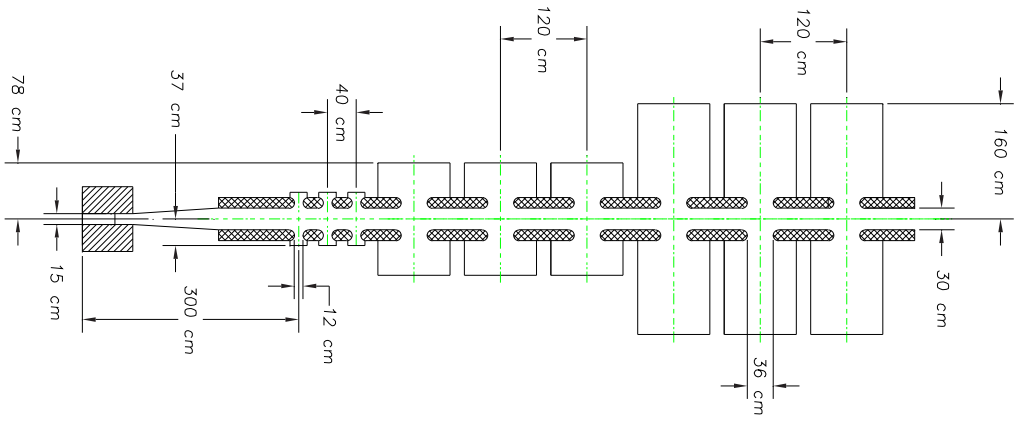

Figure 9: Schematic of capture and phase rotation using rf cavities with superconducting solenoids (hatched) inside the irises. Only three sections each are shown for cavities operating at 90, 50, and 30 MHz.

However, a study [38] of transmission down a realistic system of iris-located coils revealed betatron-resonant excitation from the magnetic-field periodicities, leading to significant particle loss. This was reduced by the use of more complicated coil shapes [37], smaller gaps, and shorter cavities, but remained a problem.

An alternative is to place continuous focusing coils outside the cavities (as shown in Fig. 4). In this case cost will be minimized with lower magnetic fields (1.25-2.5 T) and correspondingly larger decay channel radii (21-30 cm). Simulations are underway to determine the optimal solution.

1.2.7 Muon Polarization

Polarization of the muon beams presents a significant physics advantage over the unpolarized case, since signals and backgrounds of electroweak processes usually come predominantly from different polarization states.

In the center-of-mass frame of a decaying pion, the outgoing muon is fully polarized ($P = -1$ for μ^+, and $+1$ for μ^-). In the lab system the polarization depends on the decay angle θ_d and initial pion energy [39, 40]. For pion kinetic energy larger than the pion mass, the average polarization is about 20%, and if nothing else is done, the polarization of the captured muons after the phase-rotation system is approximately this value.

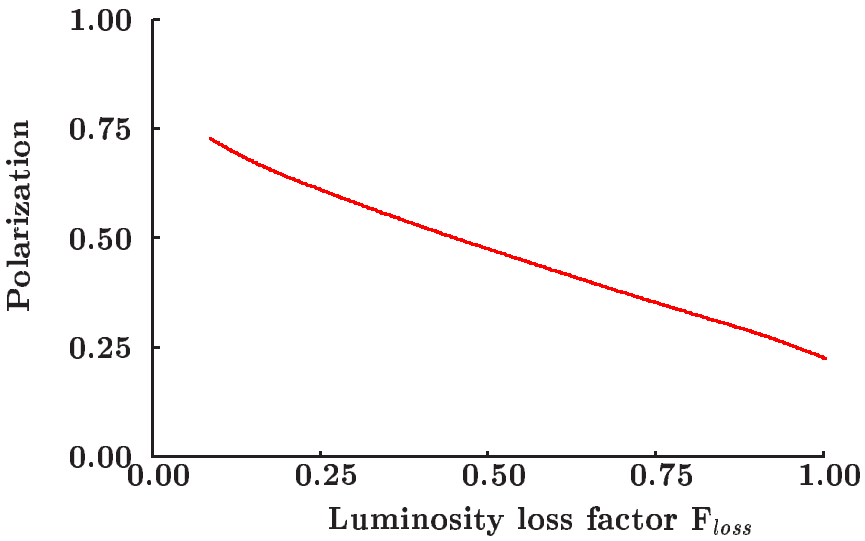

Figure 10: Polarization *vs.* fraction $F_{\rm loss}$ of μ's accepted.

If higher polarization is required, some selection of muons from forward pion decays ($\cos\theta_d \to 1$) is required. Figure 8 shows the polarization of the phase-rotated muons. The polarization {P$> \frac{1}{3}$, $-\frac{1}{3} < P < \frac{1}{3}$, and P$< -\frac{1}{3}$} is marked by the symbols $+$, **o** and $-$ respectively. If a selection is made on the minimum energy of the muons, then greater polarization is obtained. The tighter the cut, the higher the polarization, but the smaller the fraction $F_{\rm loss}$ of muons that remain. Figure 10 gives the results of a Monte Carlo study.

If this selection is made on both beams, and if the proton-bunch intensity is maintained, then each muon bunch is reduced by the factor $F_{\rm loss}$, and the luminosity would fall by $F_{\rm loss}^2$. But if, instead, proton bunches are merged so as to obtain half as many bunches with twice the intensity, then the muon-bunch intensity is maintained, and the luminosity (and repetition rate) falls only as $F_{\rm loss}$.

The luminosity could be maintained at the full unpolarized value if the proton-source intensity could be increased. Such an increase in proton-source intensity in the unpolarized case might be impractical because of the resultant excessive power in the high-energy-muon beam, but this restriction does not apply if the increase is used to offset losses in generating polarization.

Thus, the goal of high muon-beam polarization may shift the parameters of the muon collider towards lower repetition rate and higher peak currents at the pion-production target.

1.3 Summary of Critical Targetry Issues

There are several key issues which require laboratory studies before the targetry scenario can be placed on a firm basis:

1. What is the effect of the pressure wave induced in the target by the proton pulse? If the liquid target is dispersed by the beam, do the droplets damage the containment vessel?

2. What is the effect of the magnetic field of the capture solenoid on the motion of the liquid-jet target? Is the jet badly distorted by Lorentz forces on the eddy currents induced as the jet enters the field? Does the magnetic field damp the effects of the beam-induced pressure wave?

3. Can the first rf cavity of the phase-rotation channel operate viably in close proximity to the target?

4. What is the yield of low-energy pions from 16-24-GeV protons incident on the target of the muon-collider source?

5. Can numerical simulations of target behavior be developed that permit reliable extrapolation of the data we obtain?

The present understanding of questions 1-3 is discussed in sec. 2. Data relevant to question 4 has been collected by BNL experiment E-910 [23], the status of which is summarized in Appendix A. The proposed eight-part R&D program to address all of these questions is presented in sec. 3.

2 Critical Targetry Issues

2.1 Solid or Liquid Target?

The muons of a muon collider will arise from the decay of pions produced in the interaction of some 1.5×10^{15} protons/s on a primary target. If these protons have 16-GeV energy, the beam power is 4 MW. The target will be about 2 interaction lengths long and will absorb about 10% of the beam power, *i.e.*, about 400 kW. The beam repetition rate is 15 Hz, so each beam pulse deposits about 30 kJ of energy in the target.

2.1.1 Cooling the Target

The target is in the form of a cylinder, about 1 cm in radius, 30 cm in length, with a volume of about 100 cm^3. If the target material has density 10 g/cm^3, then the target mass is about 1 kg. Thus the beam-energy deposition in the target averages about 30 J/g. Taking the heat capacity of a typical metal as 0.2 J/(g-°K), the temperature rise of a metallic target is about 150°K per pulse. If the target were not cooled, it would melt (if solid) or boil (if liquid) after a dozen or so beam pulses.

However, the goal of collecting the maximal number of muons per proton is not consistent with typical cooling schemes in which the target material is in immediate contact with a large thermal reservoir.

Radiative cooling of the target appears to be unfeasible. The power radiated by a surface of area A and emissivity ϵ at temperature T is $\epsilon\sigma T^4 A$, where $\sigma = 5.67 \times 10^{-12}$ J/(cm^2(°K)^{4}s) is the Stefan-Boltzmann constant. The emissivities of typical metals are only about 0.2 (in contrast to carbon, with $\epsilon \approx 0.8$). The surface area of the target cylinder is about 200 cm^2. At 2000°K, the radiated power would be only 3.6 kW, well shy of the 400-kW beam load.

Thus, we are led to consider scenarios in which the target is in motion, with any subunit of the target exposed to only one or a few beam pulses before being transported away from the interaction region, to be cooled by a remote thermal reservoir. For similar reasons, targets at multimegawatt neutron spallation sources are expected to be based on flowing liquid metal, usually mercury [41, 42, 43, 44, 45, 46, 47].

2.1.2 Thermal Shock

The simplest option would be use of a flowing liquid metal contained within a (static) metal pipe [49, 50, 51]. However, when a large pulse of energy is deposited in a material in a time that is short compared to the transit time of a sound wave (≈ 3 μs/cm), a pressure (stress) wave results [52, 53, 43, 54, 55, 56, 57]. Since the proton pulse for a muon collider is expected to be only about 2 ns long, stress waves will be excited in the target, and consequent damage to the target and adjacent material is a concern.

This issue is often called "thermal shock". The pressure wave front propagates outwards at roughly the speed of sound in the target material. However, thermal shock is not necessarily associated with bulk transport of matter at the speed of sound.

The Initial Pressure Wave. If the beam-induced stress exceeded the tensile strength of the target material, the latter would fracture.

We present a simplified model to estimate the regime in which a pressure wave will "tear" the target apart, whether solid or liquid (see also refs. [52, 58]). When an energy density ΔU (per gram) is deposited quickly in the target, we first calculate the temperature change ΔT that would occur, assuming no thermal diffusion. Then, we calculate the strain, $\Delta l/l$ corresponding to that ΔT, and evaluate the stress P corresponding to that strain. Tearing is likely to occurs if the stress exceeds the tensile strength. In this model, tearing occurs during the phase of the pressure wave when the material is under tension, *i.e.*, for negative pressure. In liquids, this phenomenon is called cavitation [59, 60, 61].

We suppose that the effective tensile strength of a liquid metal is similar to that of the same metal in solid form. For example, the tensile strength of sea ice is reported as about 8 atm [62], while that of water can exceed 200 atm in a static measurement [63] but was measured as 8 atm by an explosive technique [64] that has much in common with the present concerns; see also [59, 60].

For most metals, the tensile strength (pressure) P is about 0.002 of the modulus of elasticity E (Young's modulus). Thus,

$$\Delta U = C\Delta T = \frac{C}{\alpha}\frac{\Delta l}{l} = \frac{C}{\alpha}\frac{P}{E} \approx 0.002\frac{C}{\alpha}, \tag{1}$$

where C is the heat capacity, α is the coefficient of thermal expansion, and the approximation holds on setting the stress equal to the tensile strength. If, for example, the heat capacity is $C = 0.3$ J/g-°C, and $\alpha \approx 2 \times 10^{-5}$/°C, then we expect the target material will tear when $\Delta U \approx 30$ J/g. This is very nearly the expected energy deposition in the muon-collider target. It is, however, somewhat smaller than a semi-empirical value of 200 J/g for the threshold for thermal-shock damage [65].

If the target tears, it is possible that the fragments do damage to the surrounding vessel. If all the deposited energy were converted to kinetic energy and the target fragmented completely, then the velocity of the fragments would be $\sqrt{2\Delta U} \approx 8$ m/s for $\Delta U = 30$ J/g. A model of spray velocities in explosions of liquids [64] leads to similar values. Studies of an exploding mercury jet were performed safely inside a plastic vessel whose wall was only $1/4''$ thick [66, 67, 68]. Thus, it is encouraging that if a liquid target were dispersed into droplets by the beam, the droplets would do little damage to the surrounding vessel. However, this should be confirmed by experiment.

The Reflected Pressure Wave. Even if target parameters are chosen such that the initial pressure wave does not tear the material, there is another concern. When the pressure wave reaches the surface of the target, it will, in general, be reflected. In the case of a cylindrical target, the reflected wave converges on the axis of the target and will typically result in higher peak pressures than exist in the initial outgoing wave. Hence, there is a serious prospect for localized fracture or vaporization of the target material close to the target axis, whether the cylindrical target is solid or liquid. In the case of a liquid, this is likely to induce localized damage to the target pipe, particularly on the upstream wall.

The destructive effects of pressure waves and cavitation on liquid-metal targets in pipes have been demonstrated at the CERN ISOLDE facility [24, 69], as shown in Figs. 11-12, and also at the Budker Institute [25], as shown in Fig. 13. Practical targets based on liquid metals in pipes require sufficiently long beam pulses and/or target geometries (*e.g.*, planar) in which

Figure 11: Full-scale model of an ISOLDE target consisting of a 2-cm-diameter, 20-cm-long tantalum cylinder containing molten lead.

Figure 12: Photograph of an ISOLDE liquid-lead target that ruptured around the upstream window after a few beam pulses [24].

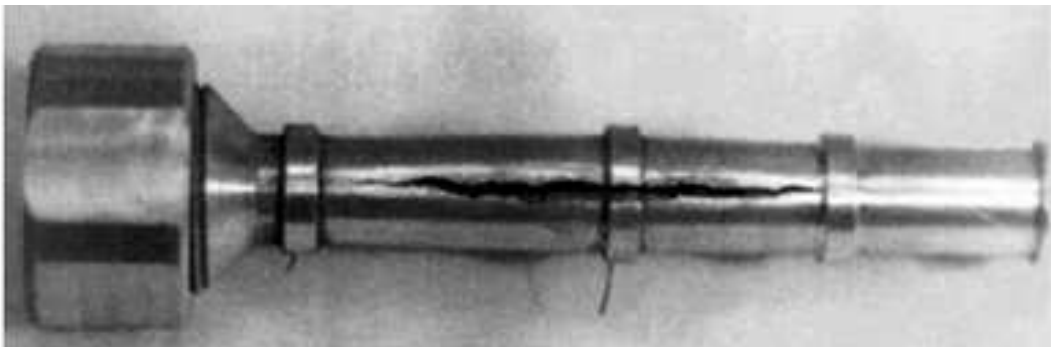

Figure 13: Photograph of a mercury target contained in an aluminum cylinder that ruptured after exposure to a beam that deposited 1 kJ/g per pulse [25].

imploding pressure waves do not occur. Therefore, liquids in pipes are not considered further for a muon-collider target. Likewise, a moving solid cylindrical target is very problematic at a muon collider.

2.1.3 Muon-Collider Primary-Target Options

The remaining options for the muon-collider target are a free, cylindrical liquid-metal jet or a moving planar solid target, as have been sketched in Figs. 4 and 7. The baseline design to be studied in the proposed R&D program utilizes a free liquid-metal jet. The moving band target presently is considered as the backup option.

2.1.4 Additional Issues for a Solid Target

As well as surviving the thermal-shock of each beam pulse, a solid target must survive the long-term effects of radiation damage. These include embrittlement, swelling and even fracture of the material due to displacement damage and hydrogen/helium production [70]. The immunity of a liquid target to these effects is an argument in favor of that option.

The cross section for displacement of a target atom in a 16-30-GeV proton beam is about 10^{-24} m^2. In an operational year of 10^7 s, a beam of 1.5×10^{15} proton/s whose rms radius is nominally 4 mm results in about 300 displacements per atom (dpa) in a nonmoving target.

For a moving solid target, any given atom is exposed to a proton flux that is less than the total by the factor

$$\frac{L_{\rm int} N_{\rm overlap}}{L_{\rm total}}, \tag{2}$$

where $L_{\rm int}$ is the length of the interaction region ($\approx$ 30 cm), $L_{\rm total}$ is the total length of the target material ($\approx$ 30 m, say), and $N_{\rm overlap}$ is the number of adjacent beam pulses that irradiate a given region. That is,

$$N_{\rm overlap} = \frac{L_{\rm int} f}{v}, \tag{3}$$

for a target moving with velocity v along the beam whose pulse rate is f Hz. For example, with $v = 1$ m/s and $f = 15$ Hz, then $N_{\rm overlap} \approx 5$, and each part of the moving target

experiences only 5% of the exposure of a nonmoving target, namely about 15 dpa in a year of operation. This still corresponds to significant radiation damage, suggesting that the target band would need to be replaced several times a year. The viability of a moving solid target needs further investigation.

There is little available evidence as to the mechanical properties of targets after such exposures. A series of studies of solid targets at CERN generally indicated severe mechanical damage to intensely irradiated targets [71, 72, 73, 74, 75, 76], although the damage was due to a combination of single-pulse shock as well as radiation. Nickel targets appear to survive well for energy depositions up to a large fraction of the shock-damage threshold [77]. Copper targets appear to form excessive amounts of copper sulfate if irradiated in contact with air [78].

2.2 Beam-Induced Radioactivity

The high flux of protons into the target will induce some radioactivity no matter what the target consists of. A thorough study of this issue will be needed before a final decision as to the target material is taken. A first study will be made using a MARS simulation of the hadronic cascade in the target.

For any target material with an atomic number greater than or equal to that of mercury, radioactive isotopes of mercury will emerge in the vapor phase [79]. These are only the most prominent among other radioactive vapors that will be produced. Hence, a high-Z target at a muon-collider source must be enclosed in a gas-tight system that includes capture tanks for the vapors, including those exhausted from any pumps. This proposal does not cover R&D towards such a system, which would be modeled after the target-containment system at the ISOLDE facility at CERN.

Especially high levels of activity would arise for targets containing bismuth, due to the sequence:

$$\text{Low-energy neutron} + \mathrm{Bi}^{209}_{83} \rightarrow \mathrm{Bi}^{210}_{83} + \gamma, \qquad \mathrm{Bi}^{210}_{83} \rightarrow \mathrm{Po}^{210}_{84} + \beta^- \quad (\text{half life} = 5 \text{ days}). \tag{4}$$

Po^{210} has a half life of 135 days and decays primarily via a 5.3-MeV α, but has a 0.1% branch to an 803-keV x-ray.

If, say, every beam proton results in one transmutted Bi atom, then the steady-state Po population would be equal to the total flux of protons in 135 days: $135 \times 10^5 \times 10^{15} \approx 10^{22}$ atoms, assuming a proton flux of 10^{15}/s. The number of Po decays would be 10^{15}/s in the steady state, *i.e.*, about 30,000 curies!

The α-particles will be almost entirely absorbed in the target, but the 800-keV x-rays present more of a problem. The steady-state strength of the x-rays corresponds to about 30 curies (assuming each beam proton results in one Po atom).

However, the resulting polonium would be dissolved in the liquid of the target with very low probability of being in vapor molecules. Hence, the handling of an activated bismuth alloy would be relatively straightforward and little more difficult than for other target materials [80].

2.3 Candidate Liquid Metals

Liquid metals have long been used as coolants for nuclear reactors, and a useful summary of candidate materials has been given by Lyon [81]. Table 2 presents a brief survey of low-melting-temperature metals, and Table 3 list some relevant physical properties of the elements of candidate materials.

Table 2: Survey of low-melting-temperature metals [81].

Approximate melting point, °C	Approximate composition, wt %
185	48 bismuth, 52 thallium (eutectic)
180	38 lead, 62 tin (eutectic)
140	60 bismuth, 40 cadmium (eutectic)
140	58 bismuth, 42 tin (eutectic)
130	56 bismuth, 40 tin, 4 zinc (eutectic)
125	44.5 bismuth, 55.5 lead (eutectic)
120	25 cadmium, 75 indium (eutectic)
117	48 tin, 52 indium (eutectic)
105	48 bismuth, 28.5 lead, 14.5 tin, 9.0 antimony (matrix alloy)
93	50 bismuth, 25 lead, 25 tin
91.5	51.6 bismuth, 40.2 lead, 8.2 cadmium (eutectic)
71.7-69.7	50 bismuth, 25 lead, 12.5 tin, 12.5 cadmium (Wood's metal)
70	33 bismuth, 67 indium (eutectic)
70	50 bismuth, 26.7 lead, 13.3 tin, 10 cadmium (eutectic)
60.5	32.5 bismuth, 16.5 tin, 51 indium
58.2	49.5 bismuth, 17.6 lead, 11.6 tin, 21.3 indium
46.5	40.63 bismuth, 22.11 lead, 10.65 tin, 8.2 cadmium, 18.1 indium
33	32 potassium, 68 rubidium (eutectic)
17	12 tin, 6 zinc, 82 gallium (eutectic)
10.8	12.5 tin, 17.6 indium, 69.8 gallium (eutectic)
10.7	16 tin, 21.5 indium, 62.5 gallium (eutectic)
−8	8 sodium, 92 rubidium (eutectic)
−11	22 sodium, 78 potassium (eutectic)
−30	5 sodium, 95 cesium (eutectic)
−40	87 cesium, 13 rubidium (eutectic)
−48	23 potassium, 77 cesium (eutectic)

We are interested in high-Z, high-density target materials for the most-efficient pion production. High electrical resistivity is helpful in reducing the eddy-current problem of a jet entering a magnetic field (sec. 2.5).

In many ways mercury is an excellent candidate, but its vapor is toxic. Also, it may be preferable to use a material that is solid at room temperature, to simplify cleanup of spills.

Table 3: Properties of some candidate elements for primary targets.

Element	Z	Density (g/cm^3)	Melting Temp. (°C)	Boiling Temp. (°C)	Heat Cap. (J/g-°C)	Heat of Vapor. (J/g)	Thermal Cond. (W/cm-°C)	Resist. ($\mu\Omega$-cm)	Thermal Exp. (10^{-5}/°C)
Copper	29	8.96	1087	2567	0.39	4796	4.01	1.7	1.7
Zinc	30	7.1	420	906	0.39	1733	1.16	6.0	3.1
Gallium	31	5.9	30	2204	0.33	3712	0.4	26†	12
Indium	49	7.3	156	2073	0.23	2016	0.82	10	3.2
Tin	50	7.3	232	2270	0.18	2487	0.67	13	2.2
Mercury	80	13.6	−39	357	0.14	295	0.087	94†	6.1
Lead	82	11.35	327	1750	0.16	858	0.35	80†	2.9
Bismuth	83	9.7	271	1610	0.12	857	0.079	120	1.3

† liquid

Lead alloys (solder-like materials) are good candidates. Rather low melting temperatures are obtained by alloying with indium, which, however, wets most solid metals so much as to make it difficult to produce liquid jets. Lead-bismuth alloys have the drawback of relatively high production of polonium when activated by the proton beam. Gallium alloys are nontoxic and can be liquid at room temperature, so the resulting ease of handling indicates their use in the initial stages of the R&D program. The relatively low atomic number, low density and low resistivity of gallium is somewhat undesirable for use in the final target.

2.3.1 Mercury

Studies of materials issues for use of mercury as a proton target include refs. [43, 82, 83, 84]. The tensile strength of liquid mercury has been studied by Briggs [85].

2.3.2 Lead Alloys

A lead alloy of particular interest is eutectic lead-bismuth, 45% Pb by weight, with a melting point of 126°C (255°F). Other interesting low-melting allows of lead and/or bismuth are made by adding cadmium, indium or tin. Some quaternary and quinternary alloys have extremely low melting temperature, such as alloys 117 and 136 (designated by their melting temperatures in °F). Table 4 gives a summary of physical properties of several commercial lead alloys.

Table 4: Lead Alloy Specifications from Belmont Metals. See also `http://www.indium.com/fusiblealloys.html`

Th: Kirk McDonald

Bob $96.80 $18/30

$51.35LB $13.25

$84.45

Belmont
METALS INC.
330 Belmont Avenue, Brooklyn, New York 11207
(718)-342-4900 • TWX 710-584-2296 • FAX 718-342-0175

SHEET

BELMONT LOW MELTING ALLOYS - Used as Production Aids

PHYSICAL PROPERTIES & NOMINAL COMPOSITION	EUTECTIC ALLOYS					NON EUTECTIC ALLOYS		
	BELMONT ALLOY 2451	BELMONT ALLOY 2491	BELMONT ALLOY 2505	BELMONT ALLOY 2562	BELMONT ALLOY 2581	BELMONT ALLOY 2431	BELMONT ALLOY 2481	BELMONT ALLOY 2405
Melting Temperature (°F.) Range (°F.)	~~117~~ 117-117	~~136~~ 136-136	~~158~~ 158-158	~~255~~ 255-255	~~281~~ 281-281	(No definite melting point, see yield temp.) 160-190	218-440	281-338
Yield Temp. (°F.)	117	136	158	255	281	162.5	240	302
Weight Lb./In.³	.32	.31	.339	.380	.315	.341	.343	.296
Specific Gravity 20°C	8.9	8.8	9.4	10.3	8.7	9.4	9.5	8.2
Tensile Lb./In.²	5400	6300	5990	6400	8000	5400	13000	8000
*Elongation in 2" Slow Loading %	1.5	50	200	60-70	200*	220*	Less than 1%	200*
Brinell Hardness #	12	14	9.2	10.2	22	9	19	22
*Specific Heat Liquid	.035	.032	.040	.042	.045	.040	.04	.047
*Specific Heat Solid	.035	.032	.040	.03+	.045	.040	.045	.047
*Latent Heat — Fusion Btu./LB.	6	8	14	7.2	20	10		22
*Coefficient of Thermal Expansion	.000025/°C.	.000023/°C.	.000022/°C.	.000021/°C.	.000015/°C.	.000024/°C.	.000022/°C.	.000015/°C.
Thermal Conductivity (Solid) Cal/Cm²/°C/Sec .94 = Copper	—	—	*.045	*.04	*.05	*.05	—	*.09
Conductivity (Electrical) Compared with Pure Copper	3.34%	2.43%	4.17%	1.75%	5.00%	4.27%	2.57%	7.77%
Resistivity, OHMS based on volume standard (Meter, MM²)	.5180	.7081	.4135	.8825	.3445	.4037	.6696	.2219
*Maximum Load — 30 Seconds Lb. — In.²			10000	8000	15000	9000	16000	15000
*Maximum Load — 5 Minutes Lb. — In.²			4000	4000	9000	3800	10000	9500
*Safe Load — Sustained Lb. — In.²			300	300	500	300	300	500
Volume Change (Liquid to Solid)	—1.4%	—1.35%	—1.7%	—1.5%	+0.77%	*—2.0%	—1.5%	*+0.5%
Volume Change (Linear growth after solidification.)	Less Than 0.05%	Less Than 0.05%	0.6%	0.3%	0.05%	0.3%	0.5%	*0%
GROWTH/SHRINKAGE CHARACTERISTICS TIME AFTER CASTING	FIGURES INDICATED ARE IN INCHES PER INCH AS DETERMINED FROM CUMULATIVE GROWTH MEASURED AS THE DIFFERENCE IN LENGTH BETWEEN MOLD AND TEST BAR DIMENSIONS IN A TEST BAR ½" x ½" x 10".							
2 Minutes	+.0005	+.0003	+.0025	—.0008	+.0007	—.0004	+.0008	—.0001
6 Minutes	+.0002	+.0002	+.0027	—.0011	+.0007	—.0007	+.0014	—.0001
30 Minutes	.0000	+.0001	+.0045	—.0010	+.0006	—.0009	+.0047	—.0001
1 Hour	—.0001	.0000	+.0051	—.0008	+.0006	.0000	+.0048	—.0001
2 Hours	—.0002	—.0001	+.0051	—.0004	+.0006	+.0016	+.0048	—.0001
5 Hours	—.0002	—.0002	+.0051	.0000	+.0005	+.0018	+.0049	—.0001
7 Hours	—.0002	—.0002	+.0051	+.0001	+.0005	+.0019	+.0050	—.0001
10 Hours	—.0002	—.0002	+.0051	+.0003	+.0005	+.0019	+.0050	—.0001
24 Hours	—.0002	—.0002	+.0051	+.0008	+.0005	+.0022	+.0051	—.0001
96 Hours	—.0002	—.0002	+.0053	+.0015	+.0005	+.0025	+.0055	—.0001
200 Hours	—.0002	—.0002	+.0055	+.0019	+.0005	+.0025	+.0058	—.0001
500 Hours	—.0002	—.0002	+.0057	+.0022	+.0005	+.0025	+.0061	—.0001
Compositions (%):								
Bismuth	44.7	49.0	50.0	55.5	58.0	42.5	48.0	40.0
Lead	22.6	18.0	26.7	44.5		37.7	28.5	
Tin	8.3	12.0	13.3		42.0	11.3	14.5	60.0
Cadmium	5.3		10.0			8.5		
Other	Indium 19.1	Indium 21.0					Antimony 9.0	

* APPROXIMATE VALUES

We have verified that the resistivities of liquid-lead alloys are very similar to those of the corresponding solid, as listed in Table 4 [28].

An extensive literature exists on materials-handling issues for applications of lead alloys at nuclear reactors [86, 87, 88, 89, 90, 91].

2.3.3 Gallium and Gallium Alloys

Some information on liquid gallium alloys can be found at
`http://www.indium.com/liquidalloys.html`

The eutectic Ga-Sn alloy is particularly convenient, as it is a liquid at room temperature. It is easy to prepare by dissolving tin wire (but not powder) in liquid gallium at 40-50°C. The binary phase diagram for Ga-Sn is shown in Fig. 14.

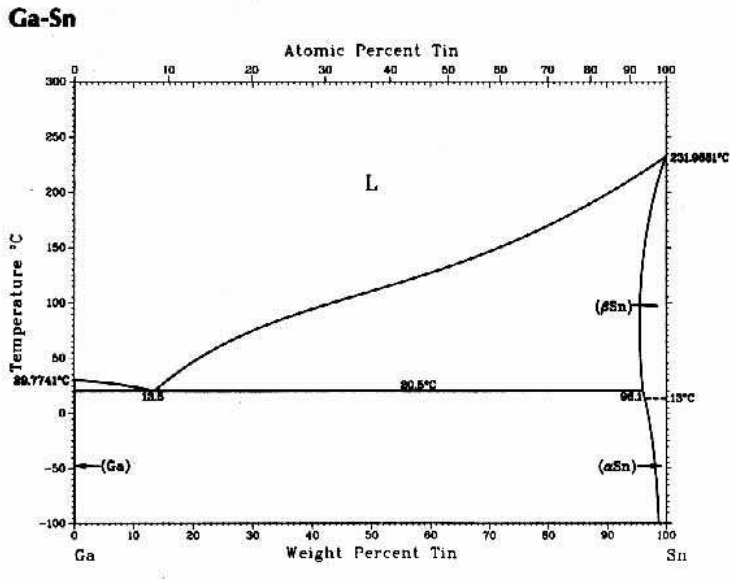

Figure 14: Ga-Sn phase diagram. Minimum melting temperature = 20.5°C [92].

Liquid gallium has a viscosity of 1.6 cp/g-cm^3, only slightly highly than that of water. The temperature dependence of the resistivity of gallium has been studied in detail [93]. Liquid gallium has been used as a coolant for silicon crystals at synchrotron light sources [94, 95].

2.3.4 Exotic Target Materials

The interaction of moving metals with the 20-T capture magnet (sec. 2.5) could be avoided by use of insulating liquids such as molten PtO_2 or Re_2O_3, or by granular materials such as slurries (*e.g.*, Pt in water) or powders [31].

The problem of beam-induced thermal shock (sec. 2.1.2) might be minimized by use of materials with very low (or negative) thermal expansion coefficients [27]. For example, Invar alloys have been studied for many years, and their properties are well known. Other

materials are less well understood. For example, oxides such as ZrW_2O_8 produce a net contraction over a range of 1-1200°K. Bismuth ice slurries have the property, like water ice, of contracting when melting. Aqueous salt suspensions such as iron formate and sodium chloride contract with heating due to a molecular electrostrictive effect. Molecular liquids such as molten SiO_2 exhibit a negative thermal expansion in the region of 1700°C due to a molecular-bond modification.

Bubbly liquids may also have a higher compressibility, which would make them useful [43].

2.4 Jet Velocity

To be useful as a target, a pulsed liquid jet must have a minimum velocity, so that each pulse is sufficiently distinct from the others, and so that the jet is reasonably straight. The minimum velocity for a conductive jet to enter a strong magnetic field is considered in sec. 2.5.

2.4.1 Effect of 15-Hz Repetition Rate

We consider the use of a pulsed jet, leading to a series of cylinders of liquid, each of length l and radius r, and moving with velocity v. The frequency f of the pulse is nominally 15 Hz.

If the material from one pulse is not to overlap that of the next, then the jet velocity must obey

$$v > fl. \tag{5}$$

For example, if the length of each pulse is be about two nuclear interaction lengths (about 30 cm for a dense, high-Z material), then with $f = 15$ Hz, we need $v > 4.5$ m/s.

The jet velocity will have to be several times this to create gaps between adjacent pulses, so that the proton beam interacts with only a single jet pulse.

2.4.2 Effect of Gravity

The trajectory of the jet will be a parabolic arc, due to the acceleration of gravity. If the jet velocity were too low, the curvature of the jet would be large, and the proton beam would not be able to intersect the jet pulse over its whole length.

The ends of the jet are displaced downward from the ideal straight trajectory by amount

$$\Delta y = \frac{gt^2}{2} = \frac{gl^2}{8v^2}, \tag{6}$$

noting that the time for the center of the jet to reach its end is $t = l/2v$. For example, with $\Delta y = 1/8$ cm, as might be desired for a jet of radius 1 cm, $l = 30$ cm, we find $v \approx 1000$ cm/s $= 10$ m/s.

Thus, the effects of pulse frequency and of gravitational curvature both require the jet velocity to be at least 10 m/s.

2.4.3 Jet Velocity *vs.* Pressure

Suppose the liquid metal is stored in a tank of area A perpendicular to the flow, and the pressure is P above ambient. A valve lets a jet of liquid escape through an aperture of area $a \ll A$.

Then Bernoulli's equation tells us that the flow velocity v out the aperture obeys

$$\frac{1}{2}\rho v^2 = P + \frac{1}{2}\rho V^2, \tag{7}$$

where ρ is the density of the liquid and V is the velocity of the liquid surface of area A in the tank. The equation of continuity for an incompressible liquid tells us that $av = AV$, so that

$$v = \sqrt{\frac{2P}{\rho(1-(a/A)^2)}} \approx \sqrt{\frac{2P}{\rho}}. \tag{8}$$

For example, with a Bi-Pb alloy of density $\rho \approx 10$ g/cm^3,

$$v[\mathrm{m/s}] \approx \sqrt{20P[\mathrm{atm.}]}. \tag{9}$$

Thus, to reach $v = 4.5$ m/s would require 1 atm overpressure in the storage tank; 20 atm would be required to reach a velocity of 20 m/s.

2.5 The Interaction of a Liquid-Metal Jet with a Magnetic Field

As a jet of liquid metal enters the magnetic field that surrounds the beam interaction region, it will be repelled according to Lenz' law. The effect is due to the Lorentz force on the eddy currents induced in the moving metal. In an extreme case the jet would not reach the center of the interaction region.

Here we present simplified analytic estimates of the effects of eddy currents, and reach the tentative conclusion that they would visibly alter the trajectory of the liquid-metal jet, but would not prevent the jet from functioning as a target. However, there appears to be little safety margin, suggesting the need for laboratory experiments to confirm that the proposed liquid-metal jet is viable.

Additional details of the analytic arguments can be found in refs. [28, 29, 30].

It is useful to establish numerical values for some relevant parameters of our system as a qualitative guide to its magnetohydrodynamic behavior.

First, we note that the problem of a moving conductor in a static magnetic field is equivalent to a moving field that encounters a conductor initially at rest. Thus, the electric field $\mathbf{E}'$ in the frame of the conductor is related to the electric and magnetic fields $\mathbf{E}$ and $\mathbf{B}$ in the lab frame by

$$\mathbf{E}' = \mathbf{E} + \mathbf{v} \times \mathbf{B}, \tag{10}$$

where $\mathbf{v}$ is the laboratory velocity of the conductor ($v \ll c$), and we use MKSA units.

Next, we recall that the penetration of a time-dependent magnetic field into a conductor is governed by a diffusion equation. Assuming $v \ll c$ and reasonably good conductivity σ, we may neglect the displacement current, and the basic electromagnetic equations are

$$\nabla \times \mathbf{E} = -\frac{\partial \mathbf{B}}{\partial t}, \qquad \nabla \times \mathbf{B} = \mu_0 \mathbf{j}, \qquad \text{and} \qquad \mathbf{j} = \sigma \mathbf{E}' = \sigma(\mathbf{E} + \mathbf{v} \times \mathbf{B}), \tag{11}$$

where $\mathbf{j}$ is the current density. On eliminating $\mathbf{j}$ and $\mathbf{E}$ we find that

$$\frac{\partial \mathbf{B}}{\partial t} = \frac{\nabla^2 \mathbf{B}}{\mu_0 \sigma} + \nabla \times (\mathbf{v} \times \mathbf{B}). \tag{12}$$

With the neglect of the second term (justified for low velocity), we find the desired diffusion equation. Thus, the characteristic time for diffusion of the magnetic field into a long conducting cylinder of radius r is

$$\tau = \mu_0 \sigma r^2. \tag{13}$$

The low-melting temperature alloys in Table 4 all have relatively low conductivity. In particular, alloy 255 has conductivity only 2% that of copper (resistivity = 1.67 $\mu\Omega$-cm), *i.e.*, about 10^6 MKSA units. Hence, for a cylinder of radius 1 cm the diffusion time is

$$\tau \approx 4\pi \times 10^{-7} \cdot 10^6 (10^{-2})^2 \approx 10^{-4} \text{ sec.} \tag{14}$$

Another characteristic time in our problem is that over which the external magnetic field varies appreciably. For a jet of velocity v that enters a solenoid of diameter D, this time is D/v. The ratio of the diffusion time to time D/v is called the magnetic Reynold's number:

$$\mathcal{R} = \frac{\tau v}{D}. \tag{15}$$

For $\mathcal{R} \ll 1$ the external magnetic field penetrates the conductor, but for $\mathcal{R} \gg 1$ it does not.

Anticipating a jet velocity of order 10 m/s and a solenoid of diameter $D \approx 0.3$ m, we have $D/v \approx 0.03$ s, and the magnetic Reynold's number is $\mathcal{R} \approx 0.003$. We conclude that in our problem the diffusion is rapid enough that the external field penetrates the conductor. That is, our candidate metals are not sufficiently "good" conductors to exclude the magnetic field from their interior. This is fortunate, as a "good" conductor could not enter a 20-T magnetic field unless its initial velocity were very high.[4]

The magnetic Reynold's number can be thought of in another way. From the point of view of the conductor, the external magnetic field is time dependent with frequency content up to $\omega \approx v/D$. The skin depth at this frequency is $\delta = \sqrt{2/\mu_0 \omega \sigma} = \sqrt{2D/\mu_0 \sigma v}$. This is to be compared to the radius r of the conductor. Indeed,

$$\frac{r^2}{\delta^2} = \frac{\mu_0 \sigma r^2 v}{2D} = \frac{\mathcal{R}}{2}. \tag{16}$$

In our case, the low value of the magnetic Reynold's number indicates that the conductor is much smaller than the relevant skin depth, and again we expect the external field to penetrate the conductor.

We now give some approximate analyses of the forces on the liquid jet as it enters a solenoid.

[4]To see this, consider a good conductor moving along the z-axis of a solenoid field. Surface current $I = B_z/\mu_0$ (per unit length) is induced so as to cancel the external solenoid field B_z. This current interacts with the radial component of the external field, $B_r \approx -(r/2) dB_z(0,z)/dz = -rB_z'/2$ to produce retarding force $F = -2\pi r I B_r = -2\pi r (B_z/\mu_0)(rB_z'/2) = \pi r^2 (B_z^2)'/2\mu_0$ per unit length. But also, $F = ma = \pi r^2 \rho \dot{v} = \pi r^2 \rho v v' = \pi r^2 \rho (v^2)'/2$, where $\rho \approx 10^4$ kg/m^3 is the mass density. This integrates to give $v^2(z) = v_{-\infty}^2 - B_z^2/\mu_0 \rho$. Thus, to enter a field of $B_z = 20$T, the initial velocity would need to be at least $B_z/\sqrt{\mu_0 \rho} \approx 200$ m/s for our heavy metals.

2.5.1 Jet on Axis of a Solenoid

We model the forces on a conducting jet in a magnetic field by considering only a ring (or disc) perpendicular to the axis of the jet. The ring has radius r, radial extent Δr and thickness Δz.

We first consider only motion along the axis of the ring, which we call the z axis, and which is also the axis of a solenoid magnet with field $\mathbf{B}(r, z)$.

Then the magnetic flux through the ring at position z is

$$\Phi \approx \pi r^2 B_z(0, z), \tag{17}$$

whose time rate of change is

$$\dot{\Phi} = \pi r^2 \dot{B}_z = \pi r^2 B_z' v, \tag{18}$$

where $\dot{}$ indicates differentiation with respect to time, $'$ is differentiation with respect to z, B_z stands for $B_z(0, z)$, and v is the velocity of the center of mass of the ring.

If the metal has electrical conductivity σ, then its resistance to currents around the ring is

$$R = \frac{2\pi r}{\sigma \Delta r \Delta z}, \tag{19}$$

so the (absolute value of the) induced current is

$$I = \frac{\mathcal{E}}{R} = \frac{\dot{\Phi}}{R} = \frac{\sigma r B_z' v \Delta r \Delta z}{2}. \tag{20}$$

Radial Pinch. The Lorentz force on the ring due to the interaction of this current with the axial field pinches the jet radially, while that due to the interaction with the radial field opposes the motion. The radial pinch can be characterized by a radial pressure gradient,

$$\frac{\Delta P_r}{\Delta r} = \frac{\Delta F_r}{\Delta r \Delta z \Delta l} = -\frac{B_z I \Delta l}{\Delta r \Delta z \Delta l} = -\frac{\sigma r B_z B_z' v}{2}. \tag{21}$$

As the jet enters the magnet from $z = -\infty$, the axial field gradient, B_z', is initially positive, and the radial forces are inward. However, as the jet exits the solenoid, the gradient B_z' becomes negative, and the radial force is outwards. Even if the jet has not been destabilized by the pinch on entering the magnetic, the radially outward forces experienced on leaving the magnet may disperse the jet.

The pinch is greatest as the ring passes the edge of the solenoid, where $B_z \approx B_0/2$ and $B_z' \approx B_0/D$ for a solenoid of diameter D and peak axial field B_0. That is,

$$\frac{\Delta P_{r,\max}}{\Delta r} \approx -\frac{\sigma}{4}\frac{r}{D} B_0^2 v. \tag{22}$$

Integrating this over radius, the pressure gradient between the axis and radius r is

$$\Delta P_{r,\max} \approx -\frac{\sigma}{8}\frac{r^2}{D} B_0^2 v. \tag{23}$$

In general, the pinch will cause the jet to shrink radially and elongate axially. Instabilities in this process may break the jet up into droplets. However, once the jet begins to deform, additional eddy currents are induced that will oppose the deformation. See sec. 2.5.2.

As a very crude model of the effect of the pinch on the radius of the jet, we suppose that the jet surface accelerates inwards during the characteristic time D/v under a force approximated by the pinch pressure $\Delta P_{r,\max}$ times the surface area. Then eq. (23) leads to the estimate

$$\Delta r \approx -\frac{\sigma}{16}\frac{rD}{\rho v}B_0^2 \tag{24}$$

for the radial perturbation caused by the pinch.

Axial Retarding Force. The component of the Lorentz force that opposes the motion of the ring is

$$\Delta F_z = 2\pi r B_r I = -\pi\sigma r^2 B_r B_z' v \Delta r \Delta z \approx -\frac{\pi\sigma r^3 (B_z')^2 v \Delta r \Delta z}{2}, \tag{25}$$

using the approximate relation for the radial field near the z-axis,

$$B_r(r,z) \approx -\frac{r}{2}\frac{dB_z(0,z)}{dz} = -\frac{rB_z'}{2}, \tag{26}$$

as can be deduced from the Maxwell equation $\nabla \cdot \mathbf{B} = 0$.

The equation of motion of a ring is then

$$dF_z = -\frac{\pi\sigma r^3 (B_z')^2 v_z \Delta r \Delta z}{2} = m\dot{v}_z = 2\pi\rho r \Delta r \Delta z v_z' v_z, \tag{27}$$

where ρ is the mass density of the metal. After dividing out the common factor of $\pi r \Delta r \Delta z v_z$ we find

$$v_z'(r) = -\frac{\sigma r^2 (B_z')^2}{4\rho}. \tag{28}$$

Before considering a detailed model of the axial field profile, B_z, we note that the peak gradient of the axial field of a solenoid of diameter D is B_0/D, and the gradient is significant over a region $\Delta z \approx D$. Hence, we estimate that on entering a solenoid the jet velocity is reduced by an increment

$$\Delta v_z(r) \approx \frac{\sigma r^2 B_0^2}{4\rho D}. \tag{29}$$

On leaving the solenoid, the jet velocity is reduced by a second increment Δv_z. (Since the effect depends on $(B_z')^2$, the force is retarding on both entering and exiting, as predicted by Lenz' law.)

The jet velocity cannot actually go negative whatever the magnetic field . If the velocity reaches zero, the jet stops (falls). Note that we divided eq. (27) by v_z before integrating; once v_z becomes zero, F goes to zero and stays there.

The reduction of velocity (29) is zero on the axis of the jet, and grows quadratically with radius. If the jet were a rigid body, Δv_z would be one half the value given by eq. (29) at the outer radius.

If the change in velocity is small compared to the initial velocity, $v_{-\infty}$, we estimate the distance $\Delta z(r)$ by which the material in the jet at radius r is retarded compared to the material on axis as

$$\Delta z(r) \approx \Delta v_z(r) \Delta t \approx \Delta v_z(r) \frac{D}{v_{-\infty}} \approx \frac{\sigma r^2 B_0^2}{4\rho v_{-\infty}}. \tag{30}$$

We desire this to be small compared to the length of the jet. Indeed, it will be awkward if Δ_z exceeds the radius of the jet.

We now consider a more specific model. See [28] for discussion of a finite solenoid.

Semi-Infinite Solenoid. The field on the axis of a semi-infinite solenoid is amenable to analytic calculation. Indeed, for a solenoid of radius $D/2$ with windings from $z = 0$ to $+\infty$, the axial field is

$$B_z(0,z) = \frac{B_0}{2}\left(1 + \frac{z}{\sqrt{(D/2)^2 + z^2}}\right), \tag{31}$$

whose derivative is

$$B_z' = \frac{dB_z(0,z)}{dz} = \frac{B_0}{2}\frac{(D/2)^2}{[(D/2)^2 + z^2]^{3/2}}. \tag{32}$$

Using eq. (32) in eq. (28) and integrating the equation of motion from $-\infty$ to z, we find

$$v_z(r,z) = v_{-\infty} - \frac{3\sigma r^2 B_0^2}{64\rho D}\left(\frac{\pi}{2} + \tan^{-1} w + \frac{w}{1+w^2} + \frac{2w}{3(1+w^2)^2}\right), \tag{33}$$

where D is the diameter of the solenoid and $w = 2z/D$.

The semi-infinite solenoid is meant to approximate a finite solenoid of length $L = \alpha D$. Since the semi-infinite coil begins at $z = 0$, the center of the finite solenoid it approximates is at $z = \alpha D/2$, *i.e.*, at $w = \alpha$. For $\alpha \gtrsim 1$, as is reasonable for an actual magnet, there is little difference between the result of eq. (33) at $w = \alpha$ and at $+\infty$, so we estimate the change in velocity as

$$\Delta v_z(r) \approx -\frac{3\pi\sigma r^2 B_0^2}{64\rho D}. \tag{34}$$

The retardation relative to the center of the jet is related by

$$\Delta\dot{z}(r) = \Delta v_z(r) = \Delta z' v_z \approx \Delta z' v_{-\infty}, \tag{35}$$

where the approximation holds if $\Delta v_z \ll v_{-\infty}$. In this approximation, we integrate eq. (33) to find

$$\Delta z(r) \approx -\frac{3\sigma r^2 B_0^2 w}{128\rho v_{-\infty}}\left(\frac{\pi}{2} + \tan^{-1} w - \frac{1}{3w(1+w^2)}\right). \tag{36}$$

This diverges for large w, but at $w = \alpha \approx 1$, corresponding to the center of a real magnet, we have

$$\Delta z(r) \approx -\frac{3\pi\sigma r^2 B_0^2 \alpha}{128\rho v_{-\infty}}. \tag{37}$$

Numerical Examples. We consider the lead-bismuth alloy 255, whose conductivity is about 10^6 MKSA units and whose density is about 10 gm/cm^3, *i.e.*, 10^4 kg/m^3. Then, eq. (34) leads to the requirement

$$v_{-\infty} > 60 \text{ m/s}\left[\frac{r}{1 \text{ cm}}\right]\left[\frac{r}{D}\right]\left[\frac{B_0}{20 \text{ T}}\right]^2. \tag{38}$$

It is thought that the jet radius must be 0.5-1 cm to match the proton beam, and that the inside diameter of the solenoid will be about 20 cm. In this case we need $v_{-\infty} > 0.75$-3 m/s for $B_0 = 20$ T.

Again, if the jet is to exit the magnet, $v_{-\infty}$ must be twice the minimum given in (38).

In the approximation of eq. (37), the shear in the jet profile between its axis and radius r is

$$\frac{\Delta z(r)}{r} \approx -3\alpha \left[\frac{r}{1 \text{ cm}}\right] \left[\frac{B_0}{20 \text{ T}}\right]^2 \left[\frac{10 \text{ m/s}}{v_{-\infty}}\right]. \tag{39}$$

For, say, $r = 1$ cm, $v_{-\infty} = 10$ m/s, $\alpha = 2$ and $B_0 = 20$ T, we would have $\Delta z(r) \approx 6r$, which is a fairly severe distortion of the jet.

Returning to the issue of the radial pinch, we can now cast eq. (23) in the form

$$\Delta P_{r,\max} \approx 50 \text{ atm} \left[\frac{r}{1 \text{ cm}}\right] \left[\frac{r}{D}\right] \left[\frac{B_0}{20 \text{ T}}\right]^2 \left[\frac{v_{-\infty}}{10 \text{ m/s}}\right]. \tag{40}$$

For, say, $r = 1$ cm, $v_{-\infty} = 10$ m/s, $D = 20$ cm and $B_0 = 20$ T, the maximum radial pressure is 2.5 atmospheres. This may be enough to perturb the shape of the jet as it enters the magnet.

When the jet leaves the magnet, the radial pressure goes negative. This pressure is small compared to the tensile strength of the jet material, so the jet will not necessarily tear apart. However, the rapid change of pressure from positive to negative may excite oscillations of the jet which lead to breakup into macroscopic droplets. This would occur after the proton beam interacted with the jet, so is more of a nuisance for the liquid-collection system than a fundamental flaw.

The longitudinal effects, (38) and (39), are suppressed at higher jet velocities, which, however, enhance the radial pinch (40).

2.5.2 Magnetic Damping of Radial Perturbations

If the liquid jet deforms, either due to the Lorentz forces on the eddy currents or due to the beam-induced pressure wave that was discussed in sec. 2.1.2, further eddy currents will arise, leading to further Lorentz forces that damp the deformation.

To estimate this, we follow the argument of sec. 2.5.1 for a conducting ring of radius r perpendicular to a magnetic field B_0. Suppose the ring is being deformed with a radial velocity v_r, either inwards or outwards. Then the rate of change of magnetic flux through the ring is $\dot{\Phi} = 2\pi r v_r B_0$, and the eddy current induced in a ring of cross section $\Delta r \Delta z$ is $I = \sigma \Delta r \Delta z v_r B_0$, where σ is the conductivity. The Lorentz force on this current leads to a radial pressure gradient of magnitude

$$\frac{\Delta P_r}{\Delta r} = \frac{\Delta F_r}{\Delta r \Delta z \Delta l} = \frac{B_0 I \Delta l}{\Delta r \Delta z \Delta l} = \sigma v_r B_0^2. \tag{41}$$

The total damping pressure at radius r is therefore

$$\Delta P_{r,\text{damp}} \approx \sigma r v_r B_0^2. \tag{42}$$

As a first example, consider inward radial motion caused by the pinch pressure (23). In the first approximation, the jet surface accelerates inwards during the characteristic time

D/v_z under a force approximated by the pinch pressure $\Delta P_{r,\max}$ times the surface area. Then eq. (23) leads to the estimate for the radial velocity:

$$v_r \approx -\frac{\sigma}{4}\frac{r}{\rho}B_0^2. \tag{43}$$

Combining this with eq. (42), the damping pressure is

$$\Delta P_{r,\mathrm{damp}} \approx \frac{\sigma^2 r^2 B_0^4}{4\rho}. \tag{44}$$

For a liquid-metal jet of conductivity 10^6 MKSA, radius 1 cm, and inside a 20-T field, the damping pressure is about 4,000 atm. This greatly exceeds the pinch pressure of 2.5 atm estimated above, and suggests that the radial motion due to the pinch is highly damped.

As a second example, consider the same jet that is now being blown apart with a radial velocity $v_r = 1,000$ m/s by the beam-induced shock. Then the damping pressure (42) is 4 GPa, which equals the tensile strength of steel, and so might hold the jet together.

The damping pressure in the second example is about 20 times the magnetic pressure, $B_0^2/2\mu_0$.

Thus, it is encouraging that significant damping of all radial perturbations will occur in a strong magnetic field.

2.5.3 Jet at an Angle to the Axis of a Solenoid

To improve the yield of pions in the interaction of the proton beam with the liquid jet, it is desirable that the jet axis make a small angle $\theta \approx 0.1$ to the axis of the solenoid. In this case the motion of the jet includes a component perpendicular to the magnetic field.

The induced eddy currents will flow in loops that are roughly perpendicular to the magnetic field lines. As a simplification, we suppose that the current loops are circles perpendicular to the axis of the solenoid. This approximation should be reasonable for small θ.

The (unperturbed) trajectory of the conductor of radius a is taken to be along the line

$$x = z\theta, \tag{45}$$

where z increases with increasing time. To simplify the calculations, we suppose the trajectory follows eq. (45), even though the velocity of the jet is perturbed by the magnetic field (impulse approximation).

Following the same line of argument as in sec. 2.5.1 we again calculate the drag force induced on the conducting disc. The force element on a piece of the disk at radius $r = \epsilon a$ and azimuth ϕ is found to be [28]

$$\begin{aligned} d\mathbf{F} &= Id\mathbf{l}\times\mathbf{B} \qquad (46)\\ &= I\epsilon a d\phi\left[(\hat{\mathbf{x}}\cos\phi+\hat{\mathbf{y}}\sin\phi)\left(B_z-\frac{(z\theta)^2+(\epsilon a)^2+2\epsilon a z\theta\cos\phi}{4}B_z''\right)+\hat{\mathbf{z}}\frac{B_z'}{2}(\epsilon a+z\theta\cos\phi)\right], \end{aligned}$$

where $\hat{\rho}$ is the unit vector pointing radially outwards from the axis of the jet ($\rho = \epsilon a$).

The transverse force can be decomposed into a radial pinch (or expansion) as discussed in sec. 2.5.1 plus a drag in the x direction. The longitudinal (z) force vanishes on the axis of the jet, has a drag that is independent of azimuth, and another component that varies with azimuth, causing a torque (or shear).

Drag Forces. We first ignore the radial pinch and the shear by integrating eq. (46) over ϕ and using eq. (20) for I to obtain

$$d\mathbf{F} = \frac{\pi\sigma a^4 v_z B_z' \epsilon^3 \Delta\epsilon \Delta z}{2}\left(\hat{\mathbf{x}}\frac{z\theta B_z''}{2} - \hat{\mathbf{z}}B_z'\right). \tag{47}$$

The z component of the drag force is the same as found previously in eq. (25). The retarding force vanishes on the jet axis, and increases as the cube of the radius within the jet. As a result, the core of the jet will move ahead of the outer regions.

In turn, we integrate (47) over ϵ to obtain the total force on a disc of thickness Δz:

$$\mathbf{F} = \frac{\pi\sigma a^4 v_z B_z' \Delta z}{8}\left(\hat{\mathbf{x}}\frac{z\theta B_z''}{2} - \hat{\mathbf{z}}B_z'\right). \tag{48}$$

In the equation of motion, we again replace differentiation by time with that by z:

$$\mathbf{F} = m\dot{\mathbf{v}} = \pi a^2 \Delta z \rho v_z \mathbf{v}'. \tag{49}$$

The components of the equation of motion of the conducting jet are thus,

$$v_x' = \frac{\sigma a^2 z\theta B_z' B_z''}{16\rho}, \qquad \text{and} \qquad v_z' = -\frac{\sigma a^2 (B_z')^2}{8\rho}. \tag{50}$$

We use the example of a semi-infinite solenoid to illustrate the effect of the eddy currents on the jet velocity, because the needed field derivatives have simple analytic forms. The form of the trajectory, (45), assumes that the center of the magnet is at the origin. Suppose the length of the physical magnet is α times its diameter D, so that the coil extends over $-\alpha D/2 \le z \le \alpha D/2$. Then the field of the physical magnet can be represented by the field of a semi-infinite solenoid beginning at $z = -\alpha D/2$.

From the derivatives of eq. (31) we see that v_z' is always negative, but that v_x' is negative only until the jet enters the magnet ($z = -\alpha D/2$). Integrating (50) from $-\infty$ to z, we find that the velocity components of the jet are

$$v_x = v_{x,-\infty} - \frac{3\sigma a^2 B_0^2 \theta}{1024\rho D}\left[\frac{\pi}{2} + \tan^{-1} w + \frac{w}{1+w^2} + \frac{2w}{3(1+w^2)^2} - \frac{16z}{3D(1+w^2)^3}\right], \tag{51}$$

and

$$v_z = v_{z,-\infty} - \frac{3\sigma a^2 B_0^2}{128\rho D}\left[\frac{\pi}{2} + \tan^{-1} w + \frac{w}{1+w^2} + \frac{2w}{3(1+w^2)^2}\right], \tag{52}$$

where $w = 2z/D + \alpha$. Of course, $v_{x,-\infty} = \theta v_{z,-\infty}$ by assumption. The velocity components of the jet when it reaches the center of the magnet ($z = 0,\ w = \alpha$) are

$$v_{x,0} = \theta v_{z,-\infty} - \frac{3\sigma a^2 B_0^2 \theta}{1024\rho D}\left[\frac{\pi}{2} + \tan^{-1}\alpha + \frac{\alpha}{1+\alpha^2} + \frac{2\alpha}{3(1+\alpha^2)^2}\right], \tag{53}$$

and

$$v_{z,0} = v_{z,-\infty} - \frac{3\sigma a^2 B_0^2}{128\rho D}\left[\frac{\pi}{2} + \tan^{-1}\alpha + \frac{\alpha}{1+\alpha^2} + \frac{2\alpha}{3(1+\alpha^2)^2}\right], \tag{54}$$

Thus, while both v_x and v_z are reduced on entering the solenoid, the relative reduction in the x velocity is only 1/8 that of the z velocity. As a consequence, the angle θ of the trajectory to the axis of the solenoid actually increases as the jet enters the magnet. For example, suppose that $v_{z,-\infty}$ is 3 times the loss of velocity on entering the magnet. Then

$$v_{z,0} = \frac{2}{3} v_{z,-\infty}, \qquad v_{x,0} = \frac{23}{24} \theta v_{z,-\infty}, \tag{55}$$

and the angle of the trajectory at the center of the magnet is

$$\theta_0 = \frac{v_{x,0}}{v_{z,0}} = \frac{69}{48}\theta = 1.44\theta. \tag{56}$$

Figure 15 illustrates the variation of v_x, v_z and θ of the jet as a function of z.

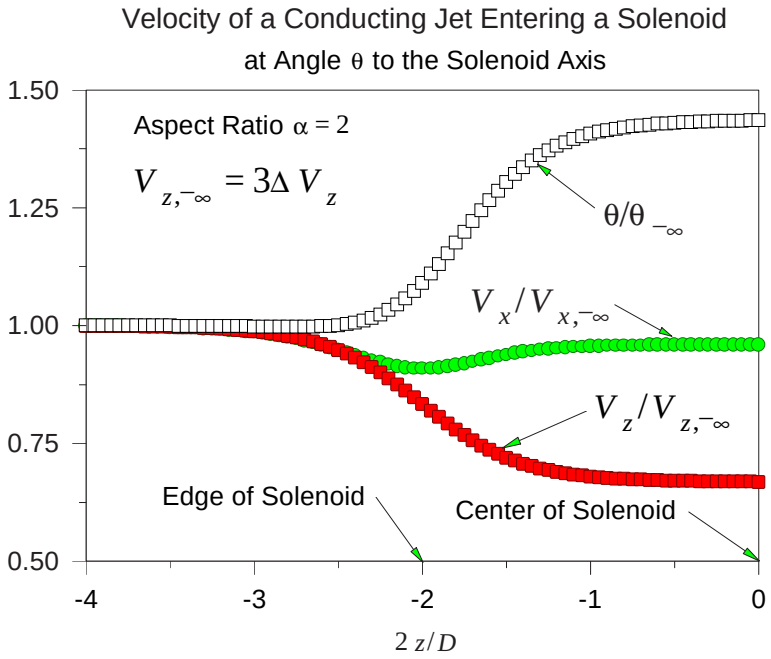

Figure 15: v_x, v_z and θ of the jet as a function of z as it enters a solenoid of aspect ratio $\alpha = 2$, according to eqs. (51-52). The initial z velocity of the jet is taken to be 3 times the loss of velocity on entering the solenoid.

We are greatly encouraged by these idealized calculations that the effect of eddy currents on the transverse velocity of the jet will not be too severe.

The above analysis is for the drag force on the jet as a whole. Recall that the force varies with radius within the jet, and so leads to longitudinal distortions as discussed in sec. 2.5.1. The variation of the drag force in x leads to additional torques and shears, which we now discuss.

Torque and Shear. The magnetic forces on the eddy currents also produce a torque that will twist the jet about the axis perpendicular to the plane of the jet motion, the y axis in our example.

The torque $d\mathbf{N}$ on a small element of a current ring about its center can be calculated from eq. (46). On integrating over ϕ and ϵ we find that $N_x = 0$, and the total torque on a disc of radius a and thickness Δz is

$$N_y = \frac{\pi}{16} z\theta\sigma a^4 v_z B_z'^2 \Delta z \approx -\frac{xF_z}{2}. \tag{57}$$

The sense of rotation is opposite to that of the deflection of the jet trajectory as it enters the magnetic field.

The moment of inertia of the disc about a diameter is $ma^2/4 = \pi\rho a^4\Delta z/4$. Hence the angular acceleration of the azimuthal angle φ of the disc about the y axis is

$$\ddot{\varphi} = v_z \frac{d\dot{\varphi}}{dz} = \frac{\theta\sigma z B_z'^2 v_z}{4\rho}. \tag{58}$$

Note that this is independent of the radius of the jet. Using B_z' from eq. (31), we have

$$\frac{d\dot{\varphi}}{dz} = \frac{\theta\sigma B_0^2}{4\rho D^2} \frac{z}{(1+w^2)^3}, \tag{59}$$

where, as before, $w = 2z/D + \alpha$, and $\alpha = L/D$. This can be integrated once to give

$$\dot{\varphi} = v_z \frac{d\varphi}{dz} = -\frac{3\theta\sigma B_0^2}{128\rho} \left[\frac{\alpha\pi}{2} + \alpha \tan^{-1} w + \frac{\alpha w}{1+w^2} + \frac{2(1+\alpha w)}{3(1+w^2)^2} \right]. \tag{60}$$

If we ignore the variation in v_z with position, this can be integrated once more to yield

$$\varphi(z) = -\frac{3\theta\sigma B_0^2 D}{256\rho v_z} \left[\left(\alpha w + \frac{1}{3} \right) \left(\frac{\pi}{2} + \tan^{-1} w \right) + \frac{\alpha - w}{3(1+w^2)} \right]. \tag{61}$$

At the center of the magnet, $w = \alpha$, the total angle of rotation of the disc is

$$\varphi_{\text{center}} = -\frac{3\theta\sigma B_0^2 D}{256\rho v_z} \left[\left(\alpha^2 + \frac{1}{3} \right) \left(\frac{\pi}{2} + \tan^{-1} \alpha \right) \right] \approx -\frac{3\pi\alpha^2\theta\sigma B_0^2 D}{256\rho v_z}, \tag{62}$$

where the approximation holds for α somewhat larger than 1. For example, if $\alpha = L/D = 2$, $D = 0.2$ m, $B_0 = 20$ T and $v_z = 10$ m/s, we find $\varphi_{\text{center}} \approx -4\pi\theta$. With $\theta = 0.1$ rad, then $\varphi_{\text{center}} \approx -0.4\pi$.

Equation (60) indicates the interesting result that the rate of change of rotation is independent of the velocity, so the total rotation can be suppressed by increasing the jet velocity, thereby lowering the transit time.

A liquid jet would presumably not rotate as a rigid body. Rather, there would be a shear in which v_z of that portion of the jet closer to the magnet axis actually increases, while v_z decreases for material farther away (and by a larger absolute amount). Our estimate that $\varphi_{\text{center}} \approx 90^\circ$ can perhaps be reinterpreted as indicating that the shear distance along the jet axis will amount to roughly the jet radius when the jet reaches the center of the magnet. This would not be troublesome.

2.5.4 The Rayleigh Instability of the Jet

Zero Magnetic Field. Following earlier work by Plateau, Rayleigh deduced that a cylindrical jet is unstable against perturbations of wavelength (along the jet axis) greater than the circumference of the jet [96]. The result of the instability is the breakup of the jet into droplets, commonly seen as water exits a nozzle. The characteristic time for onset of the instability is

$$\tau = 3\sqrt{\frac{r^3\rho}{T}}, \tag{63}$$

where the jet has radius r, mass density ρ and surface tension T. The distance travelled by a jet before breakup is then $v\tau$, where v is the jet velocity.

An example of breakup of a 0.5-mm-diameter mercury jet is shown in Fig. 16 [66, 67, 68]. The density of mercury is $\rho = 13.5$ g/cm^3, and the surface tension is $T = 470$ dyne/cm. Then eq. (63) gives $\tau = 0.002$ s for $r = 0.025$ cm. At 40 psi, the jet velocity was $v = 5$ m/s, so the characteristic length before breakup is predicted to be 1 cm, in good agreement with the reported value of 1.4 cm. It thus appears that Rayleigh's formula is valid for liquid-metal jets.

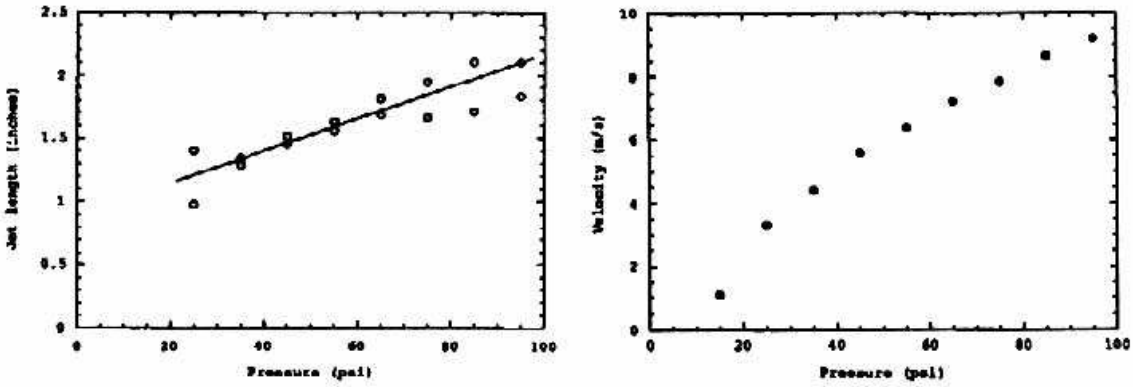

Figure 16: Length before breakup, and velocity of a mercury jet of radius 0.025 cm.

Turning to parameters relevant to the muon-collider target, consider a gallium jet of radius 1 cm. The density is $\rho = 6$ g/cm^2, and the surface tension is $T = 360$ dyne/cm. Then the instability time is $\tau = 0.4$ s. For a jet velocity of 10 m/s, the breakup length would be about 4 m, which is satisfactory. If the jet radius is reduced to 0.5 cm, the breakup length drops to 1.4 m.

Nonzero Axial Magnetic Field. The effect of a uniform axial magnetic field on the Rayleigh instability has been considered by Chandrasekhar [97]. There is no change in the instability time for a nonconducting liquid, unless its permeability is significantly greater than one. For a conducting liquid, Chandrasekhar introduces a quality factor,

$$Q = \frac{\mu B^2}{4\pi\eta}\sqrt{\frac{r^3}{\rho T}}, \tag{64}$$

where μ is the permeability, B is the axial magnetic field strength, and η is called the "resistivity" ($\eta = c^2/4\pi\sigma$, where σ is the electrical conductivity). For $Q > 20$, the Rayleigh instability is suppressed in the first approximation.

For mercury, $\eta = 7.5 \times 10^3$ cm^2/s, and $Q = 1.33 \times 10^{-7} B^2 r^{3/2}$ in Gaussian units. Thus for a 20-T axial magnetic field and $r = 1$ cm, $Q \approx 5000$, and the Rayleigh instability should be almost completely damped. This conclusion is little changed by variations in the radius or resistivity by factors of 2, and should be valid for all liquid-metal jets under consideration here.

The quality factor does not drop to 20 until the field has fallen to slightly over 1 T (for $r = 1$ cm). Hence, unless the jet travels more than a meter in a region where the magnetic field is less than 1 T, the Rayleigh instability will be of little concern for us.

2.6 The Operation of an RF Cavity near a Target

Once the pions have been collected at the target, it is necessary to shape the collected pion/muon beam into a longitudinal phase space suitable for eventual acceleration in the following cooling section. The goal is to capture and maintain the longitudinal phase space such that the energy spread dE/E is reduced to near 10%, and the pulse is contained within a pulse length of $c\tau < 6$ m. Since we are interested in capturing low-energy pions (kinetic energy 50-400 MeV), these pions will have a large initial velocity spread (β between 0.7 and 0.98). It is therefore important to begin compressing the energy spread in the phase-rotation section as soon a practical, with an accelerating gradient as high as possible.

The wavelengths of the rf cavities are constrained by the requirement that $\lambda_{\rm rf}/2$ be greater than the bunch length of the collected pions/muons. This bunch length in turn is determined by the initial bunch length of the proton beam impinging on the target and the drift distance to the initial rf cavity. For an initial proton bunch length τ_{rms} of 1 ns and a drift distance of 3 m this total bunch length will be 4 ns (1.2 m). This constrains the wavelength of the initial rf cavity to be greater than ≈ 2.4 m (frequency < 125 MHz. As the bunch moves down the phase-rotation channel, it will continue to elongate, and therefore the rf wavelength of subsequent rf cells will need to increase, and a complete phase-rotation scenario will require many rf cells of different frequencies.

A further constraint is placed on the frequencies of the rf cells if we add the requirement that the same phase-rotation channel must be capable of handling both positive and negative bunches in separate beam spills. This constraint can be satisfied simply by requiring the set of cavities to be odd multiples of a fundamental harmonic, 10, 30, 50, 70, 90, 110 MHz, *etc.* In such a scenario, the beginning rf frequency could be 110 MHz, descending to a final rf frequency of 10 MHz. Parameters for a possible complete scenario are given in the Table 5.

For the $\mu^+\mu^-$ collection system to be viable, the rf cells must perform satisfactorily at high gradients in a magnetic field, and in the high-radiation environment immediately following the target. Since experience operating an rf cell in a high-radiation environment generated by a beam of 10^{14} protons/pulse is limited [98, 99, 100, 102, 101, 103, 104, 105, 106], we propose to establish a proof-of-principle demonstration of this issue by constructing and operating at high gradients an rf cavity with a frequency suitable for a muon-collider collection system. Preparation for the study will include a MARS simulation of the flux of charged particles onto the rf cavity that emerges from the target and surrounding material.

Table 5: Low-Energy Collection-Linac Parameters.

rf Frequency (MHz)	90	50	30
Cavity Length (cm)	120	120	120
Full Gap Length (cm)	36	36	36
Cavity Radius (cm)	90	106	126
Beam Pipe Aperture (cm)	30	30	30
$Q/1000$ (from SFISH)	53.4	71.1	16.8
Av. Gradient (MV/m)	4.2	4.0	2.1
RF Peak Power (MW)	1.8	1.2	4.8
Av. Power @ 15 Hz (kW)	2.4	7.8	12.6
Stored Energy (J)	166	260	418
Linac Segment (m)	6	18	18
Total Power @ 15Hz (kW)	12	118	190

We sketch our limited understanding of the problem. Because the first rf cavity is located near the target, of order one high-energy particle passes through the cavity wall per beam proton. Secondary emission of electrons by high-energy particles occurs with probability of order 1% [102]. These secondary electrons gain various amounts of energy before hitting the cavity wall. This could produce undesirable heating of the cavity, and it could also initiate resonant secondary emission (multipactoring) that results in cavity breakdown [106]. It is believed that secondary emission of ions is of less significance [98].

For a pulse of 10^{14} protons on target, there will be of order 10^{12} secondary-emission electrons liberated in the first rf cavity. If these gained of order 1 MeV before hitting the cavity wall, the resulting energy deposition is about 0.1 J. In general, this energy deposition will be spread over a large surface area, and therefore appears to be of minor concern.

When the 10^{12} secondary electrons hit the cavity wall, they lead to tertiary electrons, *etc.* If these electrons have energy such that the secondary-emission coefficient exceeds unity, an instability occurs. For metals typically used in cavity walls, the secondary-emission coefficient exceeds unity only for electron energies of order 1 keV [100, 105]. Hence, the troublesome electrons are those that acquire only of order 10^{-3} of the nominal energy gain of the cavity. Multipactoring discharges are more often observed at low-power operation of cavities, and are suppressed at higher power where secondary electrons gain higher energy.

However, since we begin with 10^{12} secondary electrons, it is hard to predict whether a tiny fraction of them might lead to cavity breakdown. Experiments must be performed in realistic configurations to study this critical issue.

3 The R&D Program

The proposed R&D program into targetry issues for a muon collider consists of eight parts:

1. Initial studies of liquid (and solid) target materials with a proton beam at the AGS.
2. Studies of a liquid-metal jet entering a 20-T magnet at the National High Magnetic Field Laboratory (NHMFL) in Florida.
3. Studies of a full-scale liquid-metal jet in a beam of 10^{14} protons per pulse, but without magnetic field.
4. Studies of a liquid-metal jet + proton beam + 20-T pulsed solenoid magnet.
5. Studies of a 70-MHz rf cavity downstream of the target in the proton beam, but without a magnet around the cavity.
6. Continuation of topic 5 with the addition of a 1.25-T, 1.25-m-radius solenoid surrounding the rf cavity.
7. Characterization of the pion yield downstream of the target + rf cavity.
8. Simulation of the performance of liquid-metal targets: thermal shock, eddy currents. Validation of the simulation by exploding-wire studies.

The key requirements on the AGS for this program have been presented in the Executive Summary.

3.1 Initial Studies of Targets in a Proton Beam

The first set of studies concerns the viability of various target options with respect to their interaction with the proton beam. The key issues are the effects of thermal shock (sec. 2.1.2), and (for solid targets) the effects of radiation damage. We propose to study thermal shock in four target geometries:

1. **A free liquid-metal jet.** The jet may be dispersed by the beam, possibly violently. The 20-T magnetic field should damp the dispersal, but also distorts the jet on entry into the field.
2. **Liquid-metal in a pipe.** There is a high probability of damage to the pipe by the beam-induced thermal-shock.
3. **A cylindrical solid target.** The cylindrical geometry may enhance beam-induced thermal-shock damage along the axis of the target.
4. **A rectangular solid target.** For the energy deposition required at a muon collider source, thermal-shock damage is not expected. If confirmed, the primary concern will then be the long-term effect of radiation damage on the mechanical integrity of a moving band target.

Details of the test targets will be presented after a discussion of the beam.

3.1.1 The Proton Testbeam

The testbeam should approach as closely as possible the parameters of the primary proton beam for a muon collider. The key parameters are 16-24 GeV energy, 10^{14} protons per pulse, rms radius of 4 mm and pulse length of 2 ns.

The candidate proton testbeam is the FEB U-line at the AGS [108, 109], shown in Fig. 17. The location of the U-line in the AGS-RHIC complex can be seen in Fig. 51. This beam typically is operated at 24 GeV, extracting a single bunch per AGS cycle with up to 10^{13} protons in that bunch. The beam emittance is about 100π mm-mrad, and the pulse length typically is $\sigma_t = 32$ ns. The pulse rate can be as high as 0.8 Hz.

The AGS beam parameters are well matched to the needs of the proposed studies, and with some upgrades the AGS would be an excellent muon-collider source [1, 110]; see also Appendix B.

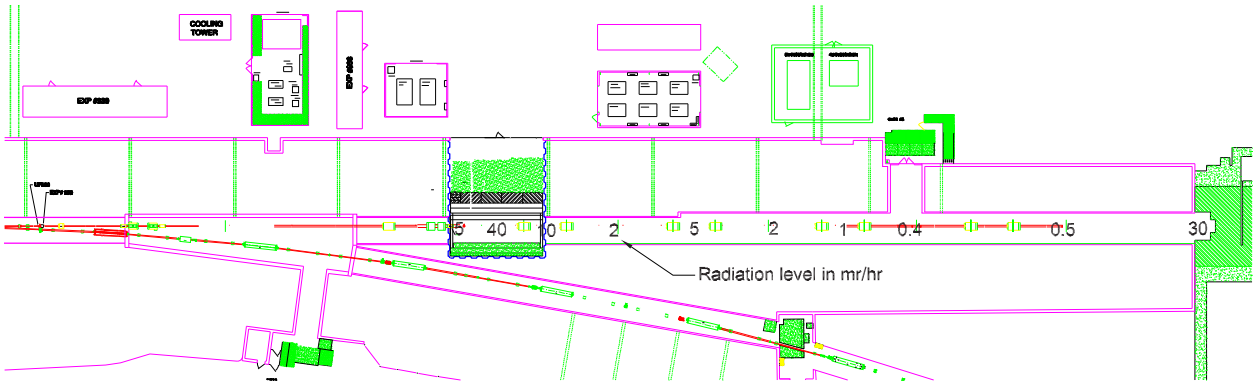

Figure 17: Plan view of FEB U-line at the BNL AGS. The residual radiation levels at various point along the tunnel are indicated.

All of the beam tests presented in this proposal can be performed during parasitic use of the beam at a pulse rate of less than one every two minutes. The initial studies (secs. 3.1 and 3.3) are in effect a series of single-pulse experiments, while later studies (secs. 3.4-7) will be limited by the repetition rate of the pulsed 20-T magnet.

The time scale for thermal shock is set by the target radius divided by the speed of sound, say (1 cm)/(3,000 m/s) = 3 μs. Any pulse length less than about 1 μs will cause the same thermal shock in the targets of concern. Thus the AGS-bunch length of 32 ns (rms) is adequate for the thermal-shock studies. For the rf cavity (secs. 3.5-6) a shorter pulse is desired. A recent study [107] indicates that the bunch length in the AGS can be reduced to $\sigma_t = 2$ ns if the beam is operated near 7 GeV. That condition should be adequate for the rf-cavity studies.

The remaining beam issue is whether a proton bunch in the FEB U-line can cause thermal shock at the level to be encountered at a muon-collider source. According to the model presented in sec. 2.1.2, the pressure in the target material resulting from the thermal shock is proportional to the peak density of energy deposited (J/g), rather than, say, the total energy deposited. Hence, by variable focusing of the beam, a scan can be made through the range of thermal shock relevant to a muon-collider source.

In particular, the muon collider design [1] presently calls for a pulse of 10^{14} protons in a spot size of 4-mm radius (rms). The model then indicates that a pulse of N protons would cause a similar thermal shock if its radius were $4\sqrt{N/10^{14}}$ mm. Anticipating that pulses of $N = 10^{13}$ will be available, we set a requirement that the U-line beam be focusable to a radius of 1 mm (rms).

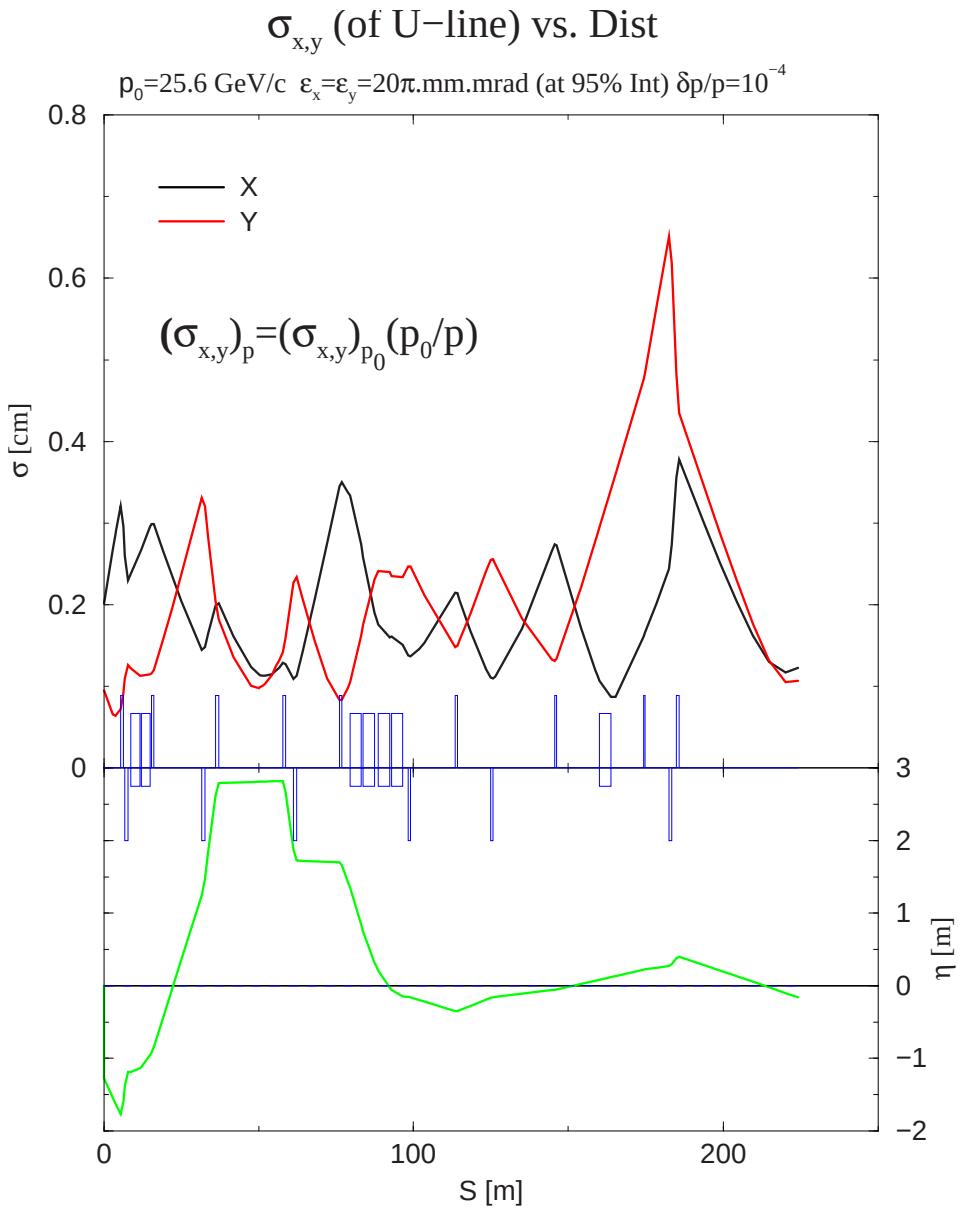

Figure 18: TRANSPORT calculation for the U-line with a focus at the neutrino blockhouse using presently connected quads. A transverse (95%) emittance of 20π mm-mrad was assumed.

A preliminary study [112] indicates that a U-line beam with (95%) emittance of 20π mm-mrad can be focused with existing quads to $\sigma_r = 1$ mm at the neutrino blockhouse. Figure 18

shows results of the TRANSPORT calculation. For the larger emittance of 100π mm-mrad that holds for bunches of 10^{13} protons, the spot size is expected to be about $\sqrt{5}$ times larger, namely 2.4 mm (rms).

Studies are underway to determine what configuration of magnets can produce the desired spot size of 1 mm (rms).

Of course, it is desirable that studies be made with a beam of 10^{14} protons per pulse to explore possible effects that scale with the total energy deposition in the target. This option will be pursued in sec. 3.3.

3.1.2 Experimental Configuration

We propose to pursue the initial targetry studies in the neutrino blockhouse of the FEB U-line (Fig. 19), despite the relatively high radiation level there (Fig. 17), to be able to share diagnostic facilities with the AGS Spallation Target Experiment (ASTE), E-938, which is studying related issues in a mercury target.

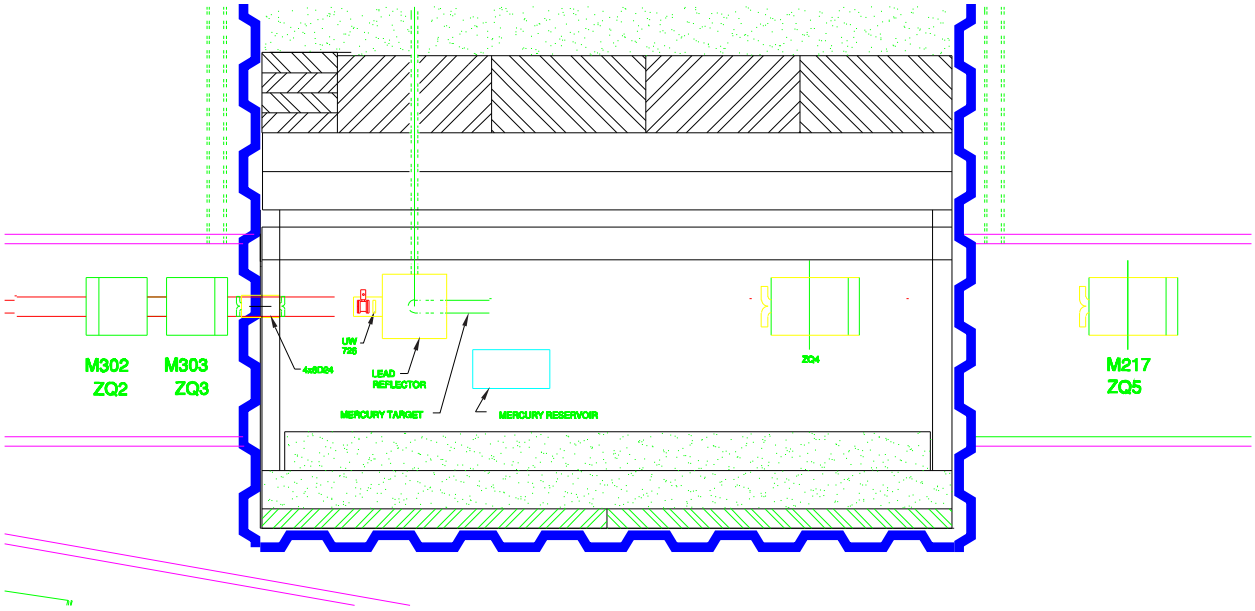

Figure 19: The neutrino blockhouse of the FEB U-line, where tests of a mercury target for neutron spallation have been performed recently.

The initial targetry studies are quite straightforward. Each of a set of candidate targets will be exposed to a series of beam pulses with ever smaller radius over the range of 5 mm (rms) down to 1 mm (and even smaller if possible). Since our initial goal is understanding of possible damage of the targets by a single beam pulse, each pulse is analyzed separately. The primary diagnostics are visual, and the secondary diagnostic is a measurement of the time-dependent mechanical strain induced in various parts of the target (discussed in sec. 3.1.3). From these, we should learn whether there are important damage thresholds near the nominal targetry parameters of a muon-collider source.

The beam will be operated at a very low repetition rate, so the targets are not cooled, other than by radiation (and conduction through the supports). The solid targets are mounted on simple supports, while the liquid targets reside in a containment vessel with walls of 1/4″-thick aluminum. The beam passes through the walls of the containment vessel. If desired, beam ports of a different material could be added.

The targets are located on a stand that can be positioned remotely in (and completely removed from) the beam.

The layout for three initial tests of liquid targets is shown in Fig. 20. As discussed in sec. 2.3.3, we plan to use eutectic Ga/Sn as the initial liquid metal. It is a liquid at room temperature. As shown from right to left, these tests involved targets in the following forms:

1. A liquid metal in an open stainless-steel trough of 1-cm diameter. The liquid may be blown out of the trough by the beam. The trough is contained in a stainless-steel box with a 1/4″-inch-thick lucite window on one face to permit a camera to view the event. We have verified that the Ga/Sn alloy does not wet lucite or stainless steel (at room temperature).

2. A liquid metal in a 1/2″-diameter stainless steel pipe bent in a U-shape. If the liquid is ejected from the tube by the beam, the dispersed liquid will be seen through the lucite window of the stainless-steel chamber above the pipe. It is also very possible that the pipe will be cracked by the beam, in which case the liquid would leak into a lower stainless-steel chamber that surrounds the pipe.

3. A vertical liquid jet of 1-cm diameter. The jet is part of a small closed-loop system with a mechanical pump, all of which is inside the aluminum containment vessel. The vertical jet is created in a 2″-diameter lucite housing. The beam passes through the walls of this housing.

The aluminum containment vessel also houses a video-rate (30 frames/s) CCD camera and (strobe) light for optical viewing of the target tests. The images from the CCD camera will be captured by a PC-based frame grabber.

We also are considering use of a higher-speed camera. If the target liquid were dispersed with a velocity of 10 m/s, a rate of 1000 frames/s would barely resolve the history of the dispersal over a 1-2 cm path as available in the various target housings. However, we would not install this (expensive) instrumentation inside the aluminum containment vessel until we have direct experience that the dispersal of the liquid is not too violent.

The solid-target tests will involve two configurations, cylinder and slab, of at least two alloys: pure nickel [77] and a copper-nickel alloy [32]. We expect no single-pulse damage to metal slab targets, but possible damage along the axis of cylindrical targets due to the reflected, converging pressure wave (sec. 2.1.2).

After completion of the initial set of tests described above, we will then study a a liquid-metal jet that propagates against the beam.

3.1.3 Liquid-Metal Jet Collinear with the Beam

As the next step towards a realistic liquid-metal target for a muon-collider source, we will study a 3-mm-diameter liquid-metal jet that collides head-on with the beam.

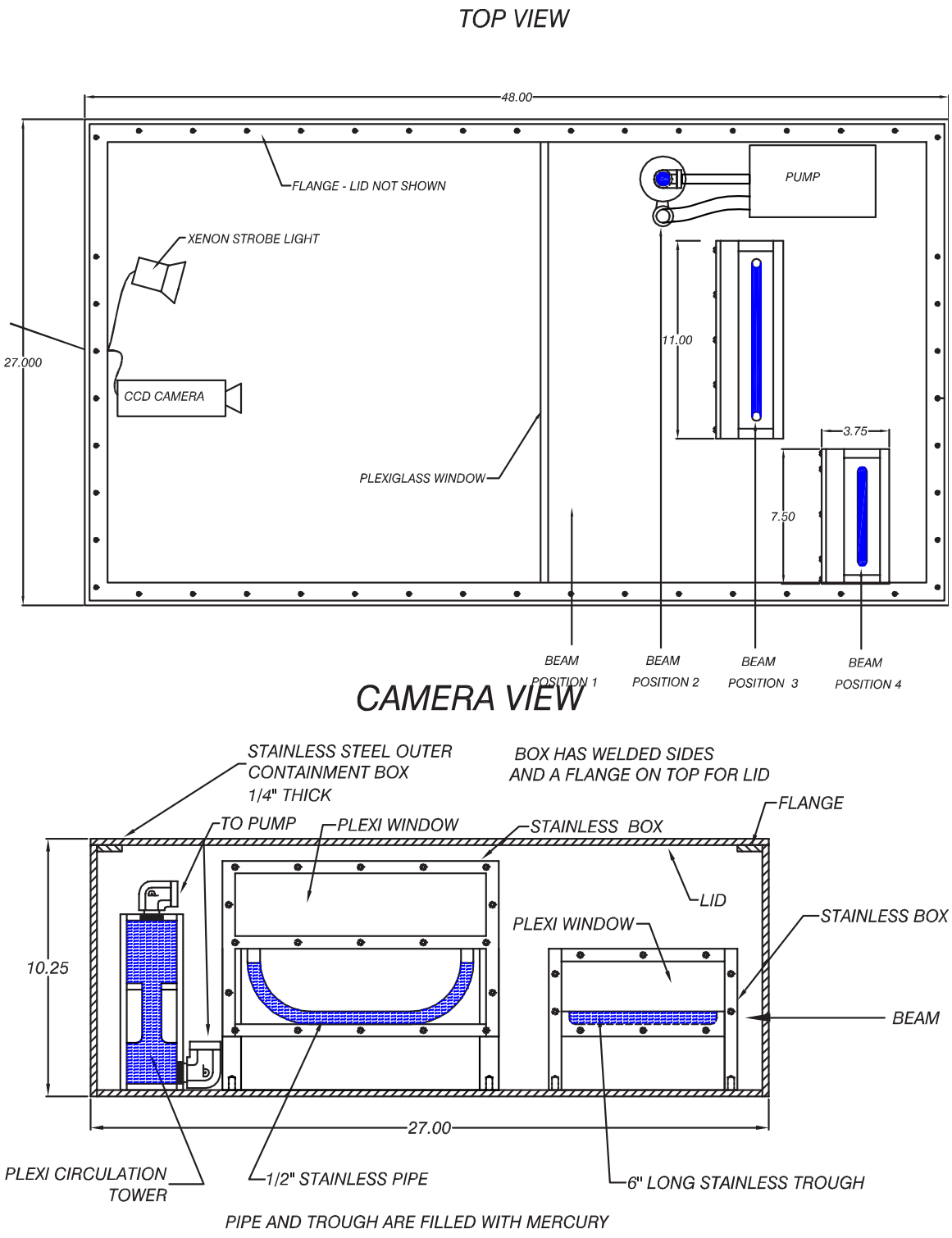

Figure 20: Top and beam views of the setup to test simple liquid targets.

The diameter of 3 mm is set by the availability of a commercial solenoid valve (Skinner 71215SN2MF00) with opening/closing times of 8 ms against a pressure of 30 atm. A block

diagram of the jet is shown in Fig. 21, and is based on a mercury jet demonstrated at CERN [26].

The small diameter of this initial jet further emphasizes the need for a proton beam of rms radius 1 mm or less.

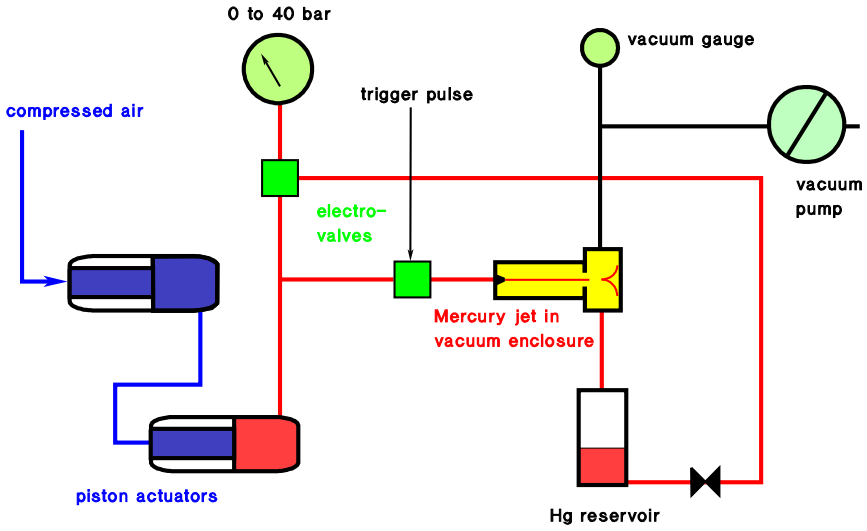

Figure 21: Block diagram of a mercury jet.

As mentioned before, in the initial tests we will use the nontoxic, room-temperature-liquid alloy of gallium and tin. This alloy has a viscosity close to that of water, so flows easily. A jet is readily produced, as shown in Fig. 22.

Figure 22: A room-temperature jet of liquid Ga/Sn created by a syringe.

The free liquid jet will be contained within a vessel similar to that shown in Fig. 20. Its interaction with the proton beam will be viewed by a camera, and the shock (if any) to the vessel will be diagnosed with the strain gauges described in the next section.

3.1.4 Measurement of Strain in the Test Targets

A quantitative measure of the effect of the beam-induced pressure wave on a target is the time-dependence of the mechanical strain in the target just after a beam pulse. AGS experiment E-938 is studying this issue for a 12-cm-diameter, 1-m-long mercury target, and has found that fiberoptic strain sensors have the greatest immunity to electromagnetic noise caused the the passage of the beam pulse [113]. We therefore propose to use this technology in the proposed studies. The E-938 collaboration has kindly agreed that we may share parts of the needed readout electronics.

The strain measurement is based on detection of stress-induced variations in the gap distance between two parts of a fiberoptic cable, shown in Figs. 23, 24 and 25. The ends of two fiber segments are separated by about 100 μm and free to move within a 1-cm-long glass tube. Relative motion between the two fibers results in a change in the interference pattern of light reflected off the two end faces. If the fibers are glued to the two ends of the glass tube, as shown in Fig. 24, and those ends are also glued to the material under stress, then the gap distance equals the strain over the 1-cm length of the glass tube.

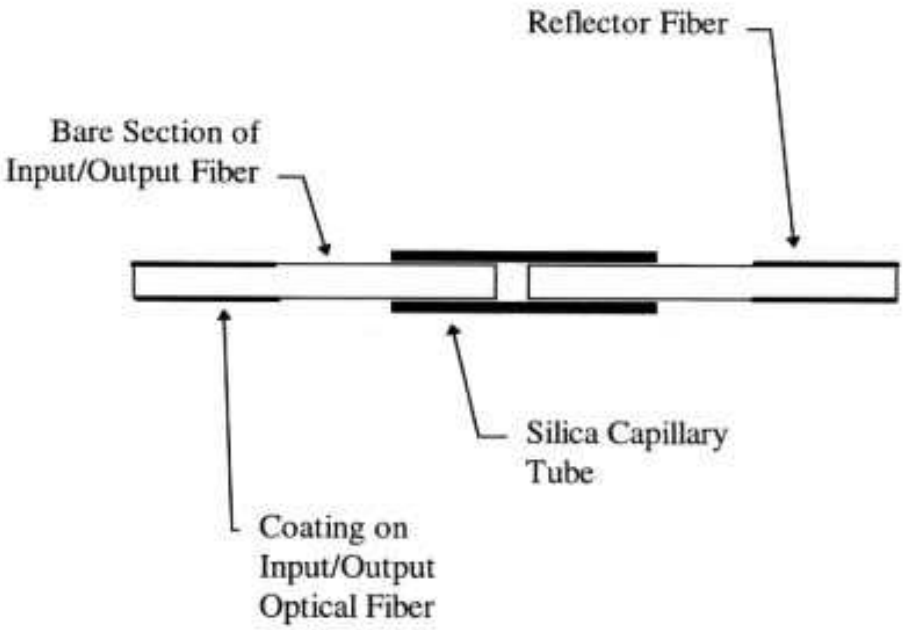

Figure 23: Components of a fiberoptic strain sensor.

The interferometric readout system [114] is capable of resolving gap variations of about 10-20 nm, corresponding to strains of 1-2 $\times$ 10^{-6} over the 1-cm-long glass tube, *i.e.*, 1-2 microstrain. From eq. (1) of sec. 2.1.2, we see that the strain expected in material directly

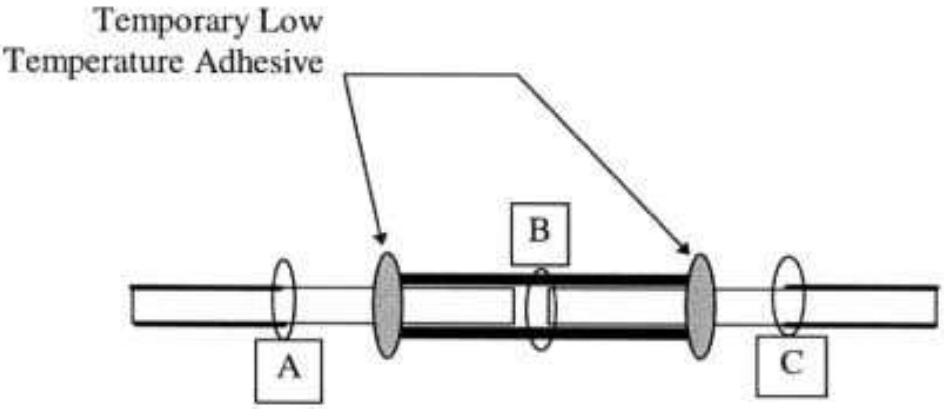

Figure 24: Two-point attachment of the strain sensor.

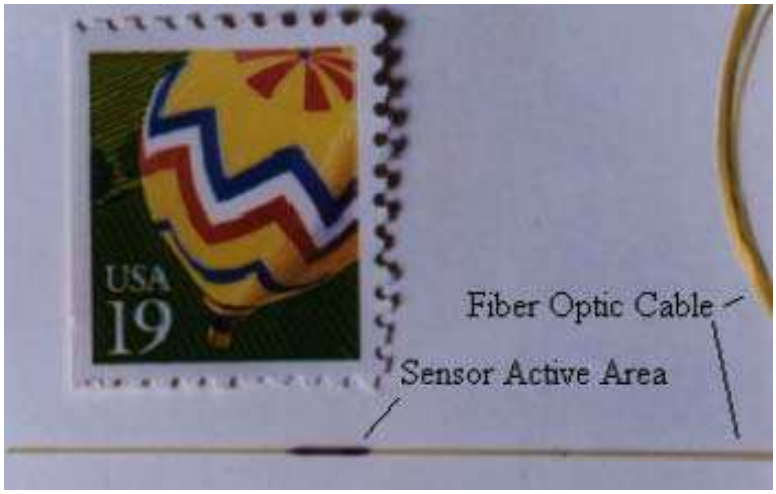

Figure 25: View of a fiberoptic strain sensor.

exposed to the beam is

$$\frac{\Delta l}{l} \approx \Delta U \frac{\alpha}{C}, \tag{65}$$

for an energy deposition density of ΔU in a material with thermal expansion coefficient α and heat capacity C. With typical values of $\Delta U = 30$ J/g, $\alpha = 2 \times 10^{-5}$ and $C = 0.3$ J/g-°C (Table 3), we expect a strain of 2×10^{-3}. Hence, the fiberoptic strain sensors have a resolution about 1/1000 of the peak stress, and so can yield useful information even when applied at positions where the stress is well below the peak amount.

Furthermore, the frequency response of the readout system exceeds 1 MHz, and so can resolve the detailed history of the initial pressure wave and subsequent reflections in targets of 1-cm transverse scale.

Figure 26 illustrates data collected with this sensor system in experiment E-938.

In our tests, the strain sensors will be applied directly to the solid targets and to the various housings of the liquid targets.

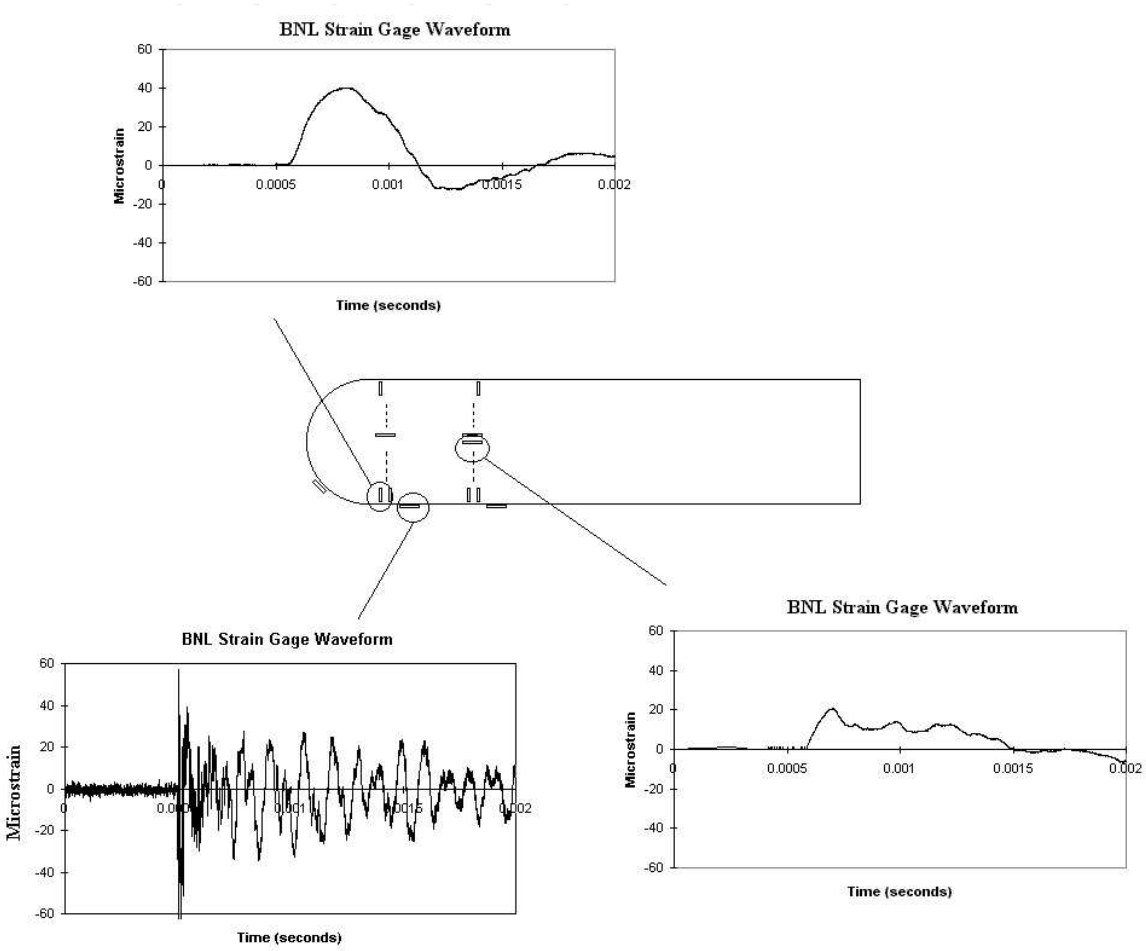

Figure 26: Arrangement of the fiberoptic strain sensors on the E-938 mercury target tank, and representative strain measurements from a beam pulse in the U-line.

3.2 Liquid-Metal Jet with a 20-T Magnet

A second key issue for a liquid-metal-jet target is whether it can move though a 20-T magnetic field without significant distortion. To test this, we propose to bring a simple liquid-metal jet to the National High Magnetic Field Laboratory (NHMFL) [115] and test it at Cell 4, a 20-T, 200-mm bore resistive magnet [116].

The Cell 4 magnet has a vertical bore, as shown in Fig. 27. It is available in 8-hour shifts, following approval of a proposal submitted to the NHMFL. We have visited the site (Tallahassee, FL) and found it well suited to our needs.

The baseline design for the muon-collider source (sec. 1.2.2) calls for a target of 1-cm radius, about 30 cm long, at an angle of about 150 mrad to the magnet axis. The magnetic field on the target is 20 T, and the inner diameter of the magnet coil is 24 cm. A horizontal liquid-jet target should have a velocity of at least 10 m/s to be little affected by gravity (sec. 2.4).

We plan to perform the initial magnet tests with the 3-mm-diameter Ga/Sn jet described

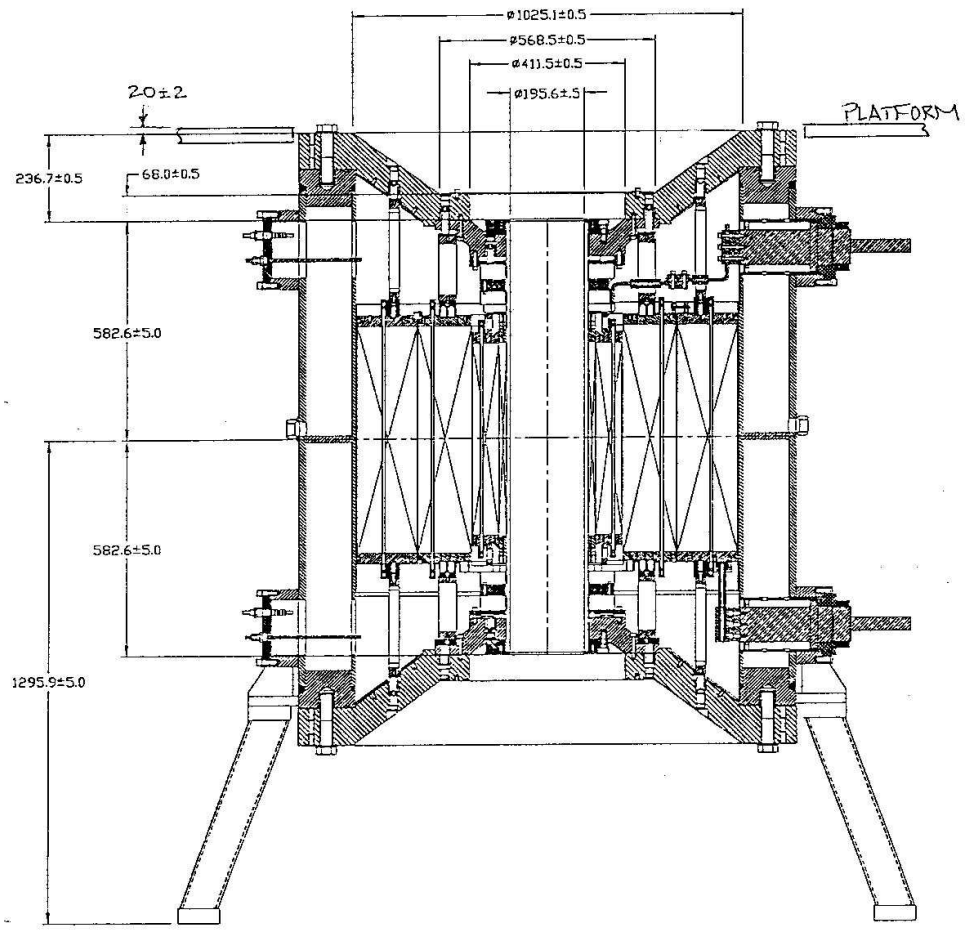

Figure 27: Vertical cross section through the 20-T, 190-mm bore resistive magnet at Cell 4 of the National High Magnetic Field Laboratory.

in sec. 3.1.3 rather than a jet of the nominal 2-cm diameter. Therefore, we will need to scale other parameters of the test to study the various eddy-current effects as the jet enters the magnet.

We recall the key results from sec. 2.5. The liquid metal has density ρ and conductivity σ. The jet has radius r and initial velocity v. The solenoid magnet has peak field B_0 and coil inner diameter is D. Then the radial pinch perturbs the jet radius by an amount that scales as

$$\frac{\Delta r}{r} \propto \frac{\sigma B_0^2 D}{\rho v}, \qquad \text{(radial pinch)}, \tag{66}$$

according to eq. (24). The jet loses axial velocity as it enters the magnet according to eq. (29). Since the change of axial velocity varies with radius, initially transverse planes in the jet shear into paraboloids. The maximum axial shear scales as

$$\frac{\Delta z}{r} \propto \frac{\sigma r B_0^2}{\rho v}, \qquad \text{(axial shear)}, \tag{67}$$

according to eq. (30). Finally, for a jet at angle θ to the axis of the magnet, there is an additional shear (which we call angle shear) between opposite sides of the jet which scales as

$$\frac{\Delta z}{r} \propto \frac{\sigma \theta B_0^2 D}{\rho v}, \qquad \text{(angle shear)}, \tag{68}$$

on multiplying eq. (62) for the rotation angle by the radius r. Note that the radial pinch (66) and the angle shear (68) have the same dependence on the dimensional parameters of the system, but the axial shear (67) has a different dependence. Hence, the latter effect must be studied separately from the other two.

We desire to observe the magnitudes of the dimensionless perturbations (66-68) in our studies of liquid jets entering a magnet.

We propose to use the eutectic Ga/Sn alloy for these tests, but have in mind possible eventual use of mercury or a lead alloy. Gallium has a conductivity about 3 times larger than the heavier metals, and is half as dense (see Table 3). Hence, the ratio σ/ρ is about 6 times larger for gallium. If we use a gallium jet of 3-mm diameter then $\sigma r/\rho$ is roughly equal to that for a heavy metal target of 2-cm diameter.

This suggests that studies of the radial pinch and angle shear should be performed with the ratio $B_0^2 D/v$ at a value 6 times the nominal for a muon-collider source, while studies of the axial shear should be performed with the ratio B_0^2/v roughly at the nominal value.

Since the Cell 4 magnet at the NHMFL has the same field B_0 and very nearly the same diameter D as the nominal muon-collider parameters, studies of the radial pinch and angle shear can be done with jet velocities 1/6 nominal, while studies of the axial shear should be done at the nominal jet velocity of 10-20 m/s.

The jet (sec. 3.1.3) will be propelled downwards into the vertical bore of the Cell 4 magnet. A thin-walled stainless-steel vessel will contain the jet. The primary diagnostic of the jet's motion will be a Hadland Photonics IMACON 790 framing streak camera available at the NHMFL.

3.3 Liquid-Metal Jet with a Proton Beam

The initial tests of a liquid-jet target in a proton beam (sec. 3.1) involve beam intensities and jet radii that are both scaled down relative to their nominal values, so as to keep the peak energy deposition density at the nominal value. It is still desirable to test a full-scale target in a beam of full intensity, to test for possible effects that scale with total energy deposition.

3.3.1 Full-Scale Liquid-Metal Jet

A full-scale liquid target will have a radius of 1 cm and a length of about 30 cm. The mass of metal in a single pulse of the jet approaches 1 kg. If the jet velocity were as high as 30 m/s, the kinetic energy of the metal would be 1 kJ. At the nominal pulse rate of 15 Hz the mechanical power in the jet would be 15 kW, which power would be dissipated as heat in the vessel that "catches" the jet.

The proposed tests of a full-scale jet can be performed at a very low pulse rate – a few pulses/hour – so heating of the apparatus by the jet will not be an issue.

However, production of even a single 2-cm-diameter jet pulse involves considerable technical challenge. The critical item is the fast valve whose opening and closing defines the pulse length. For a velocity of 30 m/s, a jet of 30-cm length lasts 10 msec. The opening and closing times of the valve must be short compared to this; say, of order 1 ms. But to produce that velocity, the metal must be pressurized to at least 50 atm. according to eq. (9). The valve must then be able to exert a force of order 1000 N (assuming the plunger has area 2 cm^2 against the pressure).

At present we have not located a commercial valve that meets such specifications, although the search has just begun. A custom valve may need to be commissioned.

For the full-scale test, we might compromise on a jet with a considerably longer pulse length. (Indeed, the option of a continually flowing jet is not excluded for the muon-collider source). Such a jet would, of course, require a significantly larger inventory of liquid metal during the tests.

3.3.2 Fast Extracted Beam with 10^{14} Protons

As discussed in Appendix B, the AGS is now being upgraded to accelerate 1-2 $\times 10^{14}$ protons/cycle (from its present record of 6×10^{13}). The protons are stored in 6 bunches in the AGS ring. At present, only one of these bunches can be extracted into the FEB, due to limitations of the G10 extraction kicker.

A new pulse-forming network for the kicker has been designed to render it capable of extracting all six bunches, but the design has not been implemented as yet.

3.4 Liquid-Metal Jet with a Proton Beam in a 20-T Magnet

The final phase of studies to establish the basic functionality of a liquid-metal target for a muon-collider source involves the addition of a 20-T magnetic field around the target to capture all particle produced with transverse momenta less than 225 Mev/c.

The magnetic field will perturb the motion of the jet, as discussed in sec. 2.5 and investigated for a scaled-down jet as in sec. 3.2. However, the field will damp the hydrodynamic transients caused by the beam-induced pressure wave (sec. 2.5.2). The complexity of these effects is such that detailed assessment of their magnitude requires direct measurement.

The 20-T magnet need not be continuous duty. The proposed study can be made with a pulsed magnet that cycles a few times an hour.

3.4.1 The 20-T Pulsed Magnet

A pulsed magnet that can deliver a field on the target in excess of 18 T for 600 ms is sketched in Fig. 28. It is comprised of 9 tons of circular copper coils that are arranged in two groups: outer and inner. A 4-MW power supply first energizes the outer coils to a field of 10 T. Then the coils are switched so as to transfer some of energy stored in the outer coils quickly into the inner coils. After a designated "flattop" length, the energy of the both coil groups is switched into an external load. The time dependences of the fields and other parameters of the system are shown in Fig. 29.

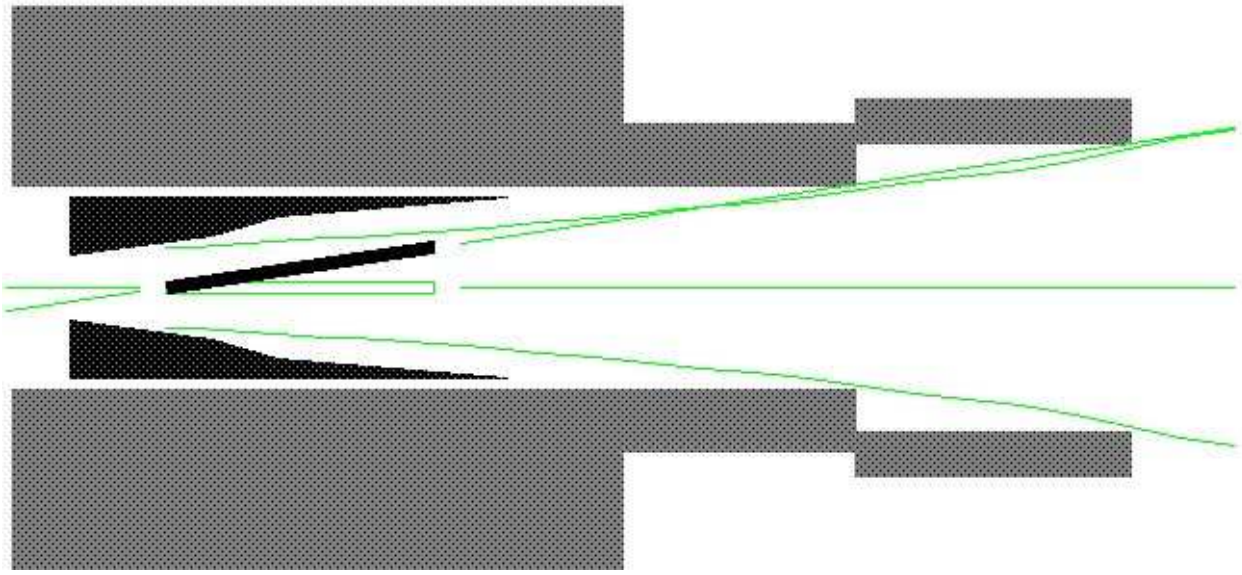

Figure 28: Section through an arrangement of pulsed-coils that can deliver a peak field of 20 T around the target for about 2/3 s. The proton beam is at an angle of 150 mrad to the axis of the magnetic field. The beam dump is incorporated into the magnet structure.

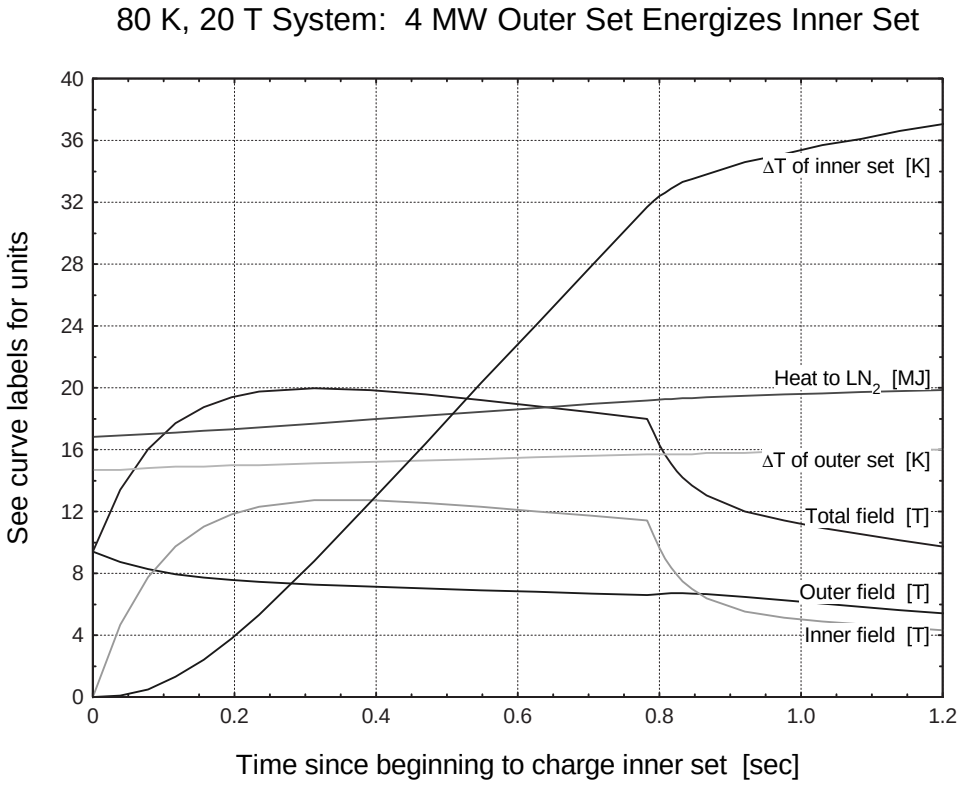

Figure 29: Time evolution of various parameters of the 20-T pulsed magnet.

The coils are to be operated at liquid nitrogen temperature to reduce the resistivity of the copper. The temperature rise during one pulse of the magnet is about 40°C, and the subsequent recooling time is about 10 min. The temperature rise is higher for longer "flattop" lengths, as is also the variation of the field strength during the "flattop". See Fig. 30.

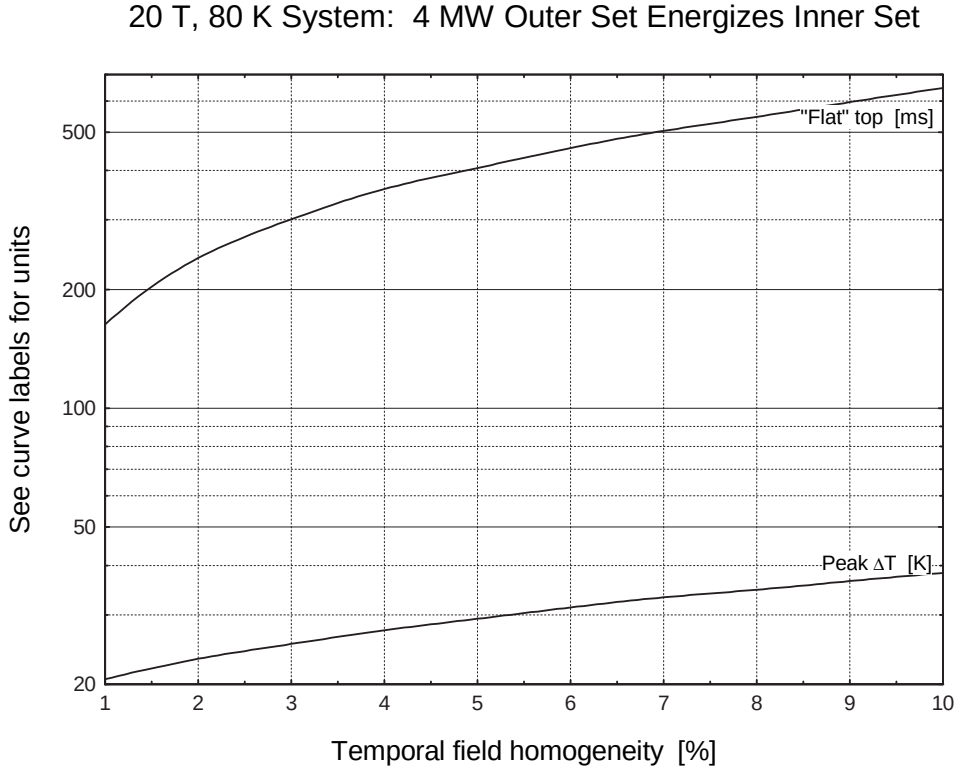

Figure 30: The length of the "flattop" of the pulse and the temperature rise ΔT in the 20-T pulsed magnet as a function of the field variation during the "flattop".

The present 4-MW power supply for the MPS magnet would be suitable for energizing the above magnet. It would be relocated to an enclosure next to the U-line.

3.4.2 Site of the Later Phases of the Program

The studies proposed in secs. 3.4-7 involve larger physical facilities in the U-line than those of secs. 3.1-3. If an iron return yoke is added to the 1.25-T solenoid magnet of sec. 3.6, the setup will be larger in diameter than the present U-line tunnel. Also, installation and commissioning of these facilities will require considerable time spent in the tunnel. As shown in Fig. 17, the residual radiation level is quite high in the neutrino blockhouse.

Hence, we propose that the later phases of the program be sited downstream of the neutrino blockhouse. A suitable location would be near Gate #5 of the U-line, as shown in Fig. 31.

An important concern is that our apparatus does not become excessively radioactive due to other use of the U-line. As shown in Figs. 28, 31 and 36, the proton beam dump is incorporated into the structure of the 1.25-20-T magnet system.

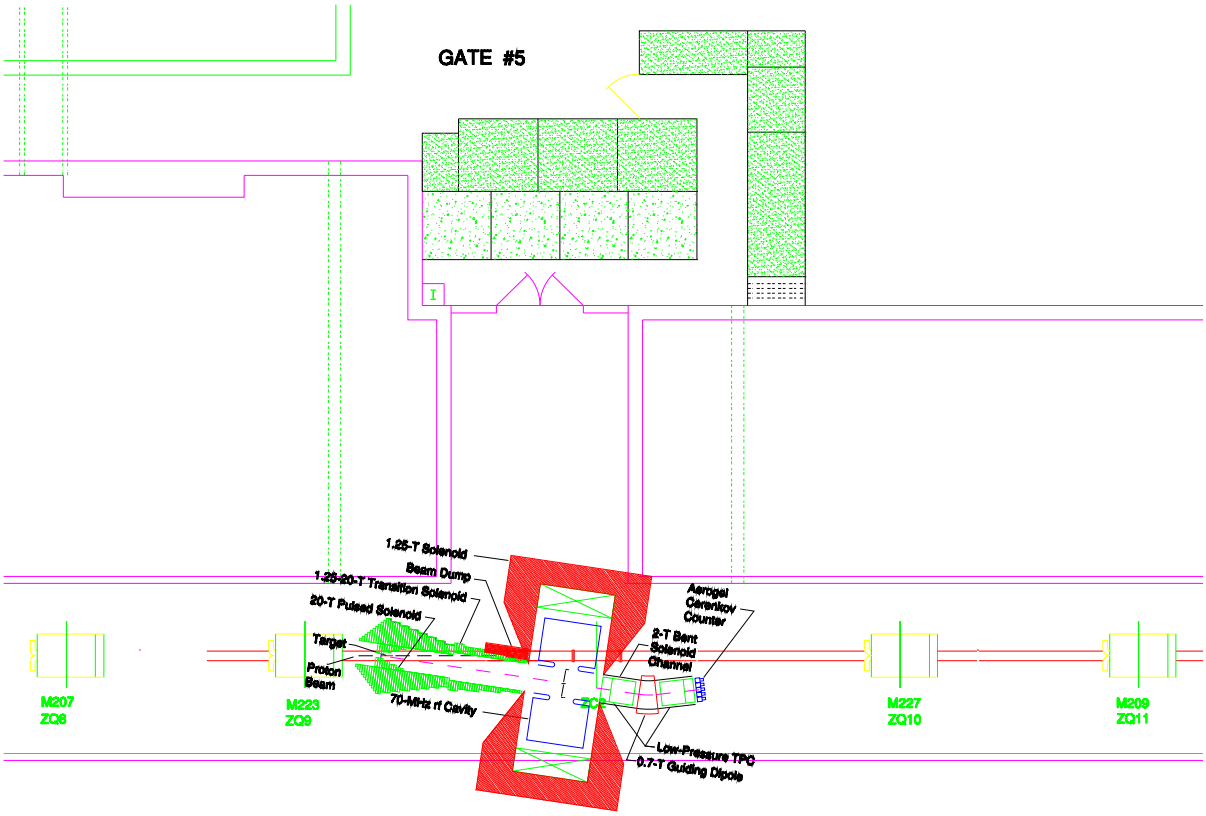

Figure 31: Possible arrangement of the targetry experiment near Gate #5 in the FEB U-line. Details of the experiment as shown in Fig. 36.

If the U-line is to continue to be used for other studies in which large amounts of beam are delivered, our apparatus should be located downstream of a removable beam dump.

3.5 RF Cavity near the Target

For the $\mu^+\mu^-$ collection system discussed in sec. 2.6 to be viable, the rf cells must operate at the levels required of them. In particular, the first cells should be operated at the highest possible peak-power levels order to obtain the maximum accelerating gradient at the front end. Also, the initial rf cells must perform satisfactorily in the high-radiation environment immediately following the target. Since experience operating an rf cell in a high-radiation environment generated by a beam of 10^{14} protons/pulse is limited, we propose to establish a proof-of-principle demonstration of this issue by constructing and operating at high gradients an rf cavity with a frequency suitable for a muon-collider collection system.

A key issue is the rf power required for such a test. A search of available rf sources in the upper frequency range of our requirements has led us to a 70-MHz rf power source which is now available at LBL as the result of retirement of the HILAC facility. We therefore focus our efforts on the design and utilization of a system using this frequency. As a baseline, we consider an rf accelerating cell (Fig. 32) with parameters given in Table 6 for operation of

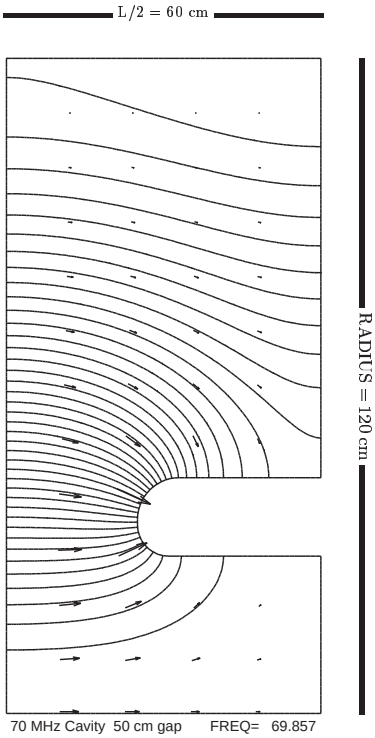

Figure 32: SUPERFISH solution for a 70-MHz rf cavity, a quarter section of which is shown.

the rf cavity at a level of 2 kilpatricks (corresponding to peak electric gradients of 20 MV/m on the cavity wall).

The R&D program would entail constructing a 70-MHz rf cavity, first powering it to maximum power levels without beam/target interactions, and then determining the maximum power levels achievable with the high-radiation environment present with beam/target interactions.

Possible breakdown of the rf cavity is associated with discharges induced by field-emission electrons, as well as secondary emission of electrons from the cavity walls during that passage of particles produced in the target. A study of the latter effect is the main goal of phases 5 and 6 of the present proposal.

Beam-induced breakdown of the cavity is sensitive to the time of emission of the electron in the rf cycle. A realistic test of cavity performance at high beam intensities requires the time structure of the beam to match that expected at a muon-collider source. There, the beam pulse should be 2 ns or less, to maximize the number of pions that are accelerated in a single rf cycle. Hence, we desire beam pulses in the U-line that have similar duration.

It may not be possible to obtain such narrow beam pulse widths at 24 GeV, but pulses with $\sigma_t = 2$ ns have been demonstrated at the AGS at 7 GeV [107]. At least, some portion of the rf-cavity tests should be made with this beam.

The rf breakdown problems will no doubt be sensitive to the total number of protons in the beam. Hence, we desire to perform tests with 10^{14} extracted protons. At the AGS, this will be possible only for 6-bunch extraction (sec. 3.4) over a total period of 1 μs. While this

Table 6: 70-MHz rf-cavity parameters.

RF Frequency (MHz)	70
Cavity Length (cm)	120
Full Gap Length (cm)	50
Cavity Radius (cm)	125
Beam Pipe Full Aperture (cm)	60
$Q/1000$ (from SFISH)	63.1
Av. Gradient (MV/m)	5.0
RF Peak Power (MW)	2.4
Stored Energy (J)	330

may not be fully equivalent to 10^{14} protons in a single rf bucket, tests should be made at the highest intensities available in the U-line.

3.6 RF Cavity Inside a 1.25-T Magnet near the Target

A further requirement of the muon-collider phase-rotation channel (sec. 1.2.4) is to envelope the entire rf channel within a solenoidal field of 1.25 T. It is desirable to have this field be as uniform as possible to avoid particle losses through resonant effects. These effects are pronounced if, for example, one places solenoid coils between the rf cells (Fig. 33a), thereby giving the longitudinal structure of the solenoidal field an oscillating structure with amplitude variations (Fig. 34). We avoid this problem by placing the entire rf channel within the coils of the solenoids, with the penalty of increasing the warm-bore aperture of the solenoids (Fig. 33b).

The beam requirements for the study of the rf cavity inside a magnetic field are similar to those of the study without field (sec. 3.5).

We consider two variations of solenoids with the 240-cm warm-bore aperture required to fully envelope the 70-MHz rf cell: a superconducting magnet and a resistive magnet.

A superconducting solenoid with such an aperture and capable of generating a 1.25-T field can be constructed at a cost of $1.2 M. A preliminary design for this is underway at LBL.

A resistive solenoid would be very similar to that now used in BNL experiment E-787, and is sketched in Fig. 36. The performance of such a magnet, with a 20-ton copper coil and 140-ton iron return-flux yoke, is shown in Fig. 35. The power required would be 1.2 MW.

Similar performance could be obtained from a design with an 11-ton aluminum coil and a 170-ton iron yoke.

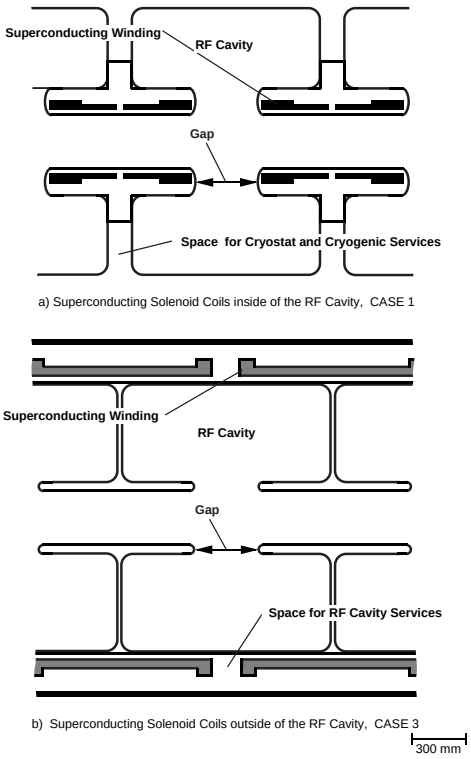

Figure 33: Different locations of solenoid coils for a phase-rotation system.

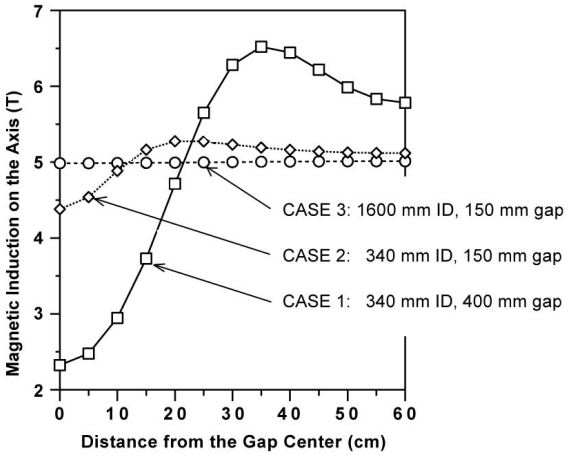

Figure 34: Magnetic induction along the beam axis for three different coil-placement scenarios.

3.7 Characterization of the Pion Yield from the Target

We propose as a final phase in the R&D program to measure the pion yield produced and collected by the prototype system. The number of captured pion/muons per incident proton is a critical parameter for the success of a muon collider. A measurement of this quantity would confirm and extend previous measurements of the pion-production yield and on the

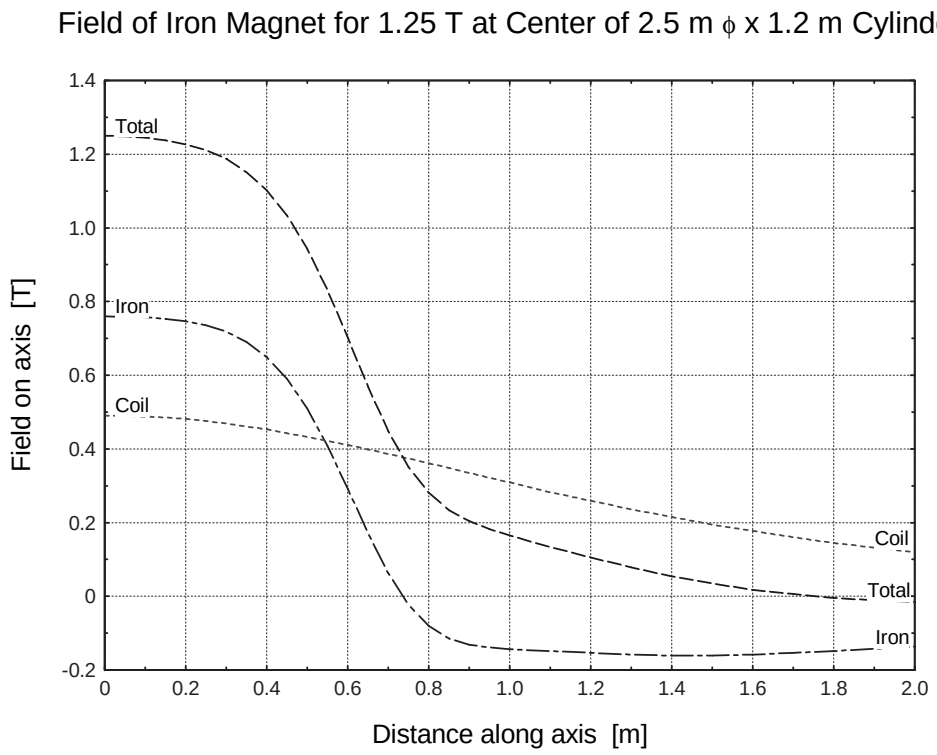

Figure 35: Performance of a 1.25-T resistive magnet.

simulation codes used for designing the collection system.

3.7.1 Overview

The quantity we wish to measure is $dN_\pi(B)/dPrdrd\phi$, where $N_\pi(B)$ is the number of identified pions (or muons) for a peak field B in the collection solenoid, dP is the momentum bin, and $rdrd\phi$ is the cross-sectional area of the bin at some plane following the collection system. The asymmetry of the production target with respect to the axis of the solenoid causes the distribution to be non-uniform in azimuthal angle ϕ.

As a primary requirement, we seek a momentum resolution of $\sigma_P/P \leq 0.05$ over the entire momentum interval $100 < P_\pi < 500$ MeV/c. Another important constraint on the detector design is the need to distinguish pions and muons from other particles (electrons, protons, kaons), although we need not distinguish between pions and muons.

A schematic drawing of the proposed experiment is shown in Fig. 36.

In this study, as for the rf-cavity studies, it would be sufficient to use a solid target. However, the 20-T capture field is an essential ingredient.

3.7.2 AGS Beam Requirements

Unlike the previous parts of the proposal, the characterization of the pion yield will require slow extracted beam. We would need only about 10^6 protons per pulse (so as to have only about 10 interactions during the 8-μs drift time of the TPC's in the detector). For

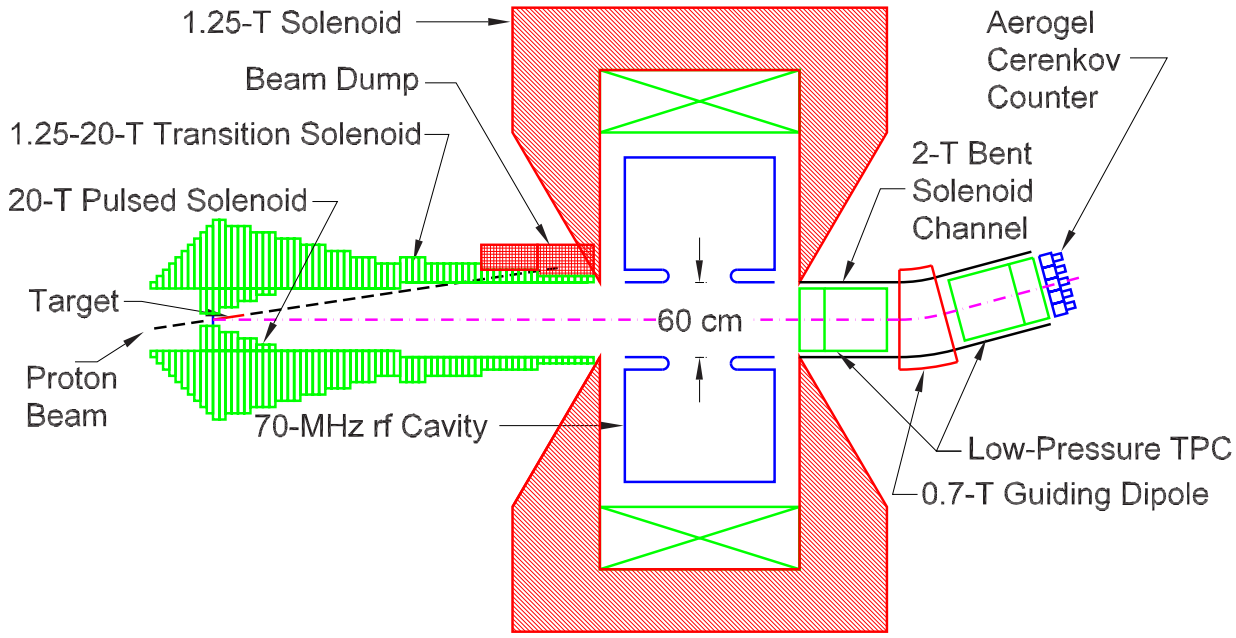

Figure 36: Plan view of the full configuration of the targetry experiment.

compatibility with the 20-T pulsed solenoid the protons should be uniformly distributed over a $\approx$ 600-ms spill. The repetition rate required is only 10/hour. The spot size on the target should be ≈ 0.5 cm^2 ($\sigma_r \approx 4$ mm).

Slow extraction has not been available up to now in the U-line. The main obstacle is the H10 extraction septum. Presently, it is pulsed to prevent it from burning up. To operate it continuously would require a new magnet and power supply (expensive). It may be possible to build a new PFN to run the magnet with a pulse that has a 600-ms-long flat top at a low duty cycle.

However, operation of the U-line with only 10^6 protons will require new beam diagnostics suitable for such low intensities. It may be possible to run the U-line as a 24-GeV secondary beam line with the H10 septum coil as the target. In this case, the beam tune for the line would be different from that during the regular FEB operation. Beam monitors would be needed to measure the position and angle of the protons incident on the test target, as well as a Čerenkov counter to establish that the beam particle is a proton.

3.7.3 Momentum Spectrometer

Since the target and rf cavity are enclosed in a solenoidal field, it is natural to use a bent solenoid to provide the dispersion needed in the spectrometer. Particle-position measurements will be made using two Time Projection Chambers (TPC's) that surround a bend in the solenoid channel. This spectrometer arrangement is similar to one proposed for the Ionization Cooling Test Facility (MUCOOL) experiment [14, 117] at FNAL.

General Features of a Bent Solenoid. In any solenoid, individual charged particles undergo helical trajectories around a "guide" trajectory. In a bent solenoid, the guide trajectory is deflected perpendicular to the plane of the bend of the solenoid, taken to be the horizontal (x-z) plane. This deflection is known as "curvature drift", and the amount of deflection is proportional to the particle's momentum.

If a vertical dipole field is superimposed over the curved part of the solenoid, one reference momentum P_0 will pass through with its guide trajectory undeflected [117]. Particles with momenta $P < P_0$ will have their guide trajectory deflected, say, upwards, while those with $P > P_0$ will have their guide trajectory deflected downwards. We take the reference momentum for the spectrometer to be $P_0 = 300$ MeV/c, since that is the center of the momentum range of interest. The guide dipole field that leaves the reference momentum undeflected in a solenoid whose bend has radius of curvature $R_{\rm bend}$ is [117]

$$B_G = \frac{P_0}{eR_{\rm bend}}. \tag{69}$$

For example, with $P_0 = 300$ MeV/c and $R_{\rm bend} = 1.4$ m, we find that $B_G = 0.714$ T.

The vertical deflection of the guide trajectory of an off-momentum particle is given by

$$y_G = \frac{P_0}{eB_S}\frac{\Delta P}{P_0}\theta_{\rm bend}, \tag{70}$$

where B_S is the solenoid field strength, and $\theta_{\rm bend}$ is the bend angle (in the plane of the bent solenoid). It is noteworthy that the deflection is greater for weaker fields. However, the momentum resolution obtainable in a spectrometer based on a bent solenoid varies as $1/(B_S\theta_{\rm bend})$, so that a stronger field gives better resolution (eq. (74) below) as is to be expected [117].

While the beam is contained within a circular aperture, defined as R_S prior to the bend, the effect of the deflection is to deform the beam into an ellipse with semimajor axis $R_S + y_G$ after the bend. The downstream solenoid and detector must be large enough to accommodate this. Hence, we desire to minimize both R_S and y_G, which implies large B_S, but small $\theta_{\rm bend}$.

Individual particles undergo Larmor oscillations around the guide trajectories with radius of curvature given by

$$R_{\rm Larm} = \frac{P_\perp}{eB_S}. \tag{71}$$

Since the product $B_S R_{\rm Larm}^2 \propto P_\perp R_{\rm Larm}$ is adiabatically invariant, and we must have $R_S \geq R_{\rm Larm}$, we obtain the relation

$$B_S R_S^2 = \text{constant}. \tag{72}$$

The weight of the coil of the bent solenoid varies roughly as R_S, while the power consumed (by a resistive coil) varies as roughly as $B_S^2 R_S$. Then according to eq. (72), the power consumption will vary roughly as $B_S^{3/2}$. In general, this favors a lower-field, more massive coil. Figure 37 shows the power consumption calculated for various coil options that produce a 2-T field; a 9-ton copper coil would consume 1.42 MW.

In the present case, particle trajectories evolve adiabatically from the capture solenoid, whose field is $B_{S,0} = 20$ T, to the spectrometer solenoid. Then, eq. (72) also tells us that

$$R_S(B_S) = R_{S,0}\sqrt{\frac{B_{S,0}}{B_S}}. \tag{73}$$

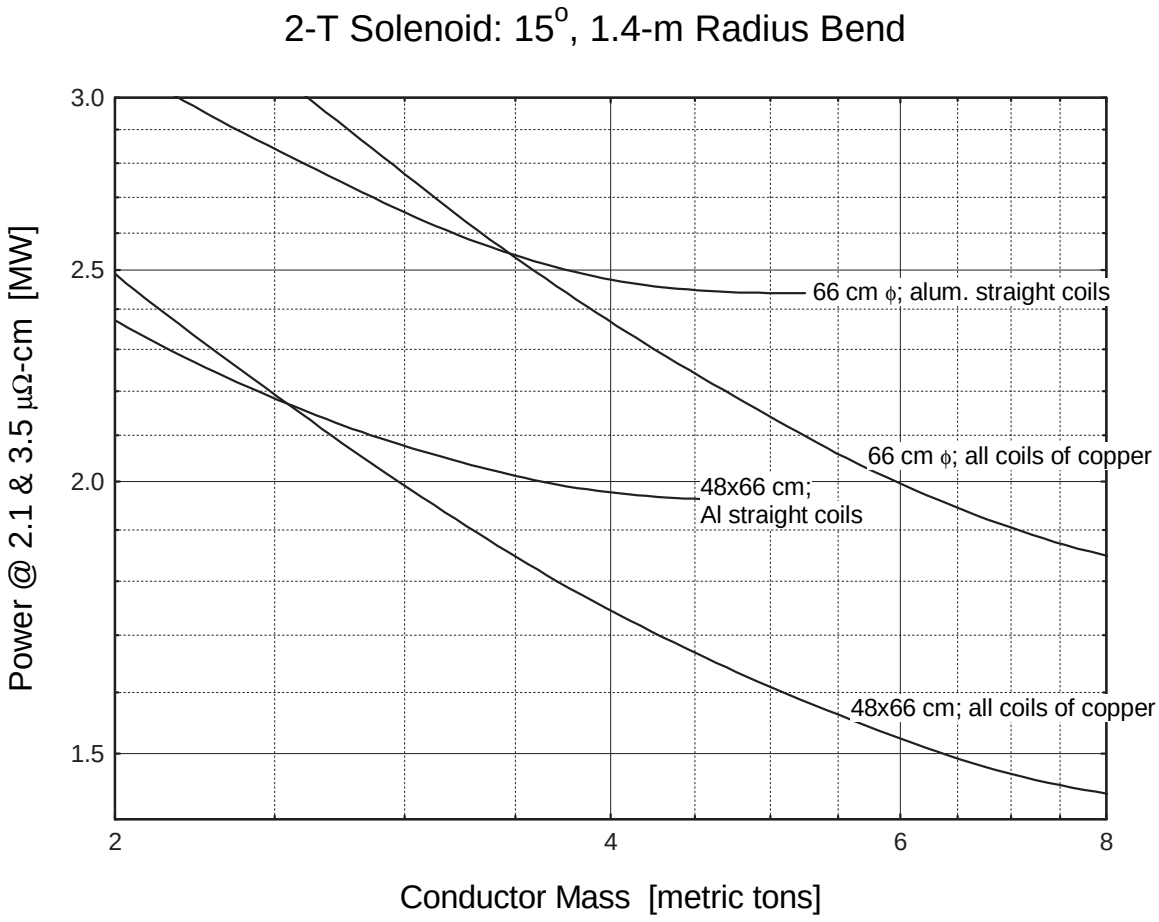

Figure 37: Power consumption of various coil options for a 2-T, 15° bent solenoid.

The aperture of the capture solenoid is $R_{S,0} = 7.5$ cm, corresponding to good capture efficiency up to transverse momentum $P_{\perp,0} = 225$ MeV/c.

Thus, if we choose $B_S = 2$ T for the spectrometer solenoid we will have $R_S = 24$ cm, compared to $R_S = 30$ cm in the 1.25-T magnet surrounding the rf cavity.

From the adiabatic invariance we also expect the maximum transverse momentum of particles transmitted to a 2-T spectrometer to be 70 MeV/c and the maximum Larmor radius to be 11.7 cm.

The bend angle should be large to improve the momentum resolution, but small to minimize the vertical dispersion of the beam. We choose $\theta_{\rm bend} = 15°$ as a reasonable compromise. Then for the maximum momentum deviation of 67% from the reference momentum, the guide trajectory is deflected vertically by 9 cm. Thus, after the bend the radius R_S of a circular aperture would need to be $24 + 9 = 33$ cm for full acceptance. However, since the dispersion occurs only in the vertical direction, we are also examining the possibility of constructing a racetrack-shaped solenoid coil downstream of the bend with elliptical aperture of 48 cm $\times$ 66 cm.

The parameters of the bent-solenoid spectrometer magnet are summarized in Table 7.

Table 7: Parameters of the analysis spectrometer magnet system. The length L_S includes both the bent and straight sections of the solenoid.

B_S	2 T
$R_{\rm bend}$	1.4 m
$\theta_{\rm bend}$	15°
$R_{S,\rm max}$	33 cm
L_S	1.4 m
B_G	0.714 T
$\Delta y_{G,\rm max}$	9 cm
$R_{\rm Larm,max}$	11.7 cm

Momentum Resolution of a Bent-Solenoid Spectrometer. A bent-solenoid spectrometer has a momentum resolution given by [117]

$$\frac{\sigma_P}{P} \approx \frac{P\sigma_x}{\theta_{\rm bend} e B_s L^{5/2}} \sqrt{\frac{720}{n}}, \tag{74}$$

when limited by position measurement accuracy σ_x. In this relation, L is the length over which the position measurements are made (active length of the TPC), and n is the number of measurements per unit length.

There is also a limit on resolution due to multiple scattering given by [117]

$$\frac{\sigma_P}{P} = \frac{13.6 \text{ MeV}/c}{P\beta\theta_{\rm bend}} \sqrt{N_X}, \tag{75}$$

where N_X is the number of radiation lengths of material encountered during the measurement.

While one can reduce multiple scattering by operating the tracking chamber at low pressure, this would limit the ability of the chamber to provide particle ID via dE/dx measurements. So we consider options to operate the chamber near atmospheric pressure, with acceptable levels of multiple scattering and high ionization density.

Table 8 lists relevant parameters for candidate gas mixtures and for the component simple gases. TPC's often have been operated with an AR/CH_4 (90/10) mixture because of its low saturation-drift voltage and reasonably good ionization density.

Table 9 includes the momentum resolution limits from eqs. (74-75) evaluated at the limits of the momentum range of interest in a chamber. Gas mixtures have been chosen for which the number n of samples/m is about 2,400. The chamber length is $L = 50$ cm, and we assume the position resolution from a single cluster is $\sigma_x = 300$ μm.

We see that the Ar/CH_4 (90/10) gas mixture causes too much multiple scattering to obtain 5% momentum resolution at 100-MeV/c momentum. This suggests the use of an

Table 8: Parameters for candidate chamber gases and their components, at STP and for minimum ionizing particles.

Parameter	He	Ar	CH_4	iC_4H_{10}	Ar/CH_4 (90/10)	He/iC_4H_{10} (75/25)
Atomic number	2	18	10	34		
Primary clusters/cm (STP)	4	25	25	84	25	25
Radiation lengths/m	0.0002	0.0091	0.0015	0.0059	0.0083	0.0016
Saturation E field (kV/cm)	–	–	0.9	1.5	0.2	≈ 1.5
Voltage for 50 cm (kV)	–	–	45	75	10	75
Saturation drift velocity (cm/μs)	–	–	10	5	6	3
Drift time over 50 cm (μsec)	–	–	5	10	8	17

Table 9: Limits on momentum resolution in the proposed spectrometer due to position resolution of the TPC's and to multiple scattering.

P (MeV/c)	β_π	Position ($n = 2400$/m)	Scattering Ar/CH_4 (90/10)	Scattering iC_4H_{10} (225 Torr)
100	0.58	0.0006	0.086	0.038
500	0.96	0.003	0.017	0.008

atmospheric-pressure helium/isobutane gas mixture, as has become popular at B-factories [118]. The price for this would be a rather high operating voltage for the TPC. Instead, we propose to use pure iC_4H_{10} at 225 Torr, which should permit twice as good momentum resolution as the Ar/CH_4 (90/10) mixture and the same dE/dx resolution, and requires operating the chamber at only 2.5 times higher voltage, *i.e.*, 25 kV for a 50-cm-long chamber.

The TPC parameters are summarized in Table 10. For comparison, the TPC's under development for MUCOOL [14, 117] have a position accuracy of $\sigma_x = 200$ μm, measurement length $L = 43$ cm, $n = 33$ measurements per meter, and 0.0002 radiation lengths of material.

Table 10: Parameters of the TPC's.

Radius (TPC_1)	24 cm
Area (TPC_2)	$48 \times 66\,\pi/4$ cm^2
L	50 cm
σ_x	300 μm
Gas	iC_4H_{10} @ 225 Torr
Voltage	25 kV
Charge samples (n)	2400/m
N_X	0.0016 rad. lengths
Drift time	8 μs
Readout time	30 ms

3.7.4 Particle Identification

Particle identification is an essential component of this experiment. Besides the pions and muons the outgoing flux will contain a substantial background of electrons and protons. In addition, we expect kaon production (some of which is potentially useful as a source of muons) at approximately 10% of the pion rate. However, it is not necessary for our purposes to distinguish pions from muons; we ultimately desire to know the rate of captured muons, but essentially all pion decays result in muons that remain captured in the solenoid channel.

We plan to base the particle identification on a combination of dE/dx measurements from the TPC's and a threshold Čerenkov counter. A time-of-flight system was considered, but it is difficult to construct a "start" counter suitable for 100-MeV/c pions (32 keV) with the required precision.

Identification of most particles will be provided by readout of the ionization density in the TPC. Each track will yield $\approx 2,400$ primary ionizations over the total of one meter of path length in the TPC's, corresponding to a dE/dx resolution of 5-6% (σ). Figure 38 shows data collected with a TPC during BNL experiment E-910 for which a similar ionization density held [23] (see also Appendix A). Kaons and protons (and light nuclei) will be distinguished from pions and muons over the entire interval 100-500 MeV/c, and electrons are distinguished for momenta greater than about 250 MeV/c.

Electrons will also be identified by a positive signal in an aerogel threshold Čerenkov counter. The β of a 500-MeV/c muon is 0.98, so the radiator should have index about 1.01, as is now achieved in high-quality aerogels [121, 122, 123, 124, 125, 126, 127, 128, 129]. The aerogel would be subdivided into $5 \times 5 \times 15$ cm^3 cells, each viewed by a 3″-diameter Hamamatsu fine-mesh photomultiplier tube. A total of about 100 cells will cover the 48 cm $\times$ 66 cm beam ellipse at the downstream end of the bent-solenoid channel.

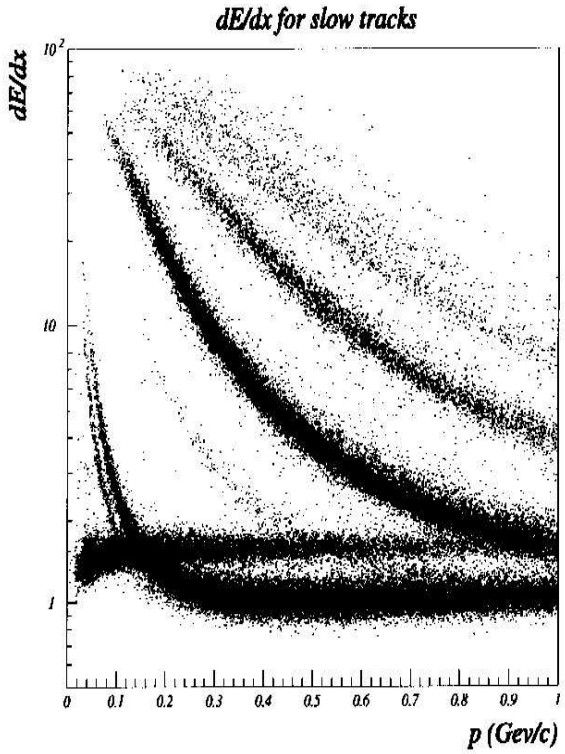

Figure 38: Ionization energy loss observed in the E-910 TPC for low-momentum tracks. Note the overlap of the (nearly horizontal) electron band with other species.

A charged particle other than an electron has about 5% probability of producing a knock-on electron that yields a signal in the aerogel detector. In view of the expected large number of low-energy protons in the spectrometer, the segmentation of the aerogel detector is justified.

In the system as described there would remain about a 5% loss of pions and muons below 250 MeV/c, due to mistagging from knock-ons in the aerogel. This inefficiency could be reduced to 0.2% at the expense of a second layer of aerogel detectors.

3.7.5 Expected Rates and Running Time

We expect about 1 collected pion per interacting proton in the momentum range of interest [1].

If the readout time is 30 ms per trigger, and the beam spill is 600 ms long, then we will record about 20 triggers/pulse. With 6 pulses/hour (limited by the time for the pulsed 20-T solenoid to recool), we will obtain about 120 triggers/hour.

The TPC readout is to be based on the STAR TPC electronics [130], which incorporates analog storage of 512 (or 1024) time samples in switched-capacitor arrays. While there are about 1,200 primary ionizations per track in the TPC, it is not necessary to sample each ionization separately. It should suffice to allot about 50 samples per track, clock at 6 MHz, for a total of 85 μs (if we use 512 samples, or 170 μs for 1024 samples). If the beam protons

are separated by 10 or more time samples, *i.e.*, by 1.6 μs or more, we should be able to identify different protons easily. Equivalently, we can process 50 (or 100) proton interactions per trigger with little time overlap among samples from different interactions. With this procedure, we can measure about 6,000 pions/hour with production kinematics of interest.

Although there is only about one pion per proton interaction of interest, there will be about 15 tracks per interaction, mostly from slow protons ejected from the target nuclei, in the TPC. See Fig. 46 of Appendix A. Thus a trigger that contained 50 proton interactions would consist of about 750 tracks in the TPC.

The collected pions of interest must be binned over the three phase variables P, r and ϕ. In addition, the field strength of the collection solenoid falls from 20 T to 18 T during the 600-ms beam spill. Thus the collected events must also be binned in magnetic field. If we require a total of 6 bins per variable, there are a total of $1,296$ bins. Then each 4-d bin receive only ≈ 15 events per hour. If we require $\approx 1,000$ events per bin to achieve 3% statistical accuracy, then we require ≈ 220 hours of beam operation. It should be emphasized, however, that during most of this time we do not need beam delivered to the experiment, so efficient operation in conjunction with other users may be possible.

3.8 Simulations of the Beam-Jet-Magnet Interaction

The R&D program presented in secs. 3.1-7 consists of laboratory studies, only some of which have parameters that match the baseline design for a muon-collider source in detail. Also, the baseline design may well evolve as the measurements are made and difficulties are understood. Hence, extrapolations will be needed from the observed data to other physical situations. Analytic scaling laws provide some guidance for this, but we also desire the additional insights as may be had from numerical simulation.

Most simulations of targetry issues have emphasized thermal-induced stress in solid targets, for example [50, 52], with some recent work on mercury targets for neutron spallation sources [54, 56, 57]. Such studies have often used the commercial code ANSYS [131], typically modelling the target as a solid. The effect of a strong magnetic field on the target has not been considered to date.

ANSYS now combines a fluid dynamics package, FLOTRAN, and an eddy-current package, Emag, together with its Mechanical and Thermal packages in an overall architecture, Multiphysics. We have begun, and propose to continue, use of the ANSYS/Multiphysics package to model the beam-jet-magnet interaction. An early result is shown in Fig. 39.

However, it is clear that the complexity of the beam-jet-magnet interaction is beyond that studied in most ANSYS simulations, and considerable effort will be required to obtain useful results. We therefore also propose to utilize research codes developed for simulation of thermal hydraulics.

3.8.1 The HEIGHTS Simulation Package

The HEIGHTS package has been developed at Argonne National Laboratory to study **H**igh **E**nergy **I**nteractions with **G**eneral **H**eterogeneous **T**arget **S**ystems. This is a 2-dimensional particle-in-cell (2-D PIC) code consisting of nine modules as sketched in Fig. 40.

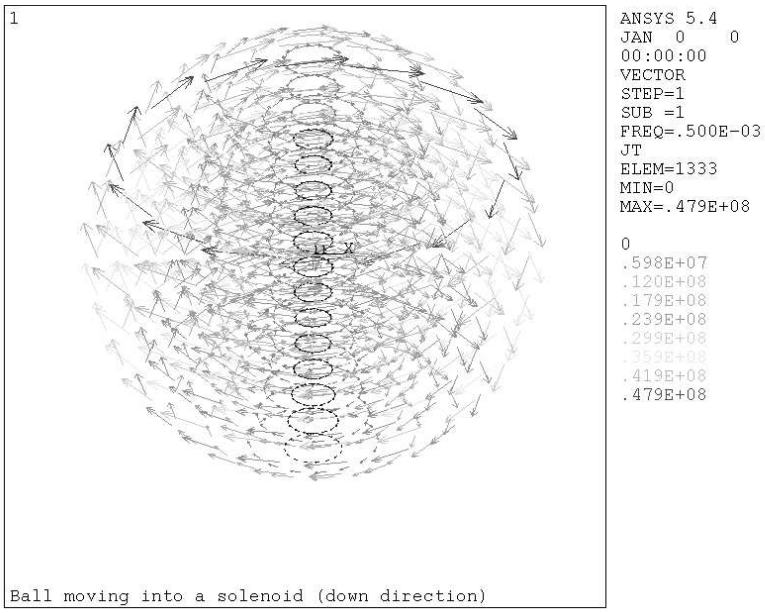

Figure 39: ANSYS/Emag simulation eddy currents induced in a conducting sphere moving through the fringe field of a solenoid magnet.

The HEIGHTS package will be used to study the motion of a liquid-metal jet in a strong and inhomogeneous magnetic field, including the hydrodynamic instability of the liquid jet, thermal stresses, and the shockwave effects resulting from the sudden deposition of the proton energy in the liquid target. Examples of past studies using this code include [132, 133, 134, 135].

Details of the proton cascade in the target will be simulated with the MARS Monte Carlo code, and provided as input to the HEIGHTS simulation.

Jet Heating and Expansion. We propose to perform detailed simulation of the dynamics of a cylindrical column of radius r_0 of the liquid metal either with a free surface or confined by a solid cylinder (pipe). The transport equations of continuity, motion, and heat balance are to be solved in a strong magnetic field, using the particle-in-cell (PIC) method in cylindrical coordinates (r, z) assuming symmetry in azimuthal angle ϕ. The problem of stability as a function of angle ϕ will be solved separately.

Because the deposited energy $Q_{\rm beam}$ depends on r and z it is necessary to calculate the motion of the medium in both coordinates. The existence of a free surface requires the use of a Lagrangian description for the numerical mesh of the target. However, to avoid the problem of large distortion of the hydrodynamic cells it is necessary to use a mixed Eulerian-Lagrangian scheme. An adequate description can be achieved using the 2-D PIC method recently implemented in the A*THERMAL-S code, the structure of which is sketched in Fig. 41.

The results from the computer simulation will show whether a pressure wave is generated inside the liquid jet and, in addition, study the consequences of such shockwave on jet behavior and stability. The magnitude of the pressure wave and its propagation/reflection

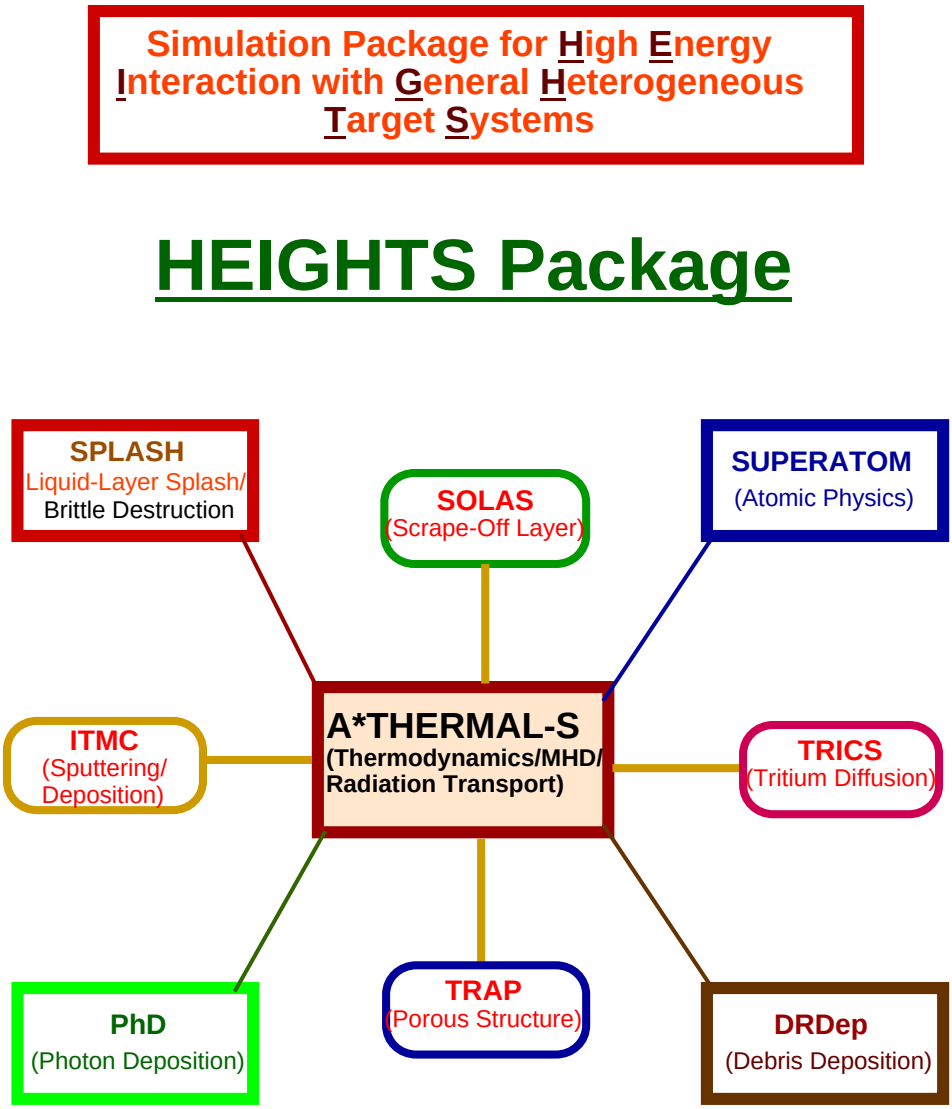

Figure 40: Block diagram of the HEIGHTS simulation package.

will determine the severity of jet breakup and distortion.

In the case of a strong pressure wave that is generated inside the jet and, as a result, the jet is broken into energetic droplets flying inside the magnet, the SPLASH code (Fig. 42) can then be used to study the droplet impacts on the chamber wall. The current SPLASH code models the hydrodynamic stability and splashing effects of a free surface of a liquid-metal layer subject to various forces acting on this liquid layer. The code can also model macroscopic erosion of a solid target from brittle destruction due to thermal stresses. We can easily implement models to study wall impact and erosion from the impinging of the energetic liquid-droplets.

Liquid-Jet Dynamics in a Strong Inhomogeneous Magnetic Field. The liquid-metal conductivity σ is not small; therefore, the magnetic-field diffusion time $\tau = \mu_0 \sigma r_0^2$,

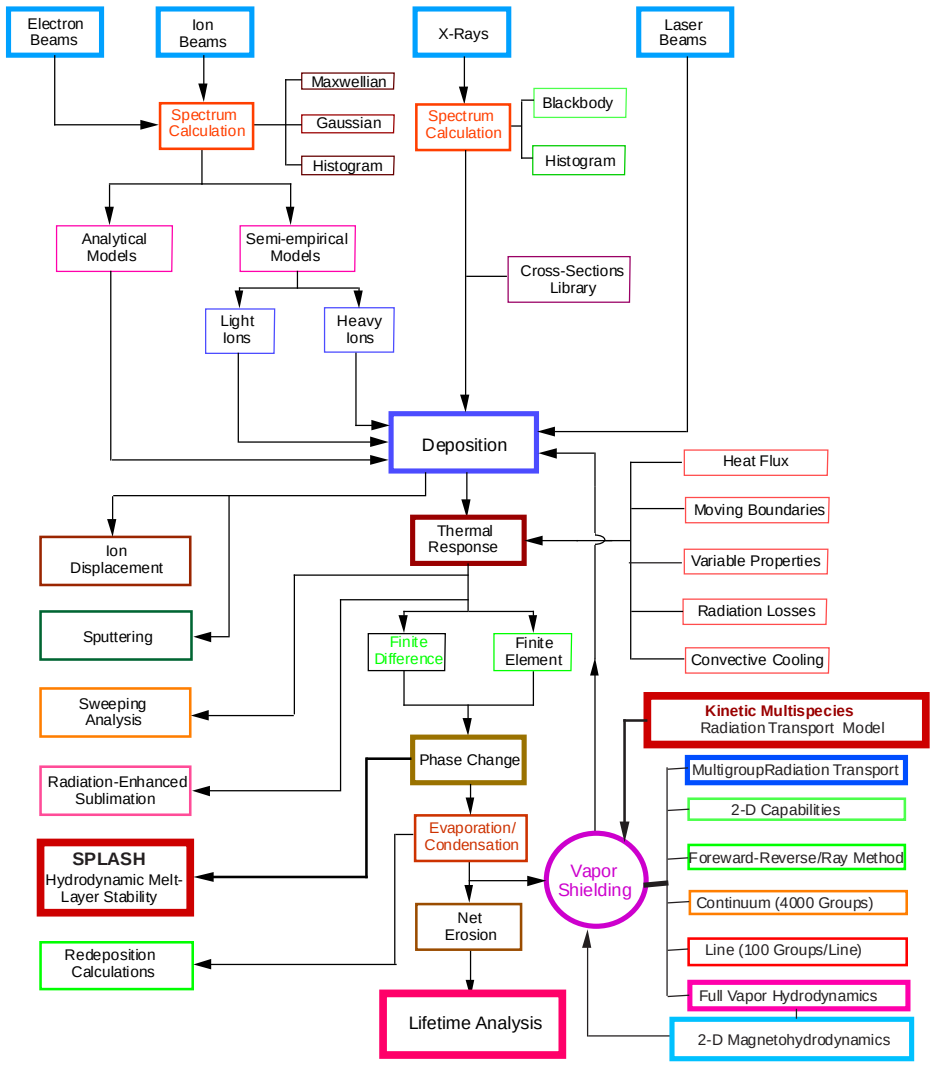

Figure 41: Block diagram of the A*THERMAL-S simulation package.

eq. (13), approaches the flight time of the jet. Then most of the external magnetic field penetrates into the liquid jet, and the resulting Lorentz force deflects the trajectory of the jet. To calculate the trajectory and to choose better conditions for the energy deposition and pion production, detailed magnetohydrodynamic (MHD) analysis is necessary of the jet dynamics in an inhomogeneous magnetic field (near both ends of the coils). This problem can also be studied using the A*THERMAL-S code; including all components of the electromagnetic forces, however, may require some modifications of the code.

Eddy-Current Effects. As the liquid metal propagates through the inhomogeneous magnetic field, eddy currents are induced in the metal. Then, because of the existence of a radial component of magnetic field, the jet velocity field will be distorted (sec. 2.5.1). This may

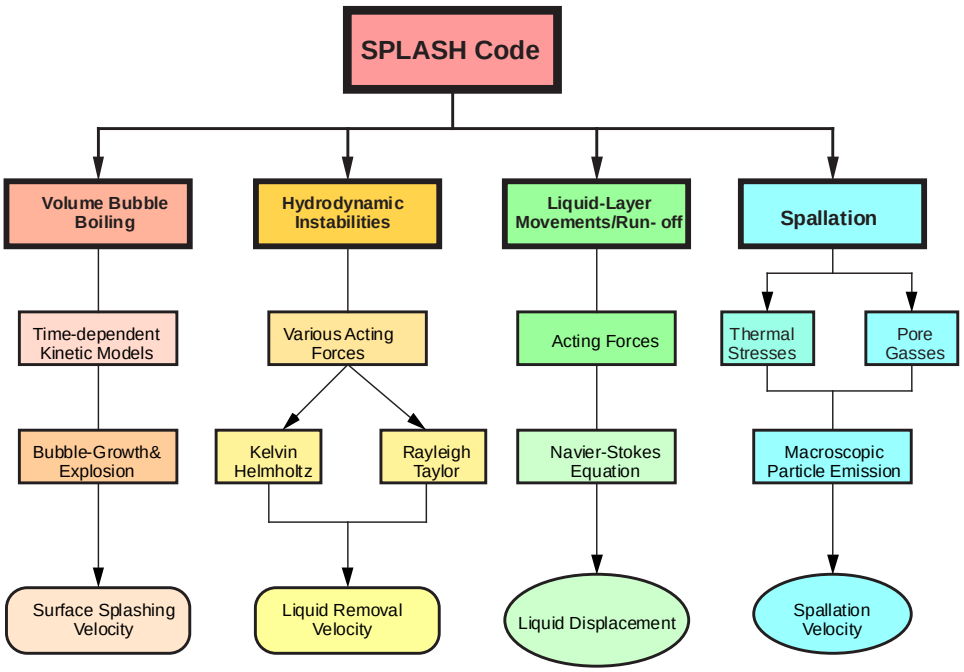

Figure 42: Block diagram of the SPLASH simulation package.

alter the shape of the jet from a circular form to an elliptical one. Decreasing the value of the magnetic field from coil inner surface to the z axis may stabilize this instability. The analysis of this problem can be made analytically using the conventional MHD stability theory.

Capillary Instability. Another problem is how to inject a free-surface liquid jet into an inhomogeneous magnetic field. During jet injection the hydrodynamic instability due to capillary forces evolves with characteristic rate $\Gamma = \sqrt{2T/\rho r_0^3}$, where T is the surface tension and ρ is the density of the liquid. The time of this instability, $\tau_T \approx 10/\Gamma$, is a few ms, which is comparable to or less than the flight time of the jet. Therefore the development of this instability could result in the dividing of the liquid jet into small droplets with size about $0.1r_0$. As discussed in sec. 2.5.3, this instability is expected to be damped by the strong magnetic field of the capture solenoid. This problem can also be modeled analytically using the conventional MHD theory and experimental data of time of droplet formation and droplets size.

3.8.2 Validation of the Simulations via Exploding-Wire Studies

In addition to such validation of the simulations as will be possible from the studies of secs. 3.1-4, we propose to study the effects of rapid energy deposition in a cylinder of liquid metal using exploding-wire technology. Such experiments could potentially be much less expensive than beam-on-target tests, and offer greater ease in varying parameters of the system. We propose to evaluate the extent to which exploding wires in liquid metals could provide useful, target-relevant information and set up a simple test stand to obtain some

first results. Our computer modeling capability will be used to guide the testing, interpret the results, and evaluate the relevancy to actual beam-on-target tests. Initial testing would be done in a static or slowly flowing liquid metal and without a magnetic field. Follow-on testing would include a magnetic field and target motion.

A schematic illustration of the suggested facility is given in Fig. 43. The liquid can be pumped from the chamber bottom to chamber top and falls freely in the form of a jet. The (insulated) wire is placed in the center of the falling liquid jet and is heated by the electric current from the discharge of a condensor bank during a time $\tau_{\rm bank} \approx 1$ μs. Facilities with similar parameters exist in many institutions, in particular at the TRINITI (Troitsk, Russia; contactperson V. Belan) or at the Kurchatov Institute (Russia). Studies of an exploding mercury jet have been reported in [66, 67, 68].

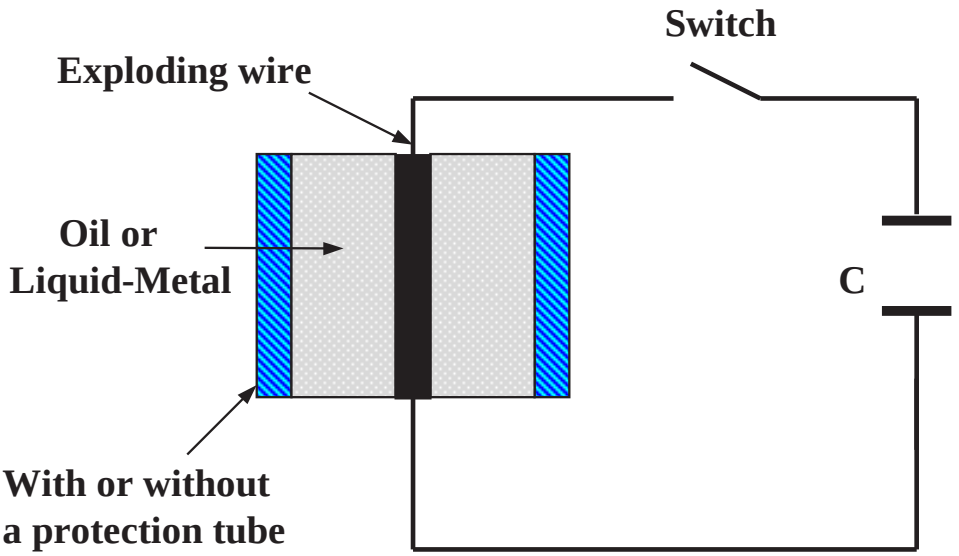

Figure 43: An exploding-wire facility to study rapid energy deposition in liquids.

System Requirements. To model and simulate the processes of rapid heating of a liquid target and possible resulting instabilities, one needs experiments with intense heating of the central zone of a cylindrical liquid jet of radius r_0 that meet the following conditions:

1. The heat deposited, Q_0, should be comparable to that in the muon-collider target, roughly 30 J/g (of target material, not of wire).

2. The heating time τ_Q should be less than the hydrodynamic time $\tau_r = r_0/v$, where v is the speed of sound in the liquid.

3. The length L of the liquid column should be much larger than the column radius r_0, to exclude three-dimensional effects.

4. The liquid should be one of the candidates (Ga/Sn, Hg, Bi/Pb, *etc.*) for use as the target at a muon-collider source.

The best plan is to use the nominal geometrical parameters of the muon-collider target, *i.e.*, $r_0 = 1$ cm, $L \approx 30$ cm. Then for a candidate liquid of density $\rho = 10$ g/cm^2, the deposited energy should be $Q_0 \approx 30$ kJ. Deposition of energy Q_0 via the exploding-wire technique requires that the energy of the capacitor bank, $Q_{\rm bank}$ be of order $3Q_0 \approx 100$ kJ. The hydrodynamic time is $\tau_r \approx 3$ μs, so the bank discharge time $\tau_{\rm bank}$ should be 1 μs or less.

Let us estimate the electrical parameters of the exploding-wire system. Suppose, for example, that the wire has radius $r_w = 1$ mm and is made of copper. Then its resistance is $R = \rho_w L/\pi r_w^2 = 1.7 \times 10^{-3}$ Ω for $L = 30$ cm, using resistivity $\rho_w = 1.7$ $\mu\Omega$-cm. The capacitance of the bank must then be $C = \tau_{\rm bank}/R \approx 600$ μF. The stored energy of the bank is $U = CV^2/2 \approx 3Q_0 \approx 10^5$ J, so the operating voltage is $V \approx 20$ kV. The peak discharge current is $I = V/R \approx 10$ MA. For a copper wire of radius 0.5 mm, the bank capacitance would be 150 μF, the voltage 40 kV and the peak current 5 MA.

The mass of the 1-mm-radius copper wire would be only about 8 g, so the energy density would be about 3,500 J/g, which will vaporize much of the wire.

Experiments are proposed be performed in three stages:

First Stage. In the first stage, an exploding-wire facility with the desired electrical parameters will be established, but for simplicity the wire will not be immersed in a liquid metal. Rather, a dielectric liquid such as a purified water or organic compound such as castor oil would be used. The physical processes of the shockwave formation and its influence on the stability of a vertical liquid jet would be studied. As well as establishing the experimental technique, the data will permit first elaboration and refinement of the physical models and computer codes.

Second Stage. In the second stage, experiments with candidate liquid metals will be performed. For this, the wire would be insulated from the conducting liquid by a film of a material with good dielectric properties such as, for example, Mylar with a thickness of a few μm. The shockwave crosses this film in a few ns, and existence of this thin film would not significantly influence the physical phenomena under study.

Third Stage. In this stage experiments from the second stage would be repeated in a strong magnetic field to study the effect of such field on jet stability during the heating of the jet.

Diagnostics. Diagnostics for the exploding-wire studies that exist at the Russian facilities include measurements for the electric parameters, pressure sensors to measure the shockwave parameters, and high-speed streak and frame cameras to monitor the liquid behavior during and after the wire explosion. The pressure sensors can be placed in the liquid jet at different distances without disturbing the flowing jet. Such diagnostics have been extensively used during high-energy deposition on target materials to simulate plasma disruption in future fusion reactors.

4 Appendix A: BNL E-910, Low-Momentum Pion Production

Inclusive pion cross sections in proton nucleus interactions are quite hard to calculate due to the contribution of many different processes and are best determined experimentally. Various event-generator codes used by the heavy-ion-physics community [19, 20, 22] to simulate the cascade inside the nucleus indicate a pronounced peak in pion production at low momenta. Unfortunately, there is very limited data in the literature for pion production at the low end of the spectrum (below 200 MeV/c). These data also are essential for calibrating the event generators for use in a realistic simulation of the muon-collider front end.

Since many aspects of the targetry and pion capture/phase rotation depend on the shape and magnitude of these spectra, the Muon Collider Collaboration has allocated some resources to obtain critical results on pion production by joining BNL experiment 910, which was capable of the necessary acceptance and statistics. By combining large acceptance with particle identification and high statistics, data from E910 have allowed a systematic study of proton-nucleus interactions as a function of the number of slow protons and pions produced, rapidity loss of the leading particle, total transverse-energy content, *etc.*

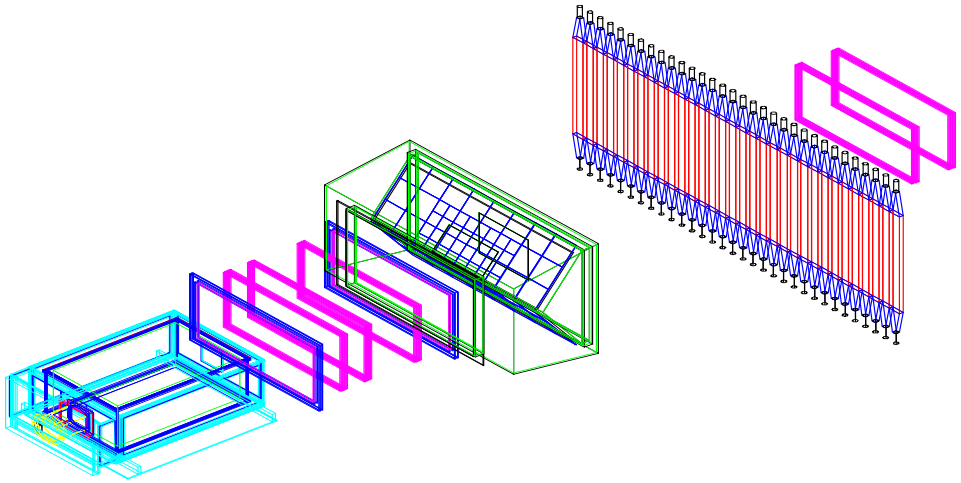

Figure 44: Major detectors in E910. The MPS magnet around the TPC has been omitted. The beam comes in from the left toward the target located in front of the TPC, which is followed by the Čerenkov and time-of-flight counters. The rectangular frames are wire chambers.

A simplified GEANT depiction of the E910 detector setup can be seen in Fig. 44. The main tracking detector was the EOS time projection chamber (TPC) placed inside the MPS magnet, downstream of the target to achieve almost full forward acceptance for charged tracks, an accurate determination of the vertex position using these tracks, and particle identification using ionization energy loss in the P-10 gas volume. The TPC was supplemented by proportional chambers placed upstream for incoming beam track reconstruction, as well as by drift chambers, a Čerenkov counter, and a time of flight wall located downstream for improved momentum resolution and particle id. A scintillating-fiber detector

behind the target was used as a multiplicity trigger for central collisions, and a scintillator beam veto behind the TPC defined minimum-bias events, including interactions that occur in the TPC gas.

Experiment 910 ran for 14 weeks in the A1 beamline at the AGS during Spring 1996 using a proton beam on a target placed in the MPS spectrometer, and collected over 20 million events, of which about a quarter are minimum bias triggers for inclusive cross section measurements. The targets were varied in material (Be, Cu, Au, U) and thickness (2-100% interaction length) and three different beam energies were used (6, 12.5 and 18 GeV/c). This was the first and only run of this experiment so far. Since then, the efforts of the E910 collaboration have focused on careful analysis of the large data sample obtained.

A typical event in the TPC is shown in Fig. 45, and Fig. 46 shows the charged multiplicity distribution in the TPC. Figure 47 shows the dE/dx energy loss *vs.* momentum for reconstructed tracks in the TPC, with clear separation of different particle species [136].

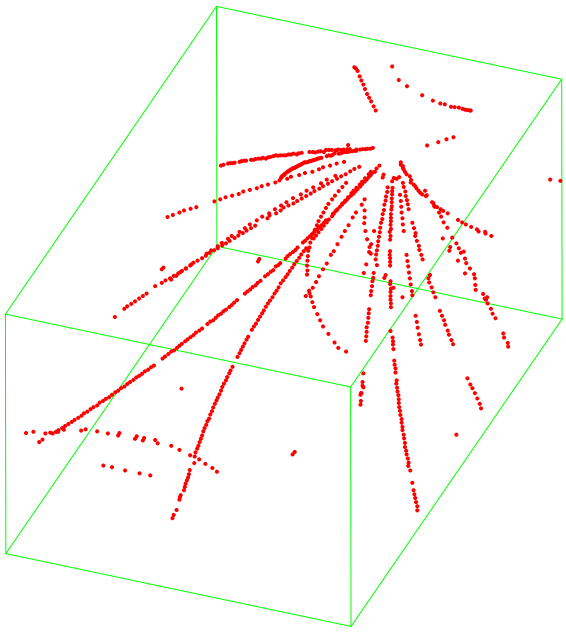

Figure 45: Downstream view of an interaction in the Au target located upstream of the TPC, showing hits reconstructed in the TPC.

An early tracking pass over a fraction of the data for preliminary physics insight has been performed in March-April 1997. Reliable tracking of particles down to 50 MeV/c has been accomplished in offline analysis. Approximate shapes for total and transverse momentum spectra for pions from this pass are shown in Figs. 48 and 49. A calibration pass was completed through August-October 1997, and a tracking pass over all the data using the calibration constants obtained. Many improvements in tracking are underway and should be complete in Fall 1998. The data processing effort is being carried out in parallel at many sites including BNL, Columbia, FSU, Iowa State, LLNL and ORNL.

An important aspect of the pion measurement in E910 is that the dE/dx sampling in the TPC is the only means of identification for particles below about 500 MeV/c, since these

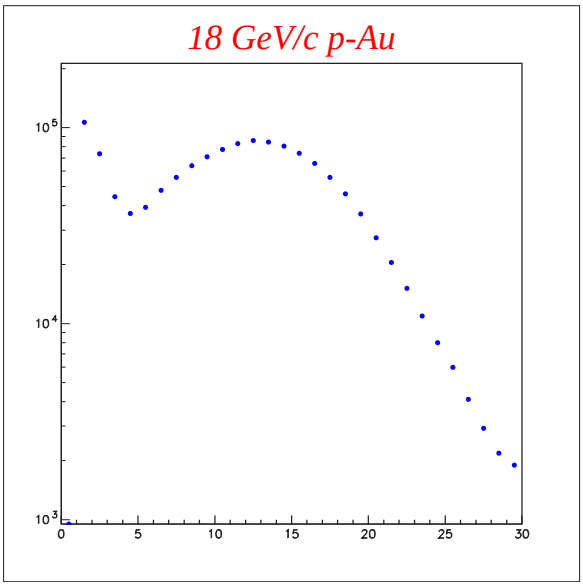

Figure 46: Charged-track multiplicity in the TPC from the 2-mm-thick Au target with a soft interaction trigger.

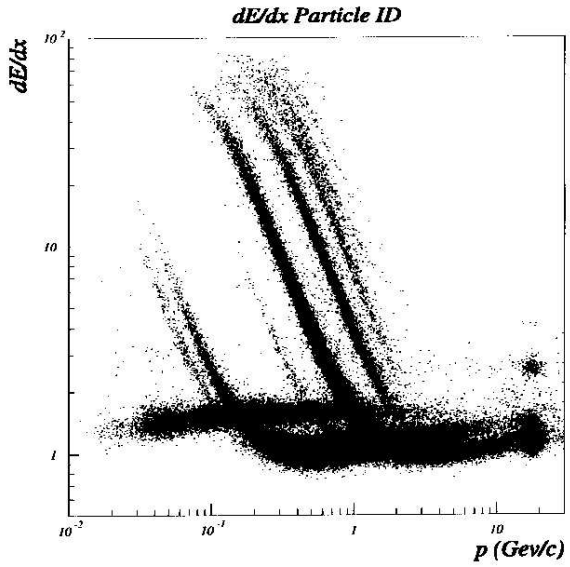

Figure 47: Ionization energy loss for tracks with 30 or more hits in the TPC. The beam momentum was 18 GeV/c.

particles either don't reach any detectors downstream of the TPC or their momentum is not high enough for particle id using time of flight or Čerenkov light. However, there is a large amount of overlap between the electron and muon/pion dE/dx bands around 100-200 MeV/c, as can be seen in Fig. 38 [136]. The electrons are produced mostly from photon conversions to e^+e^- pairs in the target, which has enough radiation lengths to make the

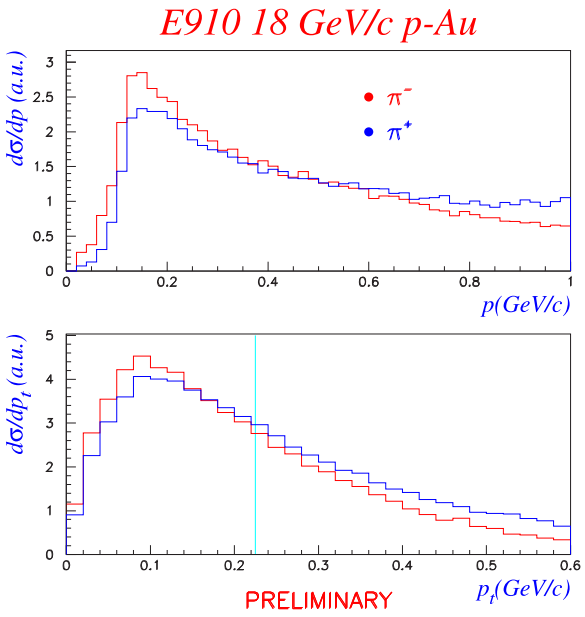

Figure 48: Forward pion spectrum for Au at 18 GeV/c. Particles to the left of the vertical line at 225 MeV/c would be captured by a 20-T, 15-cm-bore solenoid.

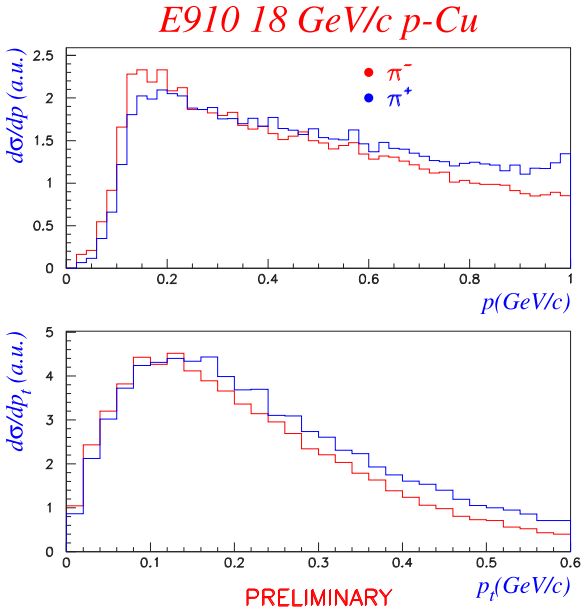

Figure 49: Forward pion spectrum for Cu at 18 GeV/c.

electron/pion ratio about one in this momentum region for the 2%-interaction-length Au target. Electrons can be identified in the TPC by reconstructing e^+e^- pairs.

The current tracking pass will produce better dE/dx resolution based on accurate TPC calibration, and will allow better separation of electrons and pions.

An important question in interpreting results and validating event generators is the size of the very slow, large-angle/backward component of the pion spectrum. This will be addressed with E910 events in which beam-gas interactions occurred in the TPC, allowing full 4π coverage for tracks produced in proton-Ar interactions. A typical beam-gas event is shown in Fig. 50.

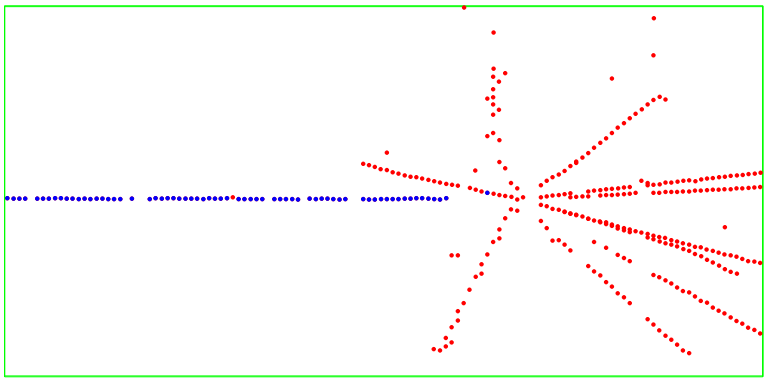

Figure 50: Side view of a beam-gas interaction in the TPC with complete coverage for backward tracks.

A publication on inclusive pion production based on E910 data is in preparation and will come out later this year. Comparison with event generators also is underway.

5 Appendix B: High Intensity Performance and Upgrades at the AGS

[This Appendix has been published separately as ref. [111].]

5.1 Recent AGS High Intensity Performance

Figure 51 shows the present layout of the AGS-RHIC accelerator complex. The high intensity proton beam of the AGS is used both for the slow-extracted-beam (SEB) area (with many target stations to produce secondary beams) and for the fast-extracted-beam (FEB) line (used for the production of muons for the $g-2$ experiment and for high intensity target testing for the spallation neutron sources and muon production targets for the muon collider). The same FEB line also will be used for the transfer of beam to RHIC.

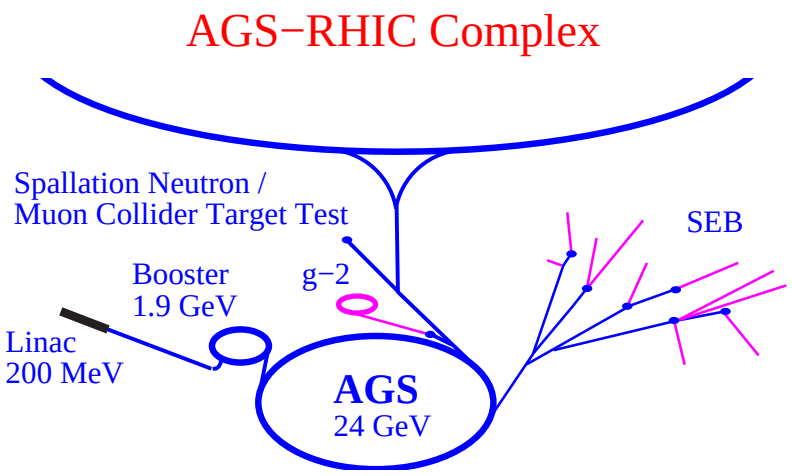

Figure 51: The AGS-RHIC accelerator complex.

The proton-beam intensity in the AGS has increased steadily over the 35-year existence of the AGS, but the most dramatic increase occurred over the last couple of years with the addition of the new AGS Booster [137, 138]. In Fig. 52 the history of the AGS intensity improvements is shown, and the major upgrades are indicated. The AGS Booster has one quarter the circumference of the AGS and therefore allows four Booster beam pulses to be stacked in the AGS at an injection energy of 1.5-1.9 GeV. At this increased energy, space-charge forces are much reduced, and this in turn allows for the dramatic increase in the AGS beam intensity.

The 200-MeV LINAC is being used both as the injector into the Booster and as an isotope production facility. A recent upgrade of the LINAC rf system made it possible to operate at an average H^- current of 150 μA and a maximum of 12×10^{13} H^- per 500-μs LINAC pulse for the isotope production target. Typical beam currents during the 500-μs pulse are

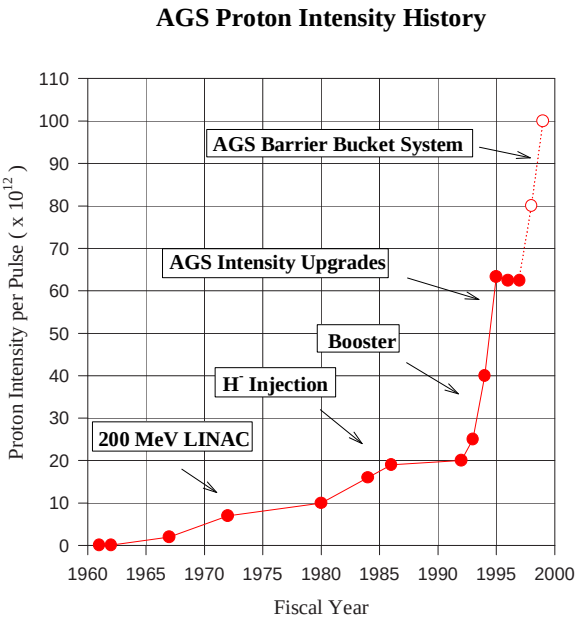

Figure 52: The evolution of the proton beam intensity in the Brookhaven AGS.

about 80 mA at the source, 60 mA after the 750-keV RFQ, 38 mA after the first LINAC tank (10 MeV), and 37 mA at the end of the LINAC at 200 MeV. The normalized beam emittance is about 2π mm-mrad for 95% of the beam, and the beam energy spread is about ± 1.2 MeV. A magnetic fast chopper installed at 750 keV allows the shaping of the beam injected into the Booster to avoid excessive beam loss.

The beam intensity achieved in the Booster surpassed the design goal of 1.5×10^{13} protons per pulse and reached a peak value of 2.3×10^{13} protons per pulse. This was achieved by very carefully correcting all the important nonlinear orbit resonances, especially at the injection energy of 200 MeV, and by using the extra set of rf cavities that was installed for heavy-ion operation as a second-harmonic rf system. The latter allows for the creation of a flattened rf bucket, which gives longer bunches with lower space-charge forces. The fundamental rf system operated with 90 kV, and the second-harmonic with 30 kV. The typical bunch area was about 1.5 eV-s. Even with the second-harmonic rf system the incoherent space-charge tune shift can reach one unit right at injection (3×10^{13} protons, norm. 95% emittance: 50π mm-mrad, bunching factor: 0.5). Of course, such a large tune shift is not sustainable, but the beam emittance growth and beam loss can be minimized by accelerating rapidly during and after injection. Best conditions are achieved by ramping the main field during injection with 3 T/s increasing to 9 T/s after about 10 ms. The quite-large nonlinear fields from eddy currents in the Iconel vacuum chamber of the Booster are passively corrected using correction windings on the vacuum chamber that are driven by backleg windings [139].

The AGS itself also had to be upgraded to be able to cope with the higher beam intensity. During beam injection from the Booster, which cycles with a repetition rate of 7.5 Hz, the AGS needs to store the already transferred beam bunches for about 0.4 s. During this time the beam is exposed to the strong image forces from the vacuum chamber, which cause beam loss from resistive-wall-coupled bunch-beam instabilities within as short a time as a

few-hundred revolutions. A very powerful feedback system was installed that senses any transverse movement of the beam and compensates with a correcting kick. This transverse damper can deliver ±160 V to a pair of 50-Ω, 1-m-long striplines. A recursive digital notch filter is used in the feedback circuit to allow for accurate determination of the average beam position and increased sensitivity to the unstable coherent beam motion. This filter design is particularly important for the betatron tune setting of about 8.9, which is required to avoid the nonlinear octupole stopband resonance at 8.75. With an incoherent tune shift at the AGS injection energy of 0.1 to 0.2 it is still necessary, however, to correct the octupole stopband resonances to avoid excessive beam loss.

To reduce the space-charge forces further, the beam bunches in the AGS are lengthened by purposely mismatching the bunch-to-bucket transfer from the Booster and then smoothing the bunch distribution using a high-frequency 100-MHz dilution cavity. The resulting reduction of the peak current helps both with coupled bunch instabilities and stopband beam losses.

During acceleration, the AGS beam has to pass through the transition energy after which the revolution time of higher-energy protons becomes longer than for the lower-energy protons. This potentially unstable point during the acceleration cycle was crossed very quickly with a new powerful transition-energy-jump system with only minimal losses even at the highest intensities. The large lattice distortions introduced by the jump system prior to the transition crossing severely limits the available aperture of the AGS, in particular for momentum spread. Efforts to correct the distortions using sextupoles have been partially successful [140]. After the transition energy, a very rapid, high-frequency instability developed which could be avoided only by purposely further increasing the bunch length using again the high-frequency dilution cavity.

The peak beam intensity reached at the AGS extraction energy of 24 GeV was 6.3×10^{13} protons per pulse, also exceeding the design goal for this latest round of intensity upgrades. It also represents a world record beam intensity for a proton synchrotron. With a 1.6-s slow-extracted-beam spill, the average extracted beam current was about 3 μA. This level of performance was reached quite consistently over the last few years, and during a typical 20 week run a total of 1×10^{20} protons is accelerated in the AGS to the extraction energy of 24 GeV.

At maximum beam intensity, about 30% of the beam is lost at Booster injection (200 MeV), 25% during the transfer from Booster to AGS (1.5 GeV), which includes losses during the 0.4-s storage time in the AGS, and about 3% is lost at transition (8 GeV). Although activation levels are quite high, all machines still can be manually maintained and repaired in a safe manner.

5.2 Possible Future AGS Intensity Upgrades

Currently the number of Booster beam pulses that can be accumulated in the AGS is limited to four by the fact that the circumference of the AGS is four times the circumference of the Booster. This limits the maximum beam intensity in the AGS to four times the maximum Booster intensity, which itself is limited to 2.5×10^{13} protons per pulse by the space-charge forces at Booster injection. To overcome this limitation, some sort of stacking will have to be used in the AGS. The most promising scheme is stacking in the time domain. To accomplish

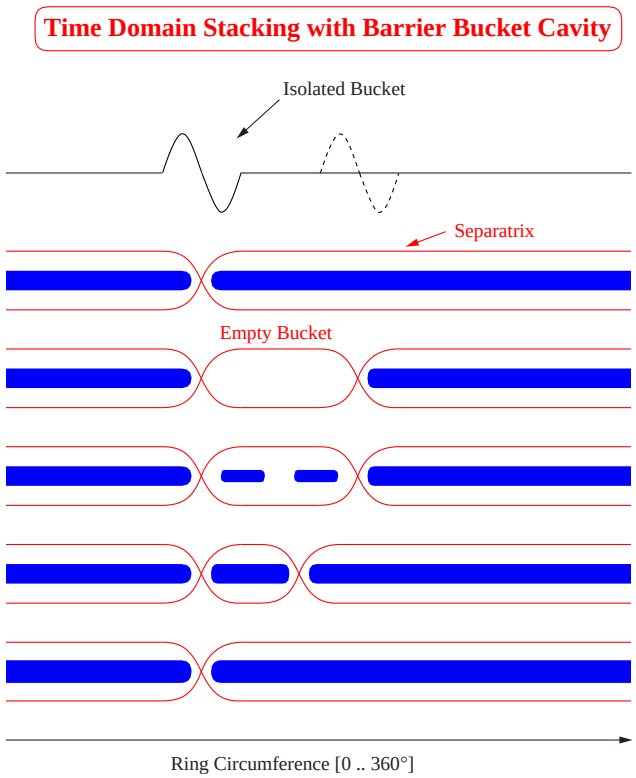

Figure 53: Time-domain-stacking scheme using a barrier-bucket cavity. The evolution of the longitudinal beam structure during the stacking process is shown from top to bottom.

this, a cavity that produces isolated rf buckets can be used to maintain a partially debunched beam in the AGS and still leave an empty gap for filling in additional Booster beam pulses. The stacking scheme is illustrated in Fig. 53. It makes use of two isolated rf buckets to control the width of this gap. Isolated bucket cavities, also called Barrier Bucket cavities, have been used elsewhere [141]. However, for this stacking scheme, a high rf voltage will be needed to contain the large bunch area of the high-intensity beam. An additional important advantage of this scheme is that while the beam is partially debunched in the AGS, the beam density and therefore space-charge forces are reduced by up to a factor of two. A successful test of this scheme has recently been completed [142], and two 40-kV Barrier cavities are being installed in the AGS with the aim of accumulating six Booster beam pulses in the AGS to reach an intensity of about 1×10^{14} protons per pulse.

For further increases in the intensity, the space-charge forces at Booster injection represent the main limitation. This could be overcome by an energy upgrade of the LINAC to about 600 MeV, replacing some of the present 200-MHz cavities with higher-gradient 400-MHz cavities driven by klystrons. At 600 MeV, the space-charge limit at Booster injection would be 5×10^{13} protons per pulse or 2×10^{14} protons in the AGS for 4 cycles per AGS cycle.

As more Booster beam pulses are accumulated in the AGS, the reduction in the overall duty cycle becomes more significant. For fast-extracted-beam operation (FEB) the accumu-

lation of four Booster pulses already contributes significantly to the overall cycle time. With the addition of a 2-GeV accumulator ring in the AGS tunnel, this overhead time could be completely avoided. Such a ring could be built rather inexpensively using low-field magnets. The maximum repetition rate of the Linac and Booster is 10 Hz. Since the circumference of the AGS is four times that of the Booster, a repetition rate of 2.5 Hz would maintain a throughput of 80 μA through the whole accelerator chain. Such an increase of the AGS repetition rate by a factor of 2.5 could be achieved by an upgrade of the AGS main magnet power supply only. The resulting beam power of 2 MW at 25 GeV corresponds to the required proton driver performance needed for a demonstration muon-collider project. The upgrades to the AGS complex are summarized in Fig. 54.

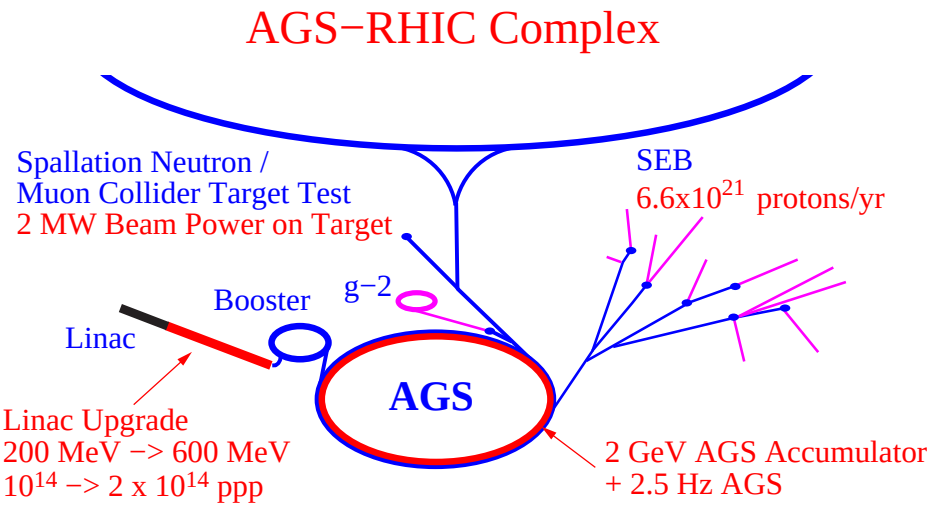

Figure 54: Summary of intensity upgrades for the AGS.

6 Appendix C: Personnel, Schedule, Budget

The institutional involvement in the 8 phases of the R&D program is listed in Table 11. A GANTT chart of the program at the level of 100 subtopics is presented on the following two pages. A cost summary derived from the GANTT chart follows these, based on a four-year program with funding roughly \$1, \$2, \$3 and \$1M for the four years, respectively.

Table 11: Participation by institution in the 8 phases of the proposed R&D program. The lead institution for each phase is shown in **boldface**.

Topic	Institutions
1. Initial Tests	BNL, CERN, ORNL, **Princeton**
2. Liquid jet + 20-T magnet	BNL, **Princeton**, NHMFL
3. Full-scale jet, 10^{14} $p$pp	ANL, **BNL**, CERN, Princeton
4. Full-scale jet + pulsed 20-T magnet	ANL, **BNL**, CERN, Princeton
5. RF cavity + short beam pulse	**BNL**, CERN, Fermilab, LBL, Princeton
6. RF cavity + 1.25-T magnet	**BNL**, LBL, Princeton
7. Pion-production measurement	**BNL**, Fermilab, LBL, Princeton
8. Simulation + exploding wire tests	**ANL**, BNL, Fermilab, ORNL, Princeton

ID	Task Name	Duration	Cost	Start	Finish
1	**Targetry R&D**	**1040 days**	**$7,110,000**	**Fri 1/1/99**	**Thu 12/26/02**
2	**Liquid Metal I**	**100 days**	**$130,000**	**Fri 1/1/99**	**Thu 5/20/99**
3	**Initial Beam Test**	**55 days**	**$80,000**	**Fri 1/1/99**	**Thu 3/18/99**
4	Containment Vessel	30 days	$30,000	Fri 1/1/99	Thu 2/11/99
5	Instrumentation	45 days	$40,000	Fri 1/1/99	Thu 3/4/99
6	Test at AGS, I	10 days	$10,000	Fri 3/5/99	Thu 3/18/99
7	**3 mm Jet Test**	**100 days**	**$50,000**	**Fri 1/1/99**	**Thu 5/20/99**
8	Jet fabricaton	90 days	$20,000	Fri 1/1/99	Thu 5/6/99
9	Containment Vessel	20 days	$10,000	Tue 2/9/99	Mon 3/8/99
10	Instrumentation	20 days	$10,000	Tue 3/9/99	Mon 4/5/99
11	Test at AGS, II	10 days	$10,000	Fri 5/7/99	Thu 5/20/99
12	**Jet Test at FSU Magnet**	**50 days**	**$60,000**	**Mon 4/5/99**	**Fri 6/11/99**
13	Containment Vessel	20 days	$20,000	Mon 4/5/99	Fri 4/30/99
14	Instrumentation	20 days	$20,000	Mon 5/3/99	Fri 5/28/99
15	Test at FSU	10 days	$20,000	Mon 5/31/99	Fri 6/11/99
16	**2 cm Jet, 1e14 p's**	**530 days**	**$600,000**	**Fri 1/1/99**	**Thu 1/11/01**
17	**2 cm Jet**	**100 days**	**$90,000**	**Mon 5/3/99**	**Fri 9/17/99**
18	Design	60 days	$20,000	Mon 5/3/99	Fri 7/23/99
19	Jet Fabrication	45 days	$20,000	Mon 6/28/99	Fri 8/27/99
20	Containment Vessel	30 days	$20,000	Mon 7/26/99	Fri 9/3/99
21	Instrumentation	20 days	$20,000	Mon 7/26/99	Fri 8/20/99
22	Test at AGS, III	10 days	$10,000	Mon 9/6/99	Fri 9/17/99
23	**1e14 ppp**	**530 days**	**$510,000**	**Fri 1/1/99**	**Thu 1/11/01**
24	AGS Extraction Upgr	520 days	$500,000	Fri 1/1/99	Thu 12/28/00
25	Test at AGS, IV	10 days	$10,000	Fri 12/29/00	Thu 1/11/01
26	**Pulsed Solenoid**	**550 days**	**$1,020,000**	**Fri 10/1/99**	**Thu 11/8/01**
27	Design	200 days	$100,000	Fri 10/1/99	Thu 7/6/00
28	Coil Purchase/Fabrication	250 days	$500,000	Fri 7/7/00	Thu 6/21/01
29	Commisioning	60 days	$100,000	Fri 6/22/01	Thu 9/13/01
30	LN2 Cryostat Design	7 days	$50,000	Fri 7/7/00	Mon 7/17/00
31	LN2 Cryostat Fabrication	50 days	$100,000	Tue 7/18/00	Mon 9/25/00
32	LN2 Handling	40 days	$20,000	Tue 9/26/00	Mon 11/20/00
33	Move/Refurbish PS	40 days	$40,000	Wed 10/4/00	Tue 11/28/00
34	Move Substation	40 days	$40,000	Wed 11/29/00	Tue 1/23/01
35	Substation Attachment	20 days	$20,000	Wed 1/24/01	Tue 2/20/01
36	Switching System	45 days	$30,000	Wed 2/21/01	Tue 4/24/01
37	Test at AGS, V	40 days	$20,000	Fri 9/14/01	Thu 11/8/01
38	**RF Systems**	**680 days**	**$1,650,000**	**Fri 10/1/99**	**Thu 5/9/02**
39	**RF Cavity**	**680 days**	**$950,000**	**Fri 10/1/99**	**Thu 5/9/02**
40	Design	260 days	$120,000	Fri 10/1/99	Thu 9/28/00
41	Purchase/Fabricate	260 days	$600,000	Fri 9/29/00	Thu 9/27/01
42	Assembly	20 days	$20,000	Fri 9/28/01	Thu 10/25/01
43	Testing w/o beam	60 days	$30,000	Fri 10/26/01	Thu 1/17/02
44	Refurbish/rebuild	20 days	$150,000	Fri 1/18/02	Thu 2/14/02
45	Test at AGS, VI	60 days	$30,000	Fri 2/15/02	Thu 5/9/02
46	**Site Preparation**	**254 days**	**$300,000**	**Tue 8/1/00**	**Fri 7/20/01**
47	Design	30 days	$30,000	Tue 8/1/00	Mon 9/11/00
48	Blockhouse	60 days	$150,000	Tue 9/12/00	Mon 12/4/00
49	Shielding	60 days	$30,000	Tue 12/5/00	Mon 2/26/01
50	Power Service	70 days	$20,000	Wed 2/28/01	Tue 6/5/01
51	Vacuum	120 days	$50,000	Mon 2/5/01	Fri 7/20/01
52	DI Water	45 days	$20,000	Tue 5/1/01	Mon 7/2/01
53	**LBL Transfer**	**50 days**	**$50,000**	**Fri 10/1/99**	**Thu 12/9/99**
54	Testing	40 days	$40,000	Fri 10/1/99	Thu 11/25/99
55	Packing	5 days	$5,000	Fri 11/26/99	Thu 12/2/99
56	Shipping	5 days	$5,000	Fri 12/3/99	Thu 12/9/99
57	**Low Level RF**	**105 days**	**$40,000**	**Wed 4/5/00**	**Tue 8/29/00**

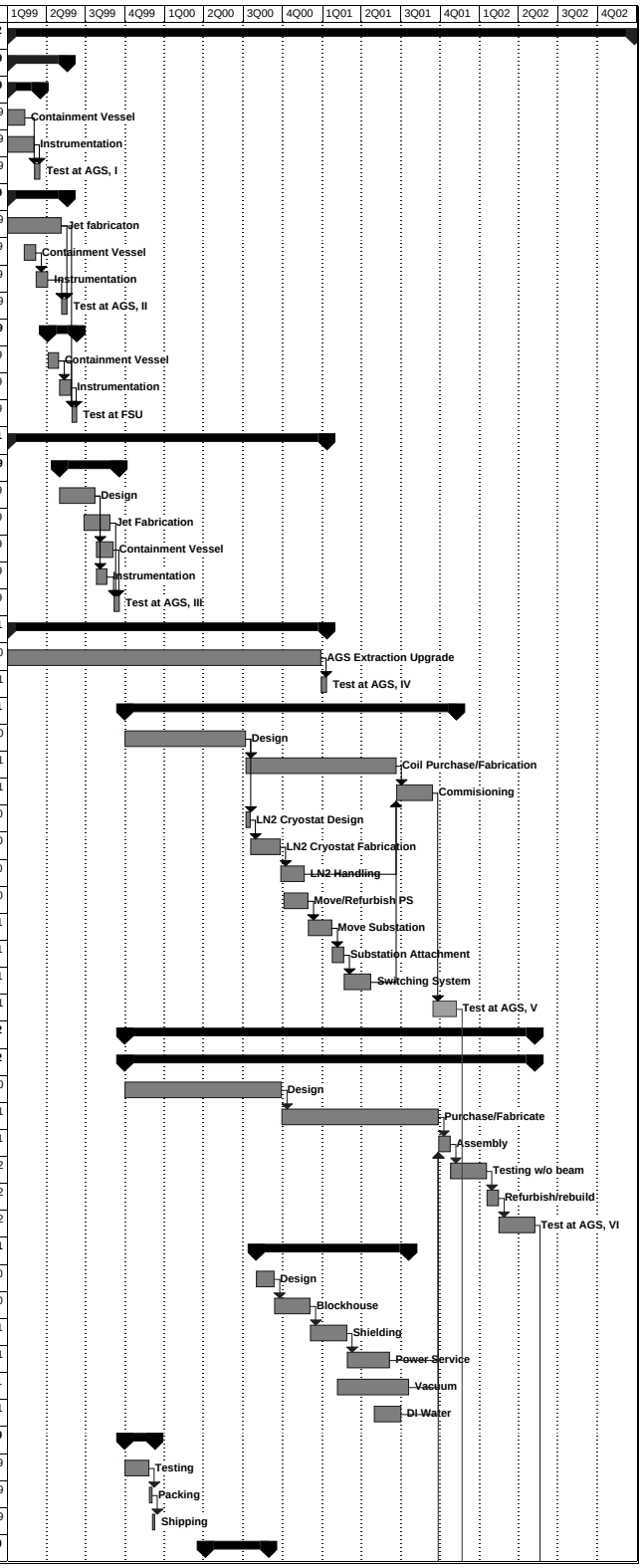

ID	Task Name	Duration	Cost	Start	Finish
58	Design	30 days	$10,000	Wed 4/5/00	Tue 5/16/00
59	Procurement	45 days	$20,000	Wed 5/17/00	Tue 7/18/00
60	Testing	30 days	$10,000	Wed 7/19/00	Tue 8/29/00
61	**Pulsing System**	**200 days**	**$110,000**	**Thu 8/3/00**	**Wed 5/9/01**
62	Design	60 days	$30,000	Thu 8/3/00	Wed 10/25/00
63	Procurement	60 days	$30,000	Thu 10/26/00	Wed 1/17/01
64	Crowbar	60 days	$30,000	Thu 1/18/01	Wed 4/11/01
65	Testing	20 days	$20,000	Thu 4/12/01	Wed 5/9/01
66	**Power Combiner**	**150 days**	**$200,000**	**Wed 1/3/01**	**Tue 7/31/01**
67	Design	60 days	$80,000	Wed 1/3/01	Tue 3/27/01
68	Procurement	60 days	$100,000	Wed 3/28/01	Tue 6/19/01
69	Testing	30 days	$20,000	Wed 6/20/01	Tue 7/31/01
70	**RF Solenoid**	**529 days**	**$1,110,000**	**Mon 8/7/00**	**Thu 8/15/02**
71	Coil Design	120 days	$60,000	Mon 8/7/00	Fri 1/19/01
72	Coil Fabricate	300 days	$500,000	Mon 1/22/01	Fri 3/15/02
73	Iron Design	120 days	$60,000	Mon 1/22/01	Fri 7/6/01
74	Iron Fabricate	150 days	$200,000	Mon 7/9/01	Fri 2/1/02
75	Support Design	80 days	$40,000	Mon 7/9/01	Fri 10/26/01
76	Support Fabricate	100 days	$50,000	Mon 10/29/01	Fri 3/15/02
77	Block House	80 days	$20,000	Mon 6/4/01	Fri 9/21/01
78	Move/Refurbish PS	60 days	$30,000	Mon 9/24/01	Fri 12/14/01
79	Substation Attachment	20 days	$20,000	Mon 12/17/01	Fri 1/11/02
80	Commsioning	60 days	$120,000	Fri 5/10/02	Thu 8/1/02
81	Test at AGS, VII	10 days	$10,000	Fri 8/2/02	Thu 8/15/02
82	**Capture Experiment**	**634 days**	**$1,770,000**	**Mon 7/3/00**	**Thu 12/5/02**
83	Bent Solenoid Design	60 days	$30,000	Tue 2/6/01	Mon 4/30/01
84	Bent Solenoid Fabrication	300 days	$500,000	Tue 5/1/01	Mon 6/24/02
85	Guide Dipole Design	30 days	$20,000	Tue 5/1/01	Mon 6/11/01
86	Guide Dipole Fabrication	180 days	$150,000	Tue 6/12/01	Mon 2/18/02
87	Transition Magnet Design	30 days	$20,000	Tue 6/12/01	Mon 7/23/01
88	Transition Magnet fabricat	120 days	$100,000	Tue 7/24/01	Mon 1/7/02
89	Power Suplies	90 days	$100,000	Wed 1/2/02	Tue 5/7/02
90	TPC system	500 days	$240,000	Wed 7/5/00	Tue 6/4/02
91	TOF System	500 days	$120,000	Wed 7/5/00	Tue 6/4/02
92	PWCs and scintillators	500 days	$150,000	Mon 7/3/00	Fri 5/31/02
93	Electronics and DAQData	500 days	$200,000	Tue 7/4/00	Mon 6/3/02
94	Counting Trailer	60 days	$60,000	Thu 1/3/02	Wed 3/27/02
95	Commisioning	50 days	$50,000	Fri 8/16/02	Thu 10/24/02
96	Test at AGS, VIII	30 days	$30,000	Fri 10/25/02	Thu 12/5/02
97	**Simulation & Validation**	**1040 days**	**$770,000**	**Fri 1/1/99**	**Thu 12/26/02**
98	Simulation	1040 days	$600,000	Fri 1/1/99	Thu 12/26/02
99	**Exploding Wire I**	**200 days**	**$110,000**	**Mon 1/3/00**	**Fri 10/6/00**
100	Capacitor Bank	120 days	$60,000	Mon 1/3/00	Fri 6/16/00
101	Test Cell, Water	20 days	$10,000	Mon 6/19/00	Fri 7/14/00
102	Instrumentation	30 days	$30,000	Mon 7/17/00	Fri 8/25/00
103	Data Collection	30 days	$10,000	Mon 8/28/00	Fri 10/6/00
104	**Exploding Wire II**	**210 days**	**$40,000**	**Mon 10/9/00**	**Fri 7/27/01**
105	Test Cell, Liquid Meta	30 days	$10,000	Mon 10/9/00	Fri 11/17/00
106	Data Collection	180 days	$30,000	Mon 11/20/00	Fri 7/27/01
107	**Exploding Wire III**	**60 days**	**$20,000**	**Wed 10/3/01**	**Tue 12/25/01**
108	Test Cell in Magnet	30 days	$10,000	Wed 10/3/01	Tue 11/13/01
109	Data Collection	30 days	$10,000	Wed 11/14/01	Tue 12/25/01

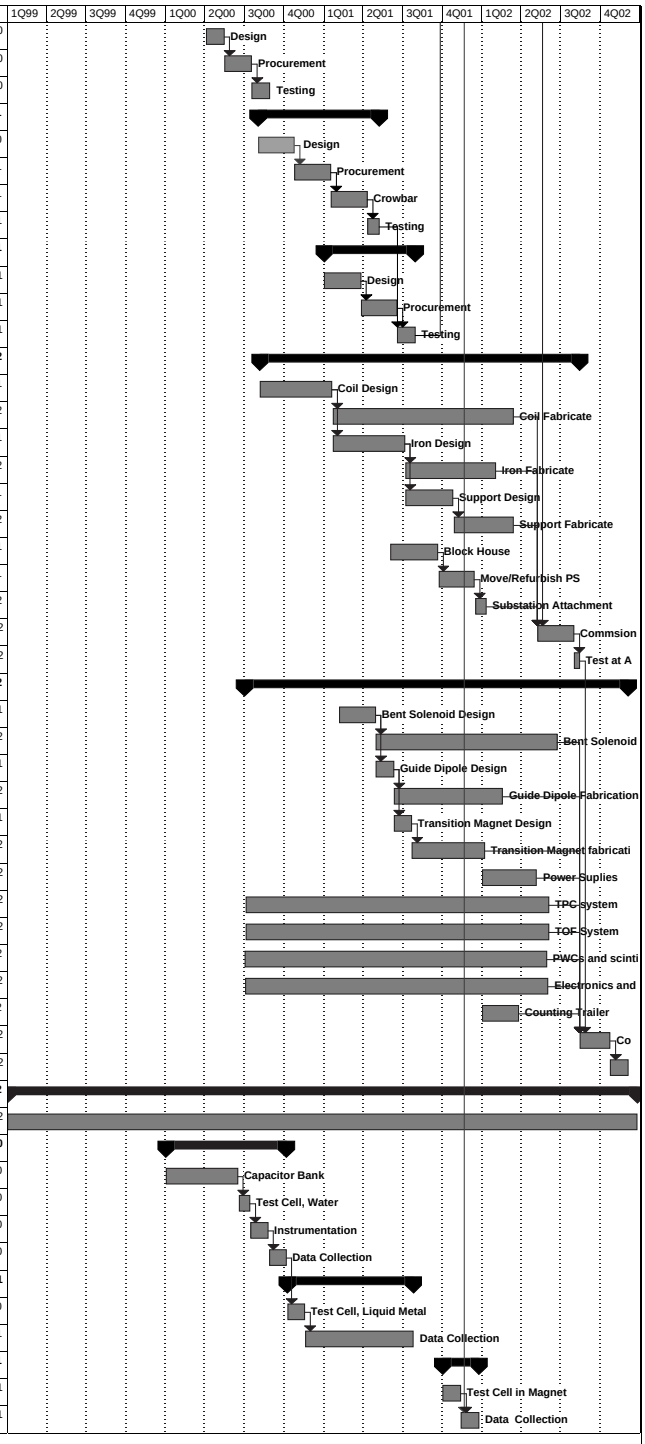

	1999	2000	2001	2002	Total
Targetry R&D					
Liquid Metal I					
Initial Beam Test					
Containment Vessel	$30,000				$30,000
Instrumentation	$40,000				$40,000
Test at AGS, I	$10,000				$10,000
3 mm Jet Test					
Jet fabricaton	$20,000				$20,000
Containment Vessel	$10,000				$10,000
Instrumentation	$10,000				$10,000
Test at AGS, II	$10,000				$10,000
Jet Test at FSU Magnet					
Containment Vessel	$20,000				$20,000
Instrumentation	$20,000				$20,000
Test at FSU	$20,000				$20,000
2 cm Jet, 1e14 p's					
2 cm Jet					
Design	$20,000				$20,000
Jet Fabrication	$20,000				$20,000
Containment Vessel	$20,000				$20,000
Instrumentation	$20,000				$20,000
Test at AGS, III	$10,000				$10,000
1e14 ppp					
AGS Extraction Upgrade	$250,962	$249,039			$500,000
Test at AGS, IV		$1,000	$9,000		$10,000
Pulsed Solenoid					
Design	$33,000	$67,000			$100,000
Coil Purchase/Fabrication		$252,000	$248,000		$500,000
Commisioning			$100,000		$100,000
LN2 Cryostat Design		$50,000			$50,000
LN2 Cryostat Fabrication		$100,000			$100,000
LN2 Handling		$20,000			$20,000
Move/Refurbish PS		$40,000			$40,000
Move Substation		$23,000	$17,000		$40,000
Substation Attachment			$20,000		$20,000
Switching System			$30,000		$30,000
Test at AGS, V			$20,000		$20,000
RF Systems					
RF Cavity					
Design	$30,462	$89,539			$120,000
Purchase/Fabricate		$152,308	$447,692		$600,000
Assembly			$20,000		$20,000
Testing w/o beam			$23,500	$6,500	$30,000
Refurbish/rebuild				$150,000	$150,000
Test at AGS, VI				$30,000	$30,000
Site Preparation					
Design		$30,000			$30,000
Blockhouse		$150,000			$150,000
Shielding		$9,500	$20,500		$30,000
Power Service			$20,000		$20,000
Vacuum			$50,000		$50,000
DI Water			$20,000		$20,000
LBL Transfer					
Testing	$40,000				$40,000
Packing	$5,000				$5,000
Shipping	$5,000				$5,000
Low Level RF					
Design		$10,000			$10,000
Procurement		$20,000			$20,000
Testing		$10,000			$10,000
Pulsing System					
Design		$30,000			$30,000
Procurement		$77,125	($47,125)		$30,000
Crowbar			$30,000		$30,000
Testing			$20,000		$20,000
Power Combiner					
Design			$80,000		$80,000
Procurement			$100,000		$100,000
Testing			$20,000		$20,000
RF Solenoid					
Coil Design		$52,500	$7,500		$60,000
Coil Fabricate			$410,000	$90,000	$500,000
Iron Design			$60,000		$60,000
Iron Fabricate			$168,000	$32,000	$200,000
Support Design			$40,000		$40,000
Support Fabricate			$23,000	$27,000	$50,000
Block House			$20,000		$20,000
Move/Refurbish PS			$30,000		$30,000
Substation Attachment			$11,000	$9,000	$20,000
Commsioning				$120,000	$120,000
Test at AGS, VII				$10,000	$10,000
Capture Experiment					
Bent Solenoid Design			$30,000		$30,000
Bent Solenoid Fabrication			$291,667	$208,333	$500,000
Guide Dipole Design			$20,000		$20,000
Guide Dipole Fabrication			$120,833	$29,167	$150,000
Transition Magnet Design			$20,000		$20,000
Transition Magnet fabrication			$95,833	$4,167	$100,000
Power Suplies				$100,000	$100,000
TPC system		$61,440	$125,280	$53,280	$240,000
TOF System		$30,720	$62,640	$26,640	$120,000
PWCs and scintillators		$39,000	$78,300	$32,700	$150,000
Electronics and DAQData acquisition		$200,000			$200,000
Counting Trailer				$60,000	$60,000
Commisioning				$50,000	$50,000
Test at AGS, VIII				$30,000	$30,000
Simulation & Validation					
Simulation	$150,577	$150,000	$150,577	$148,846	$600,000
Exploding Wire I					
Capacitor Bank		$60,000			$60,000
Test Cell, Water		$10,000			$10,000
Instrumentation		$30,000			$30,000
Data Collection		$10,000			$10,000
Exploding Wire II					
Test Cell, Liquid Metal		$10,000			$10,000
Data Collection		$5,000	$25,000		$30,000
Exploding Wire III					
Test Cell in Magnet			$10,000		$10,000
Data Collection			$10,000		$10,000
Total	$795,000	$2,039,170	$3,058,198	$1,217,633	$7,110,000

7 References

[1] C.M. Ankenbrandt *et al.*, *Status of Muon Collider Research and Development and Future Plans*, submitted to Phys. Rev. Sp. Top. – Acc. Beams;
http://www.cap.bnl.gov/mumu/status_report.html

[2] The $\mu^+\mu^-$ Collider Collaboration, *$\mu^+\mu^-$ Collider Feasibility Study*, BNL-52503, FERMILAB-Conf-96/092, LBNL-38946 (July 1996);
http://www.cap.bnl.gov/mumu/book.html

[3] G.K. O'Neill, *Storage-Ring Synchrotron: Device for High-Energy Physics Research*, Phys. Rev. **102**, 1418 (1956);
http://puhep1.princeton.edu/mumu/physics/oneill/1.html

[4] G.I. Budker, *Accelerators and Colliding Beams* (in Russian), in *Proc. 7^{th} Int. Conf. on High Energy Accel.* (Yerevan, 1969), p. 33; extract: AIP Conf. Proc. **352**, 4 (1996).

[5] G.I. Budker, Int. High Energy Conf. (Kiev, 1970), unpublished; extract: AIP Conf. Proc. **352**, 4 (1996).

[6] A.N. Skrinsky, *Intersecting Storage Rings at Novosibirsk*, Proc. Int. Seminar on Prospects of High-Energy Physics (Morges, Mar. 1971), unpublished; extract: AIP Conf. Proc. **352**, 6 (1996).

[7] D. Neuffer, *Multi-TeV Muon Colliders*, AIP Conf. Proc. **156**, 201 (1987);
http://www-ppd.fnal.gov/muscan/munotes/mc-006.pdf

[8] S. Geer and R. Raja (eds.), *Workshop on Physics at the First Muon Collider and at the Front End of the Muon Collider*, (Fermilab, Nov. 1997), AIP Conf. Proc. **435** (1998);
http://www.fnal.gov/projects/muon_collider/physics/talks.html

[9] D.B. Lichtenberg, P. Stehle and K.R. Symon, *Modification of Liouville's Theorem Required by the Presence of Dissipative Forces*, MURA Report 126 (July 12, 1956);
http://puhep1.princeton.edu/mumu/physics/symon/1.html

[10] A.A. Kolomensky, *On the Oscillation Decrements in Accelerators in the Presence of Arbitrary Energy Losses*, Sov. Atomic Energy **19**, 1511 (1965);
http://puhep1.princeton.edu/mumu/physics/kolomensky/1.html

[11] Yu.M. Ado and V.I. Balbekov, *Use of Ionization Friction in the Storage of Heavy Particles*, Sov. Atomic Energy **31**, 731 (1971);
http://puhep1.princeton.edu/mumu/physics/ado/1.html

[12] D. Cline and D. Neuffer, *A Muon Storage Ring for Neutrino Oscillation Experiments*, AIP Conf. Proc. **68**, 846 (1980); reproduced in AIP Conf. Proc. **352**, 10 (1996);

[13] The main Web page of the Muon Collider Collaboration is at
http://www.cap.bnl.gov/mumu/mu_home_page.html

[14] The MUCOOL Collaboration, *Ionization Cooling Research and Development Program for a High Luminosity Muon Collider*, FNALl-P904 (April 15, 1998);
http://www.fnal.gov/projects/muon_collider/

[15] N.V. Mokhov R. Noble and A. Van Ginneken, *Target and Collection Optimization for Muon Colliders*, AIP Conf. Proc. **372**, 61 (1996);
http://www-lib.fnal.gov/archive/1996/conf/Conf-96-006.html

[16] D. Ehst, N.V. Mokhov, R.J. Noble and A. Van Ginneken, *Target Options and Yields for a Muon Collider Source*, Proc. PAC97 (Vancouver, 1997), p. 393;
http://www.triumf.ca/pac97/papers/pdf/4W023.PDF

[17] H. Takahashi, Y. An, X. Chen and M. Nomura, *Optimization of the Target for Muon Colliders*, Proc. PAC97 (Vancouver, 1997), p. 402;
http://www.triumf.ca/pac97/papers/pdf/4W027.PDF

[18] N.V. Mokhov and A. Van Ginneken, *Pion Production and Targetry at $\mu^+\mu^-$ Colliders*, AIP Conf. Proc. **441**, 320 (1998);
http://www-ap.fnal.gov/~mokhov/papers/1998/Fermilab-Conf-98-41.ps

[19] S.H. Kahana, Y. Pang and T.J. Schlagel, in *Proceedings of Heavy Ion Physics at the AGS-HIPAGS '93*, eds. G.S. Stephans, S.G. Steadman and W.E. Kehoe; D. Kahana and Y. Torun, *Analysis of Pion Production Data from E-802 at 14.6 GeV/c Using ARC*, BNL-61983 (July 1995); see also
http://bnlnth.phy.bnl.gov/arc/arc.html

[20] N.V. Mokhov, *The MARS Code System Users Guide*, Fermilab-FN-628 (1995);
http://www-ap.fnal.gov/MARS/

[21] N.V. Mokhov and S.I. Striganov, *Model for Pion Production in Proton-Nucleus Interactions*, FERMILAB-Conf-98/053 (Feb. 5, 1998);
http://www-lib.fnal.gov/archive/1998/conf/Conf-98-053.html

[22] J. Ranft, *DPMJET version II.3 and II.4*, INFN-AE-97-45 (1997);
http://preprints.cern.ch/cgi-bin/setlink?base=preprint&categ=scan&id=SCAN-9711078.

[23] Experiment E-910 at BNL-AGS; http://www.nevis.columbia.edu/heavyion/e910/

[24] J. Lettry *et al.*, *Experience with ISOLDE Molten Metal Targets at the CERN-PS Booster*, in Proceedings of ICANS-XIII (1995);
http://puhep1.princeton.edu/mumu/target/

[25] G.I. Silvestrov, *Liquid Metal Jet Targets for Intense High Energy Beams*, Budker Institute preprint (Aug. 1998);
http://puhep1.princeton.edu/mumu/silvestrov/jet_silvestrov.pdf

[26] C. Johnson, *Solid and Liquid Targets Overview*, Proceeding of the Mini-Workshop: Target and Muon Collection Magnets and Accelerators, (Oxford, MS, 1997, unpublished);
http://nicewww.cern.ch/~cdj/public/mumutarg/

[27] Jack Carpenter, private communication (1996).

[28] C. Lu and K.T. McDonald, *Low-Melting-Temperature Metals for Possible Use as Primary Targets at a Muon Collider Source*, Princeton/$\mu\mu$/97-3 (1998);
http://puhep1.princeton.edu/mumu/mumu-97-3.ps

[29] R. Weggel, *Behavior of Conducting Solid or Liquid Jet Moving in Magnetic Field: 1) Paraxial, 2) Transverse, 3) Oblique*, CAP-220-MUON-98R (1998).

[30] J. Walker and W.H. Wells, *Drag Force on a Conducting Spherical Drop in a Nonuniform Magnetic Field*, ORNL/TN-6976 (Sept. 1979).

[31] C. Lu and K.T. McDonald, *Flowing Tungsten Powder for Possible Use as the Primary Target at a Muon Collider Source*, Princeton/$\mu\mu$/98-10 (Mar. 15, 1998); http://puhep1.princeton.edu/mumu/mumu-98-10.ps

[32] B.J. King, N.V. Mokhov and R. Weggel, *A Cu-Ni Rotating Band Target for Pion Production at Muon Colliders*, http://pubweb.bnl.gov/people/bking/target_aps98/index.html

[33] R. Weggel, *4-MW Hollow-Conductor Magnets for 20 T Hybrid Systems to Collect Pions for a Muon Collider*, BNL-Technical Report MU-015 (Jan. 1997).

[34] J.R. Miller *et al.*, IEEE Trans. Magnetics **30**, 1563 (1994).

[35] R.B. Palmer and J.C. Gallardo, *MC, Fortran program to simulate the front end and cooling section*, (unpublished).

[36] D. Neuffer and A. van Ginneken, private communication (1998).

[37] See p. 220 of ref. [2].

[38] Harold Kirk, private communication (1997).

[39] K. Assamagan *et al.*, *Measurement of the muon momentum in pion decay at rest using a surface muon beam*, Phys. Lett. **B335**, 231 (1994).

[40] B. Norum and R. Rossmanith, *Polarized beams in a muon collider*, Nucl. Phys. B (Proc. Suppl.) **51A**, 191 (1996).

[41] G.S. Bauer, *ESS Liquid Metal Target Studies*, ESS 95-33-T (Oct. 1995).

[42] G.S. Bauer, *Mercury as a Target Material for Pulsed (Fast) Spallation Neutron Sources*, ICANS-XIII, PSI-Proceedings 95-02 (Oct. 1995), p. 547.

[43] B.R. Appleton and G.S. Bauer, *Proc. Int. Workshop on the Technology and Thermal Hydraulics of Heavy Liquid Metals (Hg, Pb, Bi and Their Eutectics)*, (Schruns, Austria, Mar. 1996), ORNL CONF-9603171 (June 1996).

[44] T.A. Broome, *High Power Targets for Spallation Sources* Proc. EPAC96 (Sitges, Spain, 1996), p. 267; http://www.cern.ch/accelconf/e96/PAPERS/ORALS/TUY04A.PDF

[45] T.A. Gabriel *et al.*, *The National Spallation Neutron Source Target Station: A General Overview*, Proc. PAC97 (Vancouver, 1997), p. 86; http://www.triumf.ca/pac97/papers/pdf/2B012.PDF

[46] *Target Systems*, Chap. 5 of the National Spallation Neutron Source Conceptual Design Report (NSNS/CDR-2, May 1997);
http://www.ornl.gov/~nsns/CDRDocuments/CDRSections/Sect5.pdf

[47] J.R. Haines, *Comparison of Liquid and Solid Targets for Pulsed Spallation Neutron Sources*, ORNL report NSNS/TSR0009 (July 1997).

[48] D.B. Cline, ed., *Proceedings of the High Intensity Targeting Workshop*, (Fermilab, April 28-30, 1980).

[49] J.A. Hassberger, *Flowing Liquid Lithium Target*, in [48], p. 12.

[50] R.J. Stefanski, *A Study in Target Design*, in [48], p. 41.

[51] *Feasibility Study into the Development of a Liquid Metal Pulsed Current Target for ACOL*, Report No. C2365/F, Contract No: R/785.985/PS/AA (Cambridge Consultants Ltd., Cambridge, U.K., 1985).

[52] Z. Tang and K. Anderson, *Shock Waves in $\bar{p}$ Target* Fermilab/TN-1763 (Nov. 1991).

[53] K. Skala and G.S. Bauer, *On the Pressure Wave Problem in Liquid Metal Targets*, ICANS-XIII, PSI-Proceedings 95-02 (Oct. 1995).

[54] R.P. Taleyarkhan, S.H. Kim and J.R. Haines, *Modelling & Analysis of AGS Thermal Shock Experiment*, ORNL report.

[55] R.P. Taleyarkhan, F. Moraga and C.D. West, *Experimental Determination of Cavitation Thresholds in Liquid Water and Mercury*, Proc. 2nd Int. Topical Meeting on Accel. Applications, AccApp'98, (Gatlinburg, TN, Sept. 1998); ORNL report.

[56] R.P. Taleyarkhan *et al.*, *Results of Thermal-Shock Modeling & Analyses for the National Spallation Neutron Source*, in *Proc. Topical Meeting on Nuclear Applications of Accelerator Technology*, (Albuquerque, NM, Nov. 1997), p. 293.

[57] L. Ni and G. Bauer, *Dynamic Stress of a Liquid Metal Target Container under Pulsed Heating*, PSI report (1998);
http://puhep1.princeton.edu/mumu/target/bauer/1.html

[58] J.R. Haines, *A Simple figure of Merit for Comparison of Thermal Shock Capabilities of Candidate Target Materials*, ORNL report NSNS/TSR5 (Mar. 3, 1997).

[59] D.H. Trevena, *Cavitation and Tension in Liquids* (Adam Hilger, Bristol, U.K., 1987).

[60] F.R. Young, *Cavitation* (McGraw-Hill, New York, 1989).

[61] T.G. Leighton, *The Acoustic Bubble* (Academic Press, San Diego, 1994).

[62] A. Kovacs, *Estimating the Full-Scale Tensile, Flexular and Compressive Strength of First-Year Ice*, CRREL Report 96-6 (Sept. 1996), Fig. 9;
http://www.crrel.usa.ce.army.mil/techpub/CRREL_Reports_web/reports/CR96_11.pdf

[63] L. Briggs, *Limiting Negative Pressure of Water*, J. Appl. Phys. **21**, 721 (1950).

[64] D.A. Wilson, J.W. Hoyt and J.W. McKane, *Measurement of tensile strength of liquids by an explosion technique*, Nature **253**, 723 (1975).

[65] *Design Report TEVATRON 1 Project*, Fermilab (Sept. 1984).

[66] R. Criss and F.E. Rose, *Spatial and Temporal Development of Emissions from an Exploding Mercury Jet*, IEEE Trans. Plasma Sci. **23**, 145 (1995).

[67] W.E. Ansley, S.A. Merryman and F.E. Rose, *Characterization of Liquid Mercury Jets and the Potential Application as an Opening Switch*, (1995).

[68] W.E. Ansley and F.E. Rose, *Evaluation of Liquid-Metals Jets as the Conductor in a Rep-Rated, Exploding-Fuse Opening Switch*, IEEE Trans. Magnetics **32**, 1980 (1996).

[69] J. Lettry *et al.*, article in preparation (1998).

[70] H. Ullmaier and E. Carsughi, *Radiation damage problems in high power spallation neutron sources*, Nucl. Instr. and Meth. **B101**, 406 (1995).

[71] T.W. Eaton *et al.*, *Conducting Targets for $\overline{p}$ Production of ACOL. Past Experience and Prospects*, IEEE Trans. Nuc. Sci. **NS-32**, 3060 (1985).

[72] *Autopsie d'Une Cible en Cuivre*, CERN Central Workshop Metallurgy Dept. Report No. 3103 (1984).

[73] *Etude d'Une Cible a Antiprotons en Plomb*, CERN Central Workshop Metallurgy Dept. Report No. 3198 (1984).

[74] *Metallographic Examination of a Lightly Irradiated Copper/Graphite/Aluminium Target for CERN*, Report No. EIR KT: 7.423.0284, Federal Institute for Reactor Research (Wŕenlingen, Switzerland, 1984).

[75] R. Horne, *Preliminary Post-Irradiation Examination of a Rhenium "Snout" Target*, CERN Remote Handling Section (1985), unpublished; copy with C. Johnson).

[76] *High Temperature Compatibility Between Materials for Pulsed Current Targets*, Report No. OEFZS-A-0852 WE-402/86 (Osterreichisches Forschungzentrum, Seibersdorf, Austria, 1986).

[77] S.C. O'Day and F.M. Bienosek, *8-9 GeV $\bar{p}$ yield measurements at the Fermilab antiproton source*, Nucl. Instr. and Meth. **A343**, 343 (1994).

[78] Al Pendzick, private communication (1998).

[79] Helge Ravn, private communication (1998).

[80] Günter Bauer, private communication (1998).

[81] R.N. Lyon (ed.), *Liquid Metals Handbook*, 2nd ed., NAVEXOS-P.733 (June 1952, revised 1954); *Liquid Metals*, in *Reactor Handbook*, 2nd ed., C.R. Tipton, Jr., (ed.), Interscience, New York, 1960), p. 994.

[82] *Materials for Spallation Neutron Sources*, Proceedings of the Workshop held at Los Alamos National Laboratory (Feb. 6-10, 1995), ed. by A. Longshore, LA-13097; http.//lib-www.lanl.gov/la-pubs/00285851.pdf

[83] J.R. DiStefano, *A Review of the Compatibility of Containment Materials with Potential Liquid Metal Targets*, ORNL-TM-13056 (Aug. 1995).

[84] D. Filges, R.D. Neef and H. Schaal, *Nuclear Studies of Different Target Systems for ESS*, ICANS-XIII, PSI-Proceedings 95-02 (Oct. 1995), p. 537.

[85] L. Briggs, *Limiting Negative Pressure of Mercury in Pyrex Glass*, J. Appl. Phys. **24**, 488 (1953).

[86] A. des Brasunas, *Interim Report on Static Liquid-Metal Corrosion*, ORNL/TM1646 (May 11, 1954).

[87] J.V. Cathcart and W.D. Manly, *The Mass Transfer Properties of Various Metals and Alloys in Liquid Lead*, Corrosion **12**(2), 43 (Feb. 1956).

[88] A.J. Romano, C.J. Kamut and D.H. Gurinsky, *The Investigation of Container Materials for Bi and Pb Alloys. Part I. Thermal Convection Loops*, BNL-811 (T-313) (July 1963).

[89] G.M. Tolsen and A. Taboda, *A Study of Lead and Lead-Salt Corrosion in Thermal-Convection Loops*, ORNL/TM-1437 (April 1966).

[90] J.R. Weeks, *Lead, Bismuth, Tin and Their Alloys as Nuclear Coolants*, Nucl. Eng. and Des. **15**, 363 (1971).

[91] J.R. DiStefano and O.B. Cavin, *Temperature Gradient Compatibility Tests of Some Refactory Metals and Alloys in Bismuth and Bismuth-Lithium Solution*, ORNL/TM-5503 (Nov. !976).

[92] H. Baker (ed.), *Alloy Phase Diagrams*, 2nd ed., Vol. III of the ASM handbook (ASM International, Materials Park, OH, 1997).

[93] J. Yahia and J.P. Thobe, *The Temperature Dependence of the Resistivity of Liquid Gallium to 1000°C*, Can. J. Phys. **50**, 2554 (1972).

[94] R.K. Smither *et al.*, *Liquid gallium cooling of silicon crystals in high intensity photons beams*, Rev. Sci. Instr. **60**, 1486 (1989).

[95] R.K. Smither *et al.*, *Recent experiments with liquid gallium cooling of crystal diffraction optics*, Rev. Sci. Instr. **63**, 1746 (1992).

[96] Lord Rayleigh, *The Theory of Sound* (reprinted by Dover, 1945), Vol. 2, p. 362.

[97] S. Chandrasekhar, *Hydrodynamic and Hydromagnetic Stability* (reprinted by Dover, 1981), §112.

[98] R.L. Kustom, *The electrical breakdown of Vacuum Insulated Electrodes Under Radio Frequency Stress*, IEEE Trans. Nuc. Sci. **NS-16**, 556 (1968).

[99] A. Shalnov *et al.*, *Magnetic Field Influence on RF-Structures Electrodynamics Characteristics and Sparking Limit*, Proc. PAC95 (Dallas, Texas, 1995), p. 1155;
http://www.cern.ch/accel/conf/p95/ARTICLES/RPR/RPR15.PDF

[100] R. Kishek, Y.Y. Lau and R.M. Gilgenbach, *Temporal Evolution of Multipactor Discharge*, Proc. PAC95 (Dallas, Texas, 1995), p. 1599;
http://www.cern.ch/accel/conf/p95/ARTICLES/TAQ/TAQ32.PDF

[101] A.V. Grudiev, D.G. Myakishev and V.P. Yakovlev, *Simulation of Multipacting in RF Cavities and Periodical Structures*, Proc. PAC97 (Vancouver, 1997), p. 2609;
http://www.triumf.ca/pac97/papers/pdf/9P098.PDF

[102] K.A. Brown, I.H. Chiang, A. Pendzick and T. Tallerico, *Observations of Secondary Emission Chamber Degredation from Very High Intensity Proton Beams at the AGS*, Proc. PAC97 (Vancouver, 1997), p. 2213;
http://www.triumf.ca/pac97/papers/pdf/8P047.PDF

[103] H. Padamsee, *Overview of Advances in the Basic Understanding of Dark Current and Breakdown in RF Cavities*, Proc. PAC97 (Vancouver, 1997), p. 2884;
http://www.triumf.ca/pac97/papers/pdf/9C002.PDF

[104] X. Xu *et al.*, *RF Breakdown Studies in X-Band Klystron Cavities*, Proc. PAC97 (Vancouver, 1997), p. 3045;
http://www.triumf.ca/pac97/papers/pdf/8P032.PDF

[105] R.A. Kishek and Y.Y. Lau, *Multipactor Discharge on a Dielectric*, Proc. PAC97 (Vancouver, 1997), p. 3198;
http://www.triumf.ca/pac97/papers/pdf/7P061.PDF

[106] O. Gröbner, *Beam Induced Multipacting*, Proc. PAC97 (Vancouver, 1997), p. 3590;
http://www.triumf.ca/pac97/papers/pdf/4P004.PDF

[107] C. Ankenbrandt *et al.*, *Bunching Near Transition in the AGS*, Phys. Rev. ST Accel. Beams **1**, 030101 (1998);
http://www-lib.fnal.gov/archive/1998/pub/Pub-98-006.html

[108] AGS FEB home page: http://www.ags.bnl.gov/~tanaka/agsfeb.html

[109] M. Tanaka *et al.*, *The AGS Accelerator Complex with the New Fast Extraction System*, Proc. PAC95 (Dallas, Texas, 1995), p. 1930;
http://www.cern.ch/accel/conf/p95/ARTICLES/WAR/WAR13.PDF

[110] T. Roser, *AGS Performance and Upgrades: A Possible Proton Driver for a Muon Collider*, AIP Conf. Proc. **372**, 47 (1996);
ftp://ftp.mumu.bnl.gov/pub/documents/roser.ps

[111] T. Roser, *High Intensity Performance and Upgrades at the Brookhaven AGS*, Proc. Workshop on Space Charge Physics in High Intensity Hadron Rings, (Shelter Island, NY, May 4-7, 1998).

[112] Nicholas Tsoupas, private communication (1998).

[113] D.D. Earl, J.R. Haines and C.C. Tsai. *Measurement of Strain Experience by a Mercury Target Vessel*, ORNL report SNS/TSR-0040 (1998).

[114] Fiber and Sensor Technologies, Inc., P.O. Box 11704 Blacksburg, VA 024060 (Steve Poland, 540-522-5128);
http://www.f-s.com

[115] National High Magnetic Field Laboratory, 1800 E. Paul Dirac Drive, Tallahassee, FL 32310;
http://www.magnet.fsu.edu/

[116] B.J. Gao *et al.*, *Design of a 20 T, 200 mm Bore Resistive Magnet*;
http://www.magnet.fsu.edu/magnets/resistive/cell4/20tesla200bore/publication/

[117] C. Lu, K.T. McDonald, E.J. Prebys and S.E. Vahsen, *A Detector Scenario for the Muon Cooling Experiment*, Princeton/$\mu\mu$/97-8 (May, 1998);
http://www.hep.princeton.edu/mumu/mumu-97-8.ps

[118] BaBar *Technical Design Report*, SLAC-R-95-497 (March, 1995), Table 5.6, p. 173;
http://www.slac.stanford.edu/BFROOT/doc/TDR/tdr_ch05_ctd.ps.Z

[119] E. Kichimi *et al.*, *The Čerenkov correlated timing detector. Beam test results from quartz and acrylic bars*, Nucl. Instr. and Meth. **A371**, 91 (1996).

[120] S.E. Vahsen and K.T. McDonald, *Precision Timing via Čerenkov Radiation*, Princeton/$\mu\mu$/98-11 (July 25, 1998);
http://puhep1.princeton.edu/mumu/timing.pdf

[121] R. Enomoto *et al.*, *Feasibility Study of Single-Photon Counting Using a Fine-Mesh Phototube for an Aerogel Readout* Nucl. Instr. and Meth. **A332**, 129 (1993)

[122] I. Adachi *et al.*, *Study of a threshold Čerenkov counter based on silica aerogels with low refractive indices*, Nucl. Instr. and Meth. **A355**, 390 (1995);
http://xxx.lanl.gov/ps/hep-ex/9412008

[123] T. Nozaki *et al.*, Nucl. Phys. B (Proc. Suppl.) **50**, 288 (1996).

[124] T. Iijima *et al.*, *Aerogel Čerenkov counter for the BELLE experiment*, Nucl. Instr. and Meth. **A379**, 457 (1996).

[125] T. Iijima *et al.*, Nucl. Instr. and Meth. **A387**, 64 (1997).

[126] M. Hazumi *et al.*, Nucl. Phys. B (Proc. Suppl.) **59**, 61 (1997).

[127] R. Suda *et al.*, *Monte-Carlo Simulation for an Aerogel Čerenkov Counter*, Nucl. Instr. and Meth. **A406**, 213 (1998);
http://xxx.lanl.gov/ps/hep-ex/9707042

[128] M.H.R. Khan *et al.*, *The monitoring system for the aerogel Čerenkov counter of the BELLE detector*, submitted to Nucl. Instr. and Meth.
http://xxx.lanl.gov/ps/hep-ex/9803027

[129] D.R. Marlow *et al.*, *BELLE Aerogel Čerenkov Counter Readout System Documents*;
http://viper.princeton.edu/~marlow/acc/acc.html

[130] S.R. Klein *et al.*, *Front End Electronics for the STAR TPC*, IEEE Trans. Nuc. Sci. **NS43**, 1768 (1996).

[131] ANSYS, Inc., 275 Technology Drive, Canonsburg, PA 15317;
http://www.ansys.com

[132] A. Hassanein, *Deuteron beam interaction with lithium jet in a neutron source test facility*, J. Nucl. Mater. **233-237**, 1547 (1996).

[133] A. Hassanein, *Disruption Damage to Plasma-Facing Components from Various Plasma Instabilities*, Fusion Technol. **30**, 713 (1996).

[134] A. Hassanein *et al.*, *Modeling and simulation of melt-layer erosion during a plasma disruption*, J. Nucl. Mater. **241-243**, 288 (1997).

[135] A. Hassanein and I. Konkashbaev, *Dynamic Behavior of Plasma-Facing Materials during Plasma Instabilities in Tokamak Reactors*, Plasma Devices and Operations **5**, 297 (1988).

[136] Hiro Hiejima, private communication (1998).

[137] M. Blaskiewicz *et al.*, *High Intensity Proton Operations at Brookhaven*, Proc. PAC95 (Dallas, Texas, 1995), p. 383;
http://www.cern.ch/accel/conf/p95/ARTICLES/TAP/TAP13.PDF

[138] L. Ahrens *et al.*, *High Intensity Proton Acceleration at the Brookhaven AGS – An Update*, Proc. PAC97 (Vancouver, 1997), p. 89;
http://www.triumf.ca/pac97/papers/pdf/7P001.PDF

[139] G.T. Danby and J.W. Jackson, Part. Accel. **27**, 33 (1990).

[140] W.K. van Asselt *et al.*, *The Transition Jump System*, Proc. PAC95 (Dallas, Texas, 1995), p. 3022;
http://www.cern.ch/accel/conf/p95/ARTICLES/WAB/WAB04.PDF

[141] J.E. Griffin *et al.*, IEEE Trans. Nucl. Sci. **NS-30**, 3502 (1983).

[142] J.M. Brennan and M.M. Blaskiewicz, Proc. Workshop on Space Charge Physics in High Intensity Hadron Rings, (Shelter Island, NY, May 4-7, 1998).